VRIJE
UNIVERSITEIT
BRUSSEL

Master thesis submitted in order to be awarded the degree of
Master of Science in Engineering Technology:
Electromechanical Engineering - aeronautics

REBUILDING AND VALIDATING AN AERODYNAMIC BALANCE FOR WIND TUNNEL TESTING

Reda Lamrani

2025-2026

promoter: Prof. dr. ir. Mark Runacres
supervisors: Dr. ir. M. Faheem Siddiqui, Ir. Nias Devalckeneer

ENGINEERING SCIENCES

Acknowledgements

My first and deepest thanks go to Nias Devalckeneer and Dr. Faheem Siddiqui. Through the long stretch of evenings and nights that ran into one another, their advice, their motivation, and their trust in me carried the work, originally scoped for two, as much as my own effort did. On a personal note, what stayed with me most is that they consistently treated me as the engineer in spe that I am striving to become, not as a student whose hand they had to hold; that recognition reframed every difficult week as something I was already capable of working through. Supervision of that kind happens quietly, alongside their own research and their own students, and not a single hour of it is taken for granted here.

I would also like to thank my promotor, Prof. dr. ir. Mark Runacres. We ran into each other on campus, started talking about the master thesis, and kept the conversation going on the back of his bike on the way out. That exchange gave me both the motivation to take this on and the honest reading that it would not be easy. The quiet trust that closed that first meeting is what I returned to throughout the year.

A separate place in this acknowledgement belongs to Alain Wery, the workshop's technical expert. Whenever I needed material, machining, or anything the tunnel side of the rig demanded, he was the person I could turn to, and a good piece of advice was never further than a short conversation away. His patience with the rig occupying his bench week after week kept the in-situ calibration campaigns on track.

Finally, to my family and friends: thank you for the steady support that carried me through this year.

Reda Lamrani

Brussels, June 7, 2026

Abstract

The FLOW research group at the Vrije Universiteit Brussel operates a subsonic open-circuit wind tunnel without an in-house external force balance. This thesis reconstructs a two-component balance, donated by BikeValley, into a calibrated dual-axis instrument with a documented uncertainty budget. The research question asks whether the rebuilt balance can measure lift and drag on canonical reference objects within the working envelope of the tunnel, with results that match the established literature inside that budget.

The mechanical reconstruction uses eight NewWay porous-media air bushings, two FUTEK LSB201 load cells, and a PhidgetBridge 1046 bridge amplifier. Static dead-weight calibration follows the recommended practices of ISO 376 and AIAA R-091, and identifies a per-direction bidirectional bias-slope law together with a twelve-coefficient polynomial cross-talk matrix. A GUM-compliant uncertainty budget separates the random repeatability from the systematic absolute-scale contributions. Validation experiments cover a NACA 0012 wing, a wall-mounted circular cylinder in cross-flow, and a 1:70 scaled rotor of the inboard 30 % of the NREL 5 MW reference turbine.

The NACA 0012 polar recovers the lift-curve slope reported in the literature, inside the Prandtl elliptic window, at four campaign velocities. The cylinder drag is consistent with published wall-mounted finite-cylinder data at the matching aspect ratio. The rotor thrust coefficient collapses across two freestream velocities within $|\Delta C_T| \leq 0.03$ over a tip-speed-ratio range of 5 to 12, and the design-point thrust reaches 92 % of a radial-weighted NREL 5 MW estimate.

By those numbers, the rebuilt rig works as a two-axis instrument for static low-Reynolds work on canonical wind-tunnel objects, with an envelope between teaching balances and research-grade external balances. On the software side, a Python application written for the project drives the data: it interfaces with the tunnel-speed and pressure hardware, walks the operator through the dead-weight calibration without any file-editing, applies tare and Barlow–Pope corrections during a polar, and writes one CSV per dwell with the calibration parameters that were active for it. Future students inherit the rig as-is, on the same envelope.

Keywords: aerodynamic balance, wind tunnel, air bearings, static calibration, uncertainty analysis, GUM, NACA 0012, circular cylinder, wind turbine, load cell, data acquisition

Samenvatting

De onderzoeksgroep FLOW van de Vrije Universiteit Brussel beschikt over een subsone open-circuit windtunnel zonder eigen externe krachtbalans. Deze masterproef herbouwt een door BikeValley geschonken balans tot een gekalibreerd tweeassig meetinstrument met een gedocumenteerd onzekerheidsbudget. De onderzoeksvraag is of de herbouwde balans lift en weerstand kan meten op canonieke referentieobjecten binnen het werkbereik van de tunnel, met resultaten die binnen dat budget overeenstemmen met de gevestigde literatuur.

De mechanische herbouw stoelt op acht NewWay luchtlagers met poreuze media, twee FUTEK LSB201 lastcellen en een PhidgetBridge 1046 brugversterker. De statische gewichtenkalibratie volgt de aanbevolen praktijken van ISO 376 en AIAA R-091, en identificeert een bidirectionele helling per richting samen met een polynomiale crossmatrix van twaalf coëfficiënten. Een GUM-conform onzekerheidsbudget splitst de willekeurige reproduceerbaarheid van de systematische absolute-schaalbijdragen. De validatie-experimenten omvatten een NACA 0012 vleugel, een wand-gemonteerde cilinder in dwarsstroming, en een 1:70 schaalmodel van de binnenste 30 % van de NREL 5 MW referentierotor.

De NACA 0012 polaire reproduceert de in de literatuur gerapporteerde liftgradiënt binnen het Prandtl-elliptisch venster op vier campagnesnelheden. De cilinderweerstand stemt overeen met gepubliceerde data voor wandgemonteerde eindige cilinders bij dezelfde slankheid. De rotor-thrustcoëfficiënt collapseert over twee vrijstroomsnelheden binnen $|\Delta C_T| \leq 0.03$ over een tipsnelheidsverhoudingsbereik van 5 tot 12, en de thrust op het ontwerppunt bereikt 92 % van een radiaal-gewogen NREL 5 MW schatting.

De balans staat gevestigd als een werkend tweeassig instrument voor statische metingen bij lage Reynolds op canonieke windtunnelgeometrieën, met een gekwantificeerd bereik dat hem positioneert tussen educatieve en onderzoeksgrade externe balansen. Een eigen Python-toepassing biedt een volledige data-acquisitie- en sessiebeheer-werkstroom, en koppelt aan de bestaande tunnelsturing en drukinfrastructuur; ze leidt de operator door de gewichtenkalibratie als een begeleide procedure die de actieve configuratie bijwerkt zonder handmatige bestandsbewerking, past automatische tarering en Barlow–Pope blokkadecorrecties toe tijdens elke polaire campagne, en logt elke meting met de kalibratieparameters die erop toegepast zijn. De FLOW-groep beschikt nu over een gekalibreerd en gedocumenteerd instrument dat toekomstige studenten op hetzelfde werkbereik kunnen inzetten.

Sleutelwoorden: aerodynamische balans, windtunnel, luchtlagers, statische kalibratie, onzekerheidsanalyse, GUM, NACA 0012, circulaire cilinder, windturbine, lastcel, data-acquisitie

Résumé

Le groupe de recherche FLOW de la Vrije Universiteit Brussel exploite une soufflerie subsonique à circuit ouvert sans balance de force externe propre. Ce mémoire reconstruit une balance à deux composantes, donnée par BikeValley, en un instrument à deux axes étalonné avec un budget d'incertitude documenté. La question de recherche est de savoir si la balance reconstruite peut mesurer la portance et la traînée sur des objets de référence canoniques dans le domaine de fonctionnement de la soufflerie, avec des résultats conformes aux données de la littérature établie à l'intérieur de ce budget.

La reconstruction mécanique utilise huit paliers à coussin d'air NewWay à média poreux, deux cellules de charge FUTEK LSB201, et un amplificateur de pont PhidgetBridge 1046. L'étalonnage statique par poids morts suit les pratiques recommandées par l'ISO 376 et l'AIAA R-091, et identifie une loi de biais bidirectionnelle par direction ainsi qu'une matrice de diaphonie polynomiale à douze coefficients. Un budget d'incertitude conforme au GUM sépare la répétabilité aléatoire des contributions systématiques à l'échelle absolue. Les expériences de validation portent sur une aile NACA 0012, un cylindre circulaire monté en paroi sous écoulement transversal, et un modèle à l'échelle 1:70 du 30 % radial interne du rotor de référence NREL 5 MW.

La polaire NACA 0012 retrouve la pente de portance rapportée dans la littérature, à l'intérieur de la fenêtre elliptique de Prandtl, à quatre vitesses de campagne. La traînée du cylindre concorde avec les données publiées pour des cylindres finis montés en paroi au même allongement. Le coefficient de poussée du rotor coïncide entre deux vitesses d'écoulement libre à l'intérieur de $|\Delta C_T| \leq 0.03$ sur une plage de rapport de vitesse périphérique de 5 à 12, et la poussée au point de conception atteint 92 % d'une estimation NREL 5 MW pondérée radialement.

La balance est établie comme un instrument à deux axes fonctionnel pour des mesures aérodynamiques statiques à bas Reynolds sur des géométries canoniques de soufflerie, avec une enveloppe quantifiée qui la situe entre les balances externes éducatives et de qualité recherche. Une application Python dédiée fournit un flux complet d'acquisition et de gestion de session, et s'interface avec la commande de soufflerie et les capteurs de pression existants; elle guide l'opérateur dans la procédure d'étalonnage par poids morts qui met à jour la configuration active sans édition manuelle de fichier, applique la tare automatique et les corrections de blocage de Barlow–Pope à chaque campagne polaire, et enregistre chaque mesure avec les paramètres d'étalonnage qui lui ont été appliqués. Le groupe FLOW dispose désormais d'un instrument étalonné et documenté que les étudiants à venir pourront déployer sur la même enveloppe.

Mots-clés: balance aérodynamique, soufflerie, paliers à air, étalonnage statique, analyse d'incertitude, GUM, NACA 0012, cylindre circulaire, éolienne, cellule de charge, acquisition de données

Disclosure on the use of AI

Declaration

During the preparation of this work, the author used the following tools and services:

Name of tool/service		Purpose
ChatGPT (OpenAI)	in order to:	To search and surface relevant literature, summarise and help understand surveyed papers, draft and format LaTeX text (including tables and figure layouts), assist with code (including parts of the Python LabVIEW bridge for tunnel speed control and the linear-actuator interface), and provide technical advice across the design and analysis chain. Every summary, drafted passage, and code suggestion was reviewed and verified against the underlying source or hardware behaviour by the author before inclusion.
Claude Code (Anthropic)	in order to:	To assist with Python software development for the data acquisition application, principally the live-view interface and the wind-tunnel connection.
Grammarly	in order to:	To polish the English of the thesis and to check the final revision for spelling and grammar errors.
Writefull	in order to:	To format LaTeX content in Overleaf, principally tables, figure layouts, and nomenclature entries, with grammar and style suggestions on the English text.

After using these tools and services, the author reviewed and edited all content as needed. All experimental work, hardware assembly, calibration campaigns, wind tunnel measurements, data analysis, and engineering decisions were performed entirely by the author. The author takes full responsibility for the content of this work.

Contents

List of Figures

List of Tables

Acronyms

ADC	Analogue-to-Digital Converter
AIAA	American Institute of Aeronautics and Astronautics
AoA	Angle of Attack
DAQ	Data Acquisition
DOF	Degree of Freedom
FLOW	Thermodynamics and Fluid Mechanics (VUB research group)
FS	Full Scale
GUM	Guide to the Expression of Uncertainty in Measurement
HAWT	Horizontal-Axis Wind Turbine
ISO	International Organization for Standardization
JCGM	Joint Committee for Guides in Metrology
LSB	S-Beam load cell family (FUTEK)
MAV	Micro Air Vehicle
NACA	National Advisory Committee for Aeronautics
OFAT	One Factor At a Time
OIML	International Organization of Legal Metrology
OLS	Ordinary Least Squares
PSD	Power Spectral Density
RMS	Root Mean Square
RO	Rated Output
SST	Shear-Stress Transport (RANS model)
TSR	Tip-Speed Ratio
VAWT	Vertical-Axis Wind Turbine
VIV	Vortex-Induced Vibration

Dimensionless numbers

AR	aspect ratio	$\mathrm{AR} = b^2/S$
C_D	drag coefficient	$C_D = D/(\frac{1}{2}\rho V^2 S)$
C_L	lift coefficient	$C_L = L/(\frac{1}{2}\rho V^2 S)$
C_T	thrust coefficient (turbine)	$C_T = T/(\frac{1}{2}\rho V^2 A_{\mathrm{disc}})$
C_f	skin-friction coefficient	$C_f = \tau_w/(\frac{1}{2}\rho V^2)$
Ma	Mach number	$\mathrm{Ma} = V/a$
R^2	coefficient of determination	$R^2 \in [0;\, 1]$
Re	Reynolds number	$\mathrm{Re} = \rho V L/\mu$
St	Strouhal number	$\mathrm{St} = f_s D/V$
TSR	tip-speed ratio	$\mathrm{TSR} = \omega R/V$

Greek symbols

α	model angle of attack	$^\circ$
δ^*	boundary-layer displacement thickness	m
Δ	difference or increment	
θ	balance-to-tunnel rotation angle	$^\circ$
κ	spanwise interpolation factor (blockage)	
μ	dynamic viscosity	Pa s
π	Archimedes' constant	
ρ	air density	kg/m^3
ω	angular speed (rotor or structural mode)	rad/s

Roman symbols

a, b, c	intercept, linear and quadratic coefficients of the cross-talk polynomial	(varies)
A_{disc}	rotor disc area (turbine)	m^2
b	effective span (wing)	m
c	chord (airfoil)	m
D	cylinder or rotor diameter	m
D	drag force (wind axis)	N
F	force	N
f_s	vortex-shedding frequency	Hz
k	coverage factor (GUM)	
L	lift force (wind axis)	N
q_∞	freestream dynamic pressure	Pa
R	rotor radius	m
S	reference area (wing planform)	m^2
T	temperature	°C
T	thrust force (turbine)	N
u	standard uncertainty	
u_c	combined standard uncertainty	
U_{95}	expanded uncertainty at $k = 2$	
V	freestream velocity	m/s
V/V	voltage ratio (bridge output)	mV/V
W	calibration weight	N

Subscripts

t	tension
c	compression
cal	calibration
corr	corrected (after cross-talk or blockage)
meas	measured (before correction)
D, L	drag and lift channel
disc	rotor disc
lbl, std	operator-label and standard TSR
rms	root-mean-square
s	shedding (Strouhal)
∞	freestream

1.1 Context

Reliable force measurements in a subsonic wind tunnel remain central to experimental aerodynamics. Whether the object under investigation is a standard NACA airfoil, a vertical-axis wind turbine rotor, or a professional bicycle, the ability to resolve lift and drag with known uncertainty determines the value of every test campaign. At the Vrije Universiteit Brussel, the FLOW research group operates a subsonic open-circuit wind tunnel that serves both education and research. The laboratory already had an external force balance, but wanted an additional, student-proof instrument with documented calibration and uncertainty records.

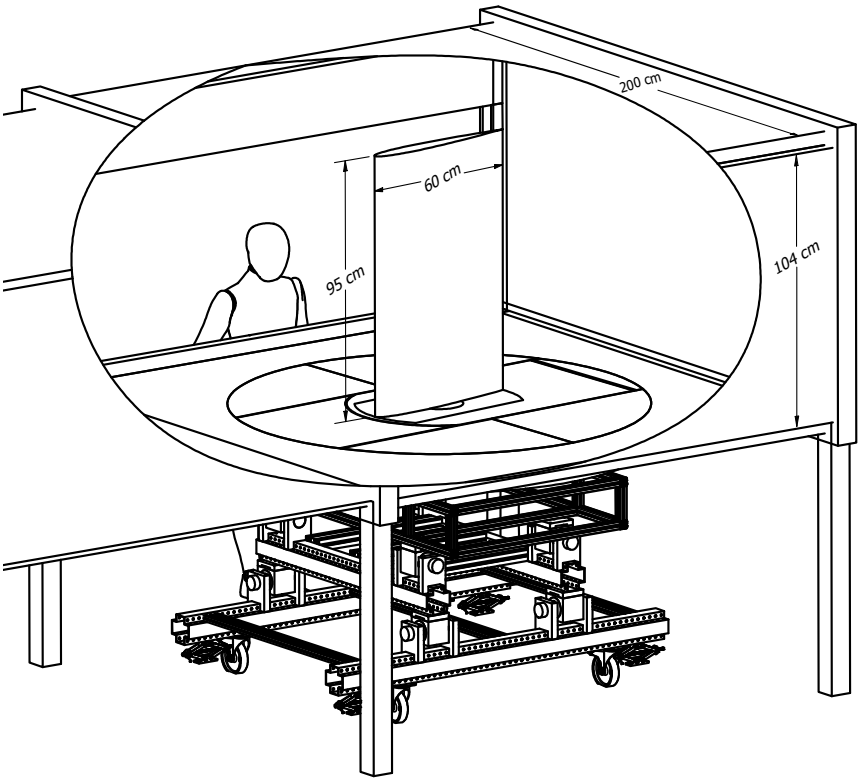

Figure 1.1: Isometric view of the VUB subsonic tunnel test section with the rebuilt two-component aerodynamic balance and a NACA 0012 wing mounted on the turntable. Principal tunnel and rig dimensions are annotated on the drawing.

In 2024, the research centre BikeValley donated a decommissioned two-component balance to the FLOW laboratory after upgrading their own facility. The donated set originally served their cyclist-drag measurements and was an in-house, single-purpose design that came without design documentation, calibration data, or a complete pneumatic chain. This thesis takes the eight NewWay S305002 porous-media air bushings and four FUTEK load cells of that hardware and develops them into a documented and calibrated aerodynamic balance integrated into the VUB wind tunnel.

1.2 Topic and scope

The work in these chapters takes the donated two-component balance from a pile of hardware to a calibrated tool for the VUB subsonic tunnel. Three threads run through it: the mechanical and pneumatic build, the dead-weight calibration with its cross-talk and uncertainty side, and the wind-tunnel campaigns that test whether the chain holds up. A NACA 0012 wing and a wall-mounted circular cylinder serve as the two reference cases. The same pipeline is then turned loose on a scaled NREL 5 MW rotor section. Each campaign is run across the tunnel velocity range and read back against published numbers.

1.3 Research question

Can the reconstructed VUB wind tunnel balance measure lift and drag on a NACA 0012 airfoil and a circular cylinder in a stable and reproducible manner across the operating envelope of the FLOW tunnel, with the resulting C_L and C_D conforming to established reference data within the bounds of a documented uncertainty budget?

1.4 Objectives

The objectives that structured the work are listed in Table 1.1, grouped by category and stated as engineering targets with an acceptance criterion. The hardware-side entries fix the constraints that drove every mechanical, pneumatic and electronic choice of Chapter 3; the calibration, validation, software and uncertainty entries fix the quantitative bar against which the campaign of Chapter 4 is read.

Table 1.1: Objectives and acceptance criteria for the rebuilt balance. Targets are settled before the experimental work begins; each is revisited in Chapter 6.

Category	Objective	Acceptance criterion
Hardware	Force components	2 (lift, drag)
	Model footprint	diameter ≤ 1.5 m
	Maximum lift	≥ 100 N (NACA 0012, $V = 18$ m/s)
	Maximum drag	≥ 50 N (cylinder, $V = 18$ m/s)
	Cell-level uncertainty	$u_{\text{cell}} \lesssim 1$ N
	Structural overdesign	frame static load ≥ 500 kg
	Vertical lift range	jacking stroke ≥ 30 cm
	Air-bushing friction	stick-slip-free at zero velocity
Operational	Installation path	from below, through turntable opening
	Assembly / disassembly	≤ 1 working day by two operators
	Software usability	new user, no supervisor input
Calibration	Linearity	$R^2 \geq 0.999$ on the loaded branches
	Hysteresis	$\lesssim 1$ % FS (educational tier, §2.4)
	Cross-talk	< 3 % between the two components
	Expanded calibration uncertainty	$\lesssim 2$ % FS at $k = 2$ (educational tier)
Software	Voltage-to-coefficient pipeline	live monitoring, tare, blockage in one tool
	Tunnel-side integration	bridge to existing LabVIEW infrastructure
Validation	NACA 0012 lift-curve slope	within ± 5 % of Sheldahl and Klimas (1981)
	NACA 0012 $C_{D,\min}$	within ± 20 % of published data
	Cylinder time-averaged C_D	inside the Wang et al. (2012)–Vardanyan (2023) band
Uncertainty (GUM)	Combined expanded ΔC_D	$\lesssim 0.02$ at $V \geq 15$ m/s (design range)
	Combined expanded ΔC_L	$\lesssim 0.05$ at $V \geq 15$ m/s (design range)

1.5 Thesis structure

The remainder of the thesis is organised in six chapters.

- **Chapter 2** surveys the external- and internal-balance archetypes that dominate published practice, describes the VUB subsonic open-circuit tunnel and the site constraints it imposes, motivates the choice of a direct force balance over surface pressure taps and wake-rake surveys, and positions the present design against published low-cost systems.
- **Chapter 3** hands the reader a build sheet for the assembled balance. Everything is laid out at the level another lab would need to copy it: the column on its two air-bushing stages, the compressor-to-bushing pneumatic line, the FUTEK cells and the Phidget-bridge front end, the polynomial cross-talk model that sits on top of the dead-weight calibration, and the tunnel-side test procedure.
- **Chapter 4** reports the three-phase calibration campaign (bench, in-situ, wind-tunnel), the validation campaigns on the NACA 0012 wing and the bluff body in cross-flow, and the HAWT rotor as the applied case.
- **Chapter 5** places the measured balance performance against the literature comparison of Section 2.4, identifies the dominant design trade-offs, and defines the validity envelope of the measurements.
- **Chapter 6** revisits the objectives of Section 1.4 against the achieved performance and answers the research question.
- **Chapter 7** proposes the next hardware and methodological steps that would tighten the envelope further.

2.1 External and internal balance architectures

Before describing the present balance in detail in Chapter 3, this section walks through the four balance archetypes that dominate the published practice (González et al., 2011). The aim is to set out how each architecture works and what it is typically used for, so that the rationale for the present external two-component air-bushing choice falls naturally out of the comparison.

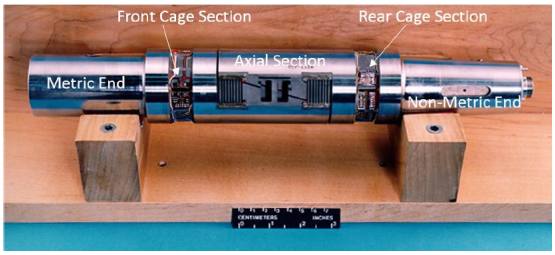

Figure 2.1: Internal strain-gauge moment balance (Sadowski, 2018).

Internal strain-gauge balance. A monolithic element machined from a single billet of precipitation-hardened stainless steel mounts inside the model on a sting. Foil strain gauges bonded to dimensioned flexure sections sense each component through a Wheatstone bridge. The architecture is compact and aerodynamically unobtrusive. Cost is high, and every test model must be designed around the sting geometry.

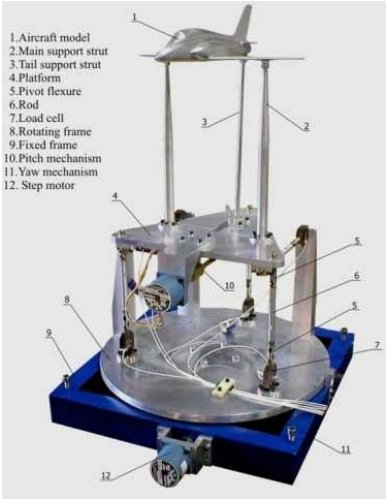

Figure 2.2: Six-component external platform balance (Samardžić et al., 2014).

External platform balance. A rigid platform sits below or above the test section and is supported by several load cells or flexure elements. Each sensor reads a linear combination of the applied forces and moments, so a full calibration matrix is needed to separate the components. The architecture is mechanically simple and accommodates a wide span of model sizes. Its achievable accuracy is bounded by how cleanly the post-measurement matrix decouples the channels (González et al., 2011; Bardera et al., 2024).

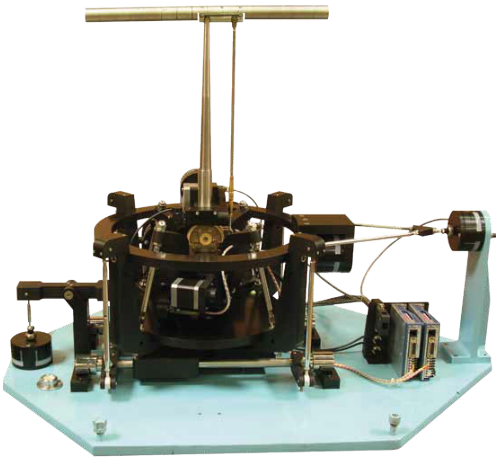

Figure 2.3: Pyramidal force/moment balance (Aerolab LLC, 2024).

Pyramidal balance. Four converging members place a virtual resolving centre at the geometric centre of the test section, so that forces and moments appear at the sensors without mechanical cross-coupling. The architecture is offered as a turn-key product by manufacturers such as Aerolab. Cost and physical footprint keep it uncommon at the educational scale.

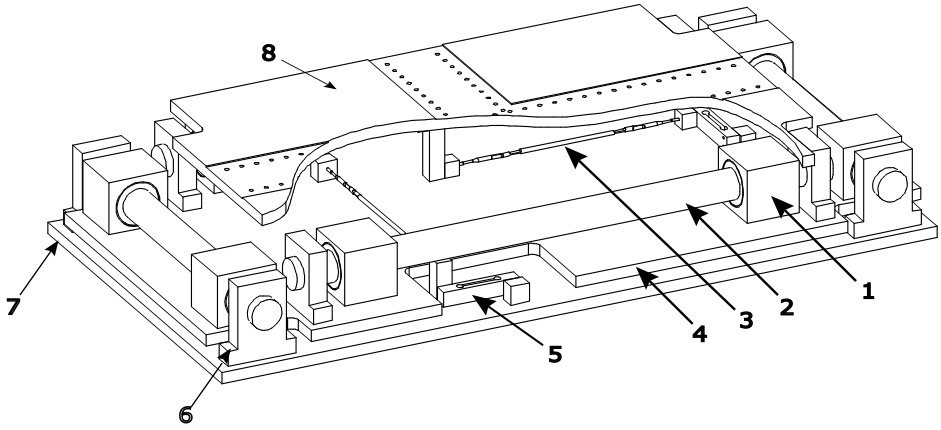

Figure 2.4: Two-axis air-bushing balance layout. Numbered components: (1) air bushing with mounting block; (2) shaft; (3) flexure; (4) middle stage; (5) air bushing; (6) clamping; (7) lower stage; (8) upper stage. Schematic from (Ostafichuk and Green, 2002).

External air-bushing balance. A thin pressurised air film between a porous-graphite bushing and a hardened shaft lets the moving plate translate freely along the measurement axis while reacting all off-axis loads through the same film. Stacking two bushing stages on orthogonal shafts gives a two-degree-of-freedom planar carriage on which the model is mounted, with the in-plane force components read by separate load cells anchored to the fixed frame. The architecture is uncommon at the wind-tunnel scale and is documented in only a handful of published systems (Ostafichuk and Green, 2002; Zhou et al., 2026). Figure 2.4 shows the mechanical layout.

The balance developed in this thesis falls in this fourth category: a two-DOF external air-bushing layout, sized for the educational-tunnel force range. The detailed mechanical build, including the choice of bushing model, the load-cell mounting and the as-built bushing distribution, is given in Chapter 3.

2.2 The VUB subsonic open-circuit wind tunnel

The balance described in this thesis was built around one specific facility: the large low-speed open-circuit wind tunnel of the Vrije Universiteit Brussel. Ambient air enters through a bell-mouth and contraction, passes through a 2000×1000 mm rectangular test section of 12 m overall length, and exhausts via the diffuser into the laboratory without recirculation (Csurcsia et al., 2023). The operating range covers 0 to 20 m/s. The free-stream T_u sits at 0.39 % at $U_0 = 10$ m/s for smooth inflow (Talamalek et al., 2025). Figure 2.5 shows a side view of the test section.

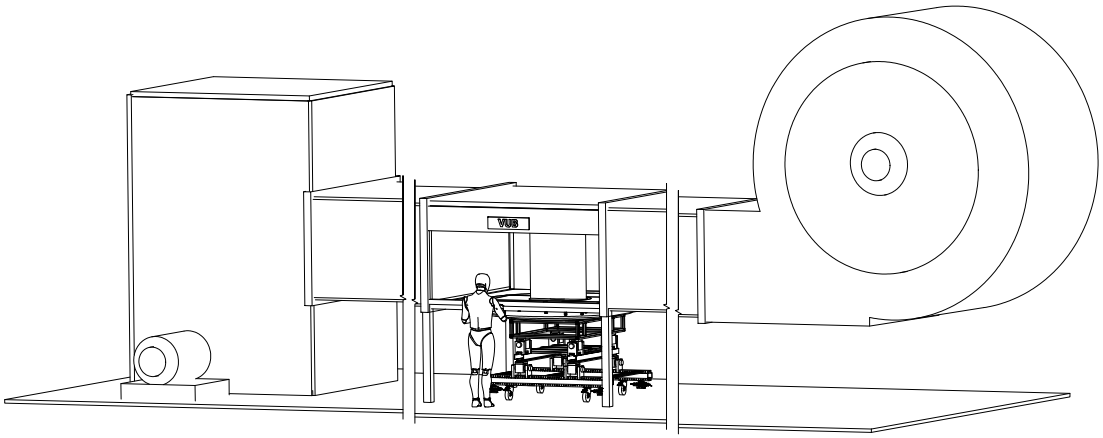

Figure 2.5: Side view of the VUB subsonic open-circuit wind tunnel.

Several site-specific features had to be accepted as given before any balance hardware was considered. The turntable opening in the test-section floor has a diameter of 1.5 m and sets the upper bound on the model footprint (Figure 2.6b). The concrete laboratory floor under the tunnel is markedly out of level. Two structural cross-beams below the test section originally blocked the volume that a full-size rig would occupy (Figure 2.6a); they were taken out by the VUB's Fablab team. The balance assembly is installed from below, through the turntable opening, which fixes the installation path for any rig built around this tunnel.

(a) Test section with the original cross-beams in place.

(b) Underside of the test section with the floor panel removed.

Figure 2.6: The largest VUB wind tunnel: (a) a side view of the test section with the original cross-beams still in place, and (b) the sub-floor access through the removed floor panel used to install the balance.

2.3 Force measurement in low-speed wind tunnels

Three measurement principles compete with a direct force balance for recovering aerodynamic forces on a wind-tunnel model: surface pressure integration, downstream wake survey, and particle image velocimetry (Barlow et al., 1999). The four routes are sketched side by side in Figure 2.7. The choice between them is rarely arbitrary: each route is bounded by what it can and cannot deliver on the model used in this work. Table 2.1 sets the strengths against the limitations side by side.

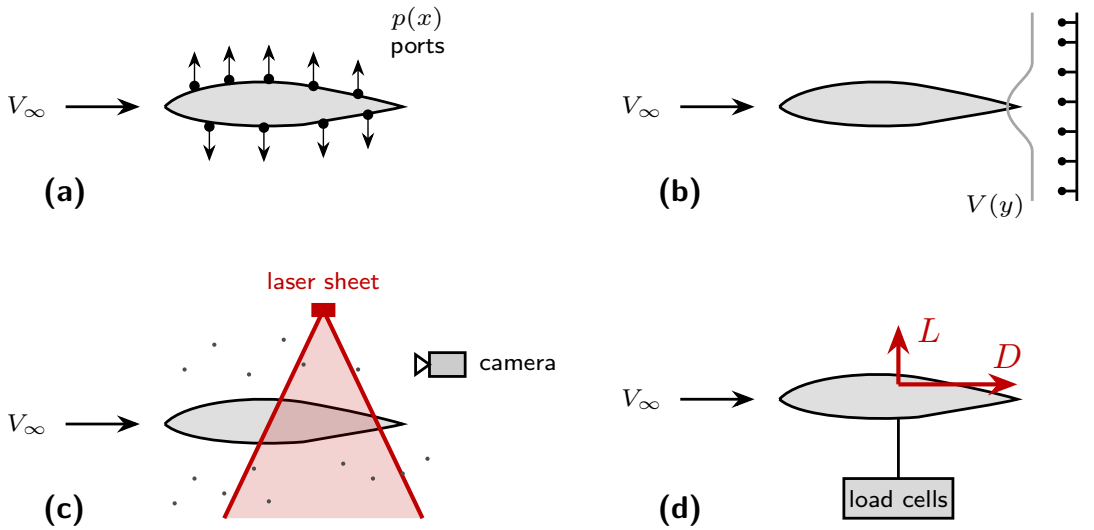

Figure 2.7: Four routes to a force measurement in a low-speed wind tunnel: (a) surface pressure taps; (b) wake-rake; (c) particle image velocimetry; (d) direct force balance.

Table 2.1: Force-measurement principles compared by strength and limitation, for the lift- and drag-resolved campaigns of this thesis.

Method	Strengths	Limitations
Surface pressure taps	Direct local pressure data; mature technology with an established uncertainty envelope.	Cannot resolve skin-friction drag; the model has to be modified with embedded ports; impractical on closed or thin geometries.
Wake-rake (momentum survey)	Recovers drag without modifying the model; independent of the balance hardware.	Lift not directly resolved; assumes uniform inflow and two-dimensional wake; sensitive to probe positioning and wake unsteadiness.
Particle image velocimetry (PIV)	Full velocity field around the model; non-intrusive optical measurement.	Heavy infrastructure (laser, camera, seeding); calibration-intensive per campaign; not realistic for sub-Newton force resolution at undergraduate facility scale.
Direct force balance	Reads the resultant force on the model itself through a calibrated transducer; delivers lift and drag together in real time on the same hardware; no model modification and no wake-plane assumption.	Requires the balance hardware itself and a traceable calibration; sensitive to support-interference and mounting alignment.

The balance route is the only one of the four that delivers lift and drag together on the same hardware, without modifying the model and without an assumption about the inflow or the wake geometry. It is the standard instrument for the campaigns described in Chapters 3 and 4.

2.4 Comparative positioning

The balance literature in the design space targeted by this thesis splits along two natural axes: how the architecture decouples its force components, and where each instrument sits on the cost-versus-accuracy curve. The high-precision air-floating designs of Ostafichuk and Green (2002) and Zhou et al. (2026) occupy one end of the spectrum, with reported residuals at the per-mille level and force ranges deliberately sized for the intended application. At the other end, a growing body of educational and student-built systems uses strain-gauged platforms; these are affordable and mechanically simple, with the accuracy bounded by the quality of a post-measurement decoupling matrix. Table 2.2 collects the most-referenced anchors of that spectrum, with figures taken verbatim from each cited source.

Table 2.2: Comparative positioning of published wind-tunnel balances in the academic and low-cost design space. Numerical entries are taken verbatim from each cited source.

Source	DOF	Sensing & decoupling	Force range	Reported accuracy
Ostafichuk & Green 2002 (Ostafichuk and Green, 2002)	2	Air bushing, mechanical air-film decoupling	0–70 N drag/side	0.38 % FS worst residual
Zhou et al. 2026 (Zhou et al., 2026)	3	Air floating, mechanical air-film decoupling	$O(10^{-4})$–$O(10^{-2})$ N	0.12 % precision
Sor et al. 2019 (Sor et al., 2019)	1 (drag)	Strain gauge, single axis	wide adjustable	n.r. in abstract
Tomin et al. 2020 (Tomin et al., 2020)	3	Strain gauge, post-cal matrix	0–5 kg cells	±10 % on lift/drag
Morris & Post 2010 (Morris and Post, 2010)	2 (+1 opt.)	Strain gauge, post-cal matrix	10 lbf (≈ 44 N) cells	±10 % on C_L/C_D
Weakly et al. 2024 (Weakly et al., 2024)	2	Strain gauge, rigid coupling	0–5 kg sphere/wing	2.5 % MAPE (static)
Sadowski 2018 (Sadowski, 2018)	2 (thrust/torque)	Strain gauge, single-piece flexure	15 lbf thrust, 15 in-lbf torque	±0.1 % FS @ 95 % CI
Santamaría et al. 2024 (Santamaría et al., 2024)	3	Strain gauge, post-cal matrix (cubic LS)	5 kg cells	RMSE 0.0158 (C_D), 0.0258 (C_L)

Notes. FS: full scale. MAPE: mean absolute percentage error. n.r.: not reported in the source abstract.

Two patterns hold across the rows. One is about how each camp deals with uncertainty. Research instruments characterise their cross-talk and quote per-mille residuals; educational platforms hand back a headline percentage without much of a budget. The other is force range. Air-floating references stay in narrow windows where their resolution is still useful, and strain-gauge platforms reach further at the price of a coarser absolute accuracy. For a balance built at the teaching tier of this space, the percent band is the realistic expectation, and the calibration documentation decides where inside that band the instrument actually lands. Where this design sits, with the numerical evidence, is taken up in Chapter 5.

3.1 Problem statement and design requirements

The literature in Chapter 2 places the present balance at the intersection of three constraints: an external two-component layout, an air-bushing pre-decoupling architecture, and an educational subsonic tunnel environment. Few published systems combine all three. The site-specific features documented in Section 2.2 fix the rest of the design space. The balance must fit the existing turntable, be installable from below, level itself on an uneven floor, and resolve sub-Newton drag on small reference models.

The engineering targets that follow from these constraints, together with the calibration, validation, software and uncertainty acceptance criteria for the campaign, are collected in Table 1.1 of Chapter 1. They are the explicit reference against which every design decision in the remainder of this chapter is justified.

3.2 System overview and coordinate frame

The present balance is a two-component external air-bushing system, sized to fit the VUB facility and to belong to the architecture introduced in Section 2.1. The model attaches to an upper plate that floats on two stacked stages of porous-graphite air bushings, mounted 90° apart so that one stage carries the drag motion and the other the lift motion. The assembly sits on a steel frame that is rolled in from below the tunnel and raised into the test-section floor. Figure 3.1 sketches the side view with the wind-axis lift and drag vectors at the model.

Two coordinate systems appear in this work. The *balance frame* (x_b, y_b) is fixed to the bushing stages, with x_b along the drag-stage axis and y_b along the lift-stage axis. The *tunnel frame* (x_t, y_t) is fixed to the test section, with x_t along the free-stream flow and y_t vertical. A unified offset angle $\theta = 2.64°$ between the two frames was identified from a bare-balance dead-weight calibration and is applied to every campaign of this thesis (wing, cylinder, turbine). The rotation

$$\begin{bmatrix} F_D \\ F_L \end{bmatrix}_t = \begin{bmatrix} \cos\theta & -\sin\theta \\ \sin\theta & \cos\theta \end{bmatrix} \begin{bmatrix} F_{x_b} \\ F_{y_b} \end{bmatrix} \tag{3.1}$$

maps the two measured cell forces (F_{x_b}, F_{y_b}) into the wind-axis drag and lift components (F_D, F_L) used in Chapter 4. The angle of attack of the model is set by an external linear actuator whose calibration is reported in Chapter 4. The component-level breakdown of the structure follows in Section 3.3.

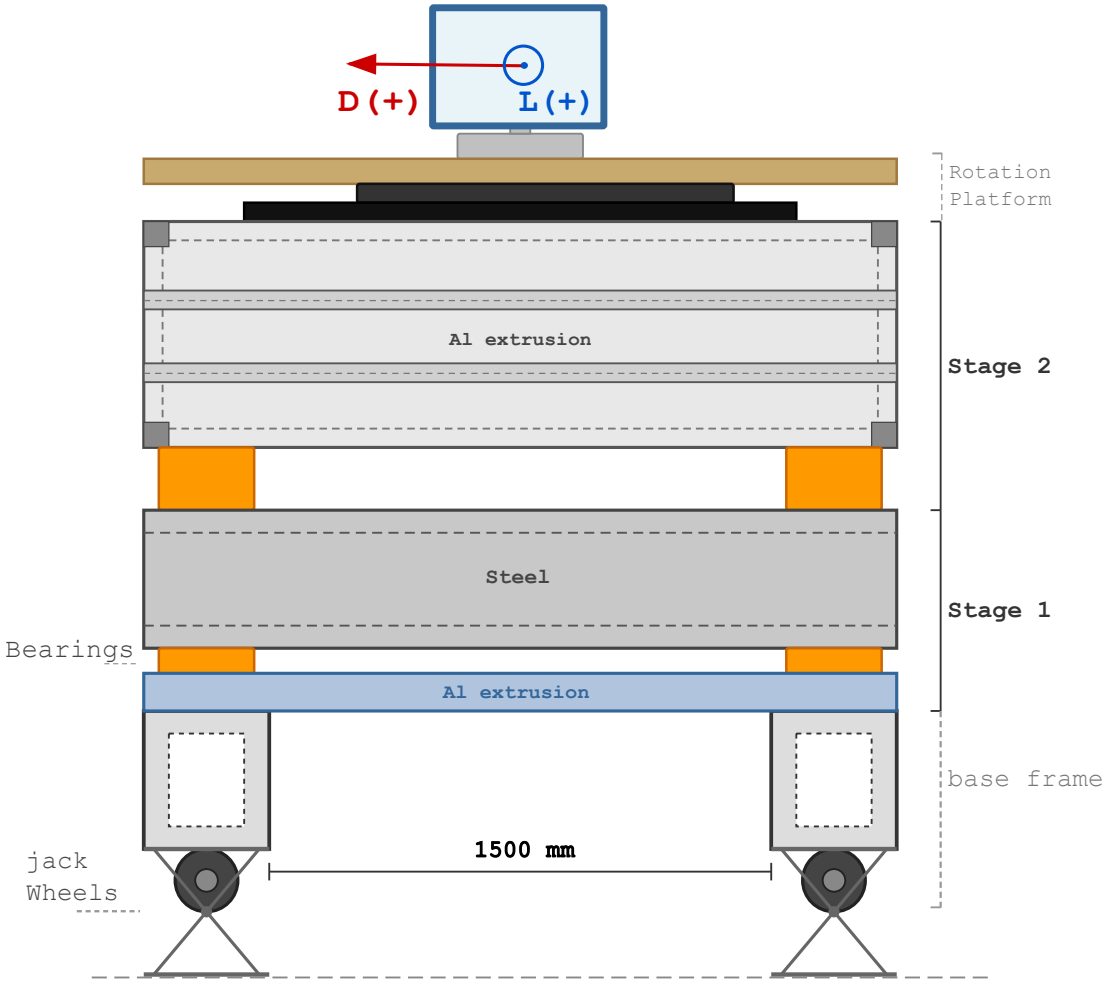

Figure 3.1: Side view of the balance with the positive wind-axis lift L and drag D directions at the model and the mechanical build-up from base frame through the two bearing stages to the rotation platform. The 1500 mm dimension is the base-frame footprint width.

3.3 Mechanical design and integration

The structure is built up vertically in five layers, rendered in Figure 3.2 and indicated schematically in Figure 3.1. Going from the laboratory floor upward: (i) a *baseline frame* that carries the entire balance on wheels and jacks; (ii) a *first bearing stage* that allows translation along one horizontal axis; (iii) a *second bearing stage*, mounted 90° on top of the first, that allows translation along the orthogonal horizontal axis; (iv) the *turntable assembly* that sets the model orientation; and (v) the *model interface* on top. Each layer rests on the one below through clamped joints. No welding is used inside the measurement load path, because welding introduces permanent thermal distortion that would shift the bearing alignment by more than the air-gap tolerance allows. As-built workshop photographs of the assembly are reproduced in Appendix E.

Figure 3.2: CAD render of the balance structure showing the five-layer vertical build-up from the rolling base to the model interface.

3.3.1 Baseline frame, transport and levelling

Everything above this layer sits on the baseline frame, and the frame is the rig's only contact with the lab floor. Three jobs fall to it: rolling the balance between storage and tunnel, raising it through the turntable opening, and absorbing the unevenness of the concrete once it is in place.

Rolling base. A welded steel frame on four casters allows two operators to roll the assembly into the tunnel room and align it under the turntable opening (Figure 3.3a). The frame is built from imperial cross-section channels (hole pitch 1 inch, profile width 1 inch with 0.5 inch flanges) inherited from the donated assembly, which sets the bolt-pattern compatibility for every component above it.

Jacks. Four scissor-style jacks lift the frame from rolling height to tunnel-floor level. Eight would spread the load more evenly, but each is cranked by hand: four stays within one operator's

reach, while eight makes it a two-person job that breaks the student-use target of Table 1.1. The four are therefore kept, and the lateral play they leave is removed afterwards by the stabilisers below. The 8 mm steel base plates under each jack (Figure 3.3c) are custom-machined and welded to the rolling-frame uprights so that the lifting load is taken in pure compression rather than through bolted joints.

Stabilisers. Once the jacks are at working height, four secondary stabilisers are placed under the frame (Figure 3.3b). They bring the frame to the eight support points a second set of jacks would have given, killing the lateral wobble that four jacks alone allow when an operator brushes against the rig. The stabilisers are not load-bearing in the strict sense; they take over the vibrational baseline so that the jacks no longer see small ambient floor motion.

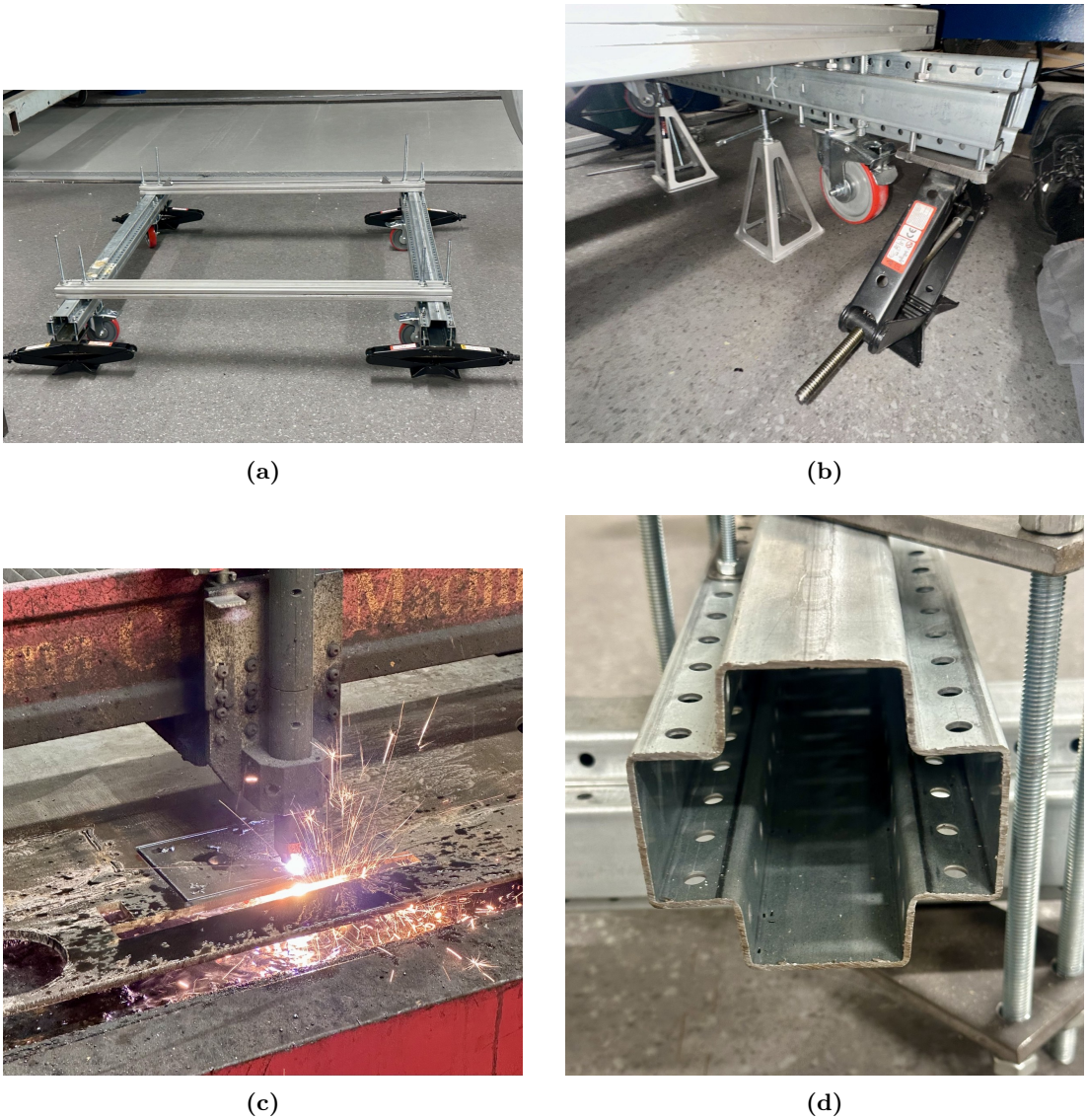

(a) **(b)**

(c) **(d)**

Figure 3.3: Four views of the baseline frame. (a) Rolling base on four casters with jacks retracted. (b) Jacks raised, secondary stabilisers in place. (c) Custom-machined 8 mm steel plates welded under each jack mount. (d) Imperial cross-section steel channel inherited from the donated assembly.

The three elements above, rolling base, jacks, and stabilisers, were each selected as the best of several options considered during the design. Wheel size sits at the largest diameter that fits within the height-limited base; larger wheels reduce the push force needed to roll the assembly

across the laboratory floor. The final baseline meets the operational targets of Table 1.1. It has stayed within those targets across every campaign reported in this thesis.

3.3.2 Two-stage air-bushing column

Two stacked air-bushing translation stages, mounted 90° apart, realise the two measurement axes: stage 1 rides on the lower shaft pair and stage 2 on the orthogonal upper pair, both on porous-graphite bushings. The result is a single platform that translates freely in drag and in lift, with each axis sensed by an independent load cell.

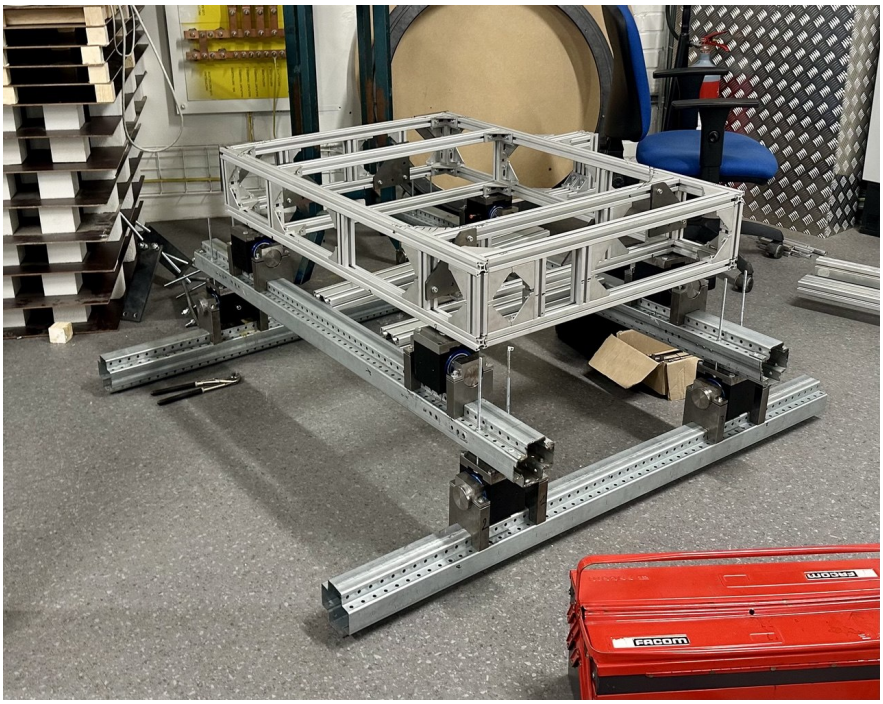

Figure 3.4: Bare bushing-stage architecture with both stages still to be aligned.

Every connection inside the column is bolted through aluminium-extrusion clamping blocks; welding was avoided to keep thermal distortion below the bushing air-gap tolerance. The clamps hold polished 50 mm steel shafts on which the bushings ride. A close-up of one such clamp and a separate view of the NewWay porous-graphite bushings used in both stages are shown in Figure 3.5.

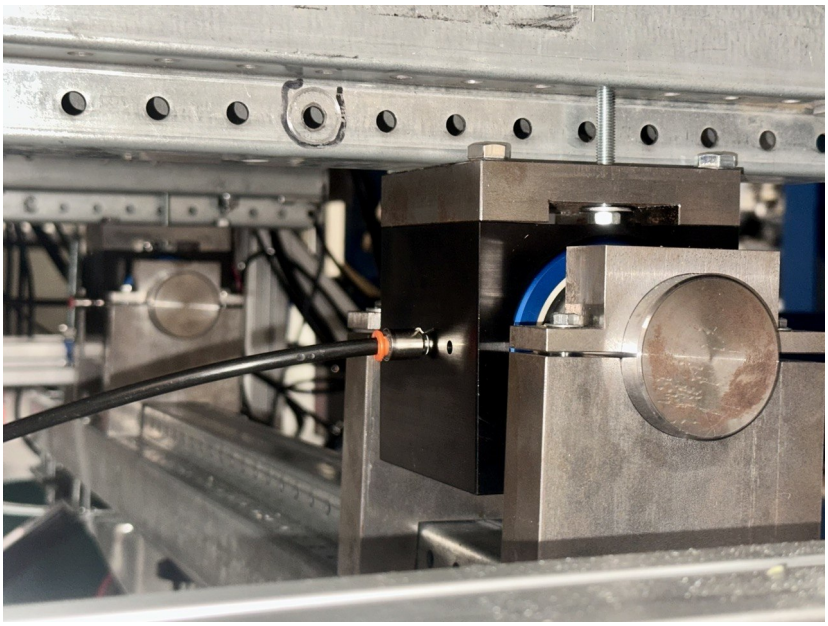

(a)

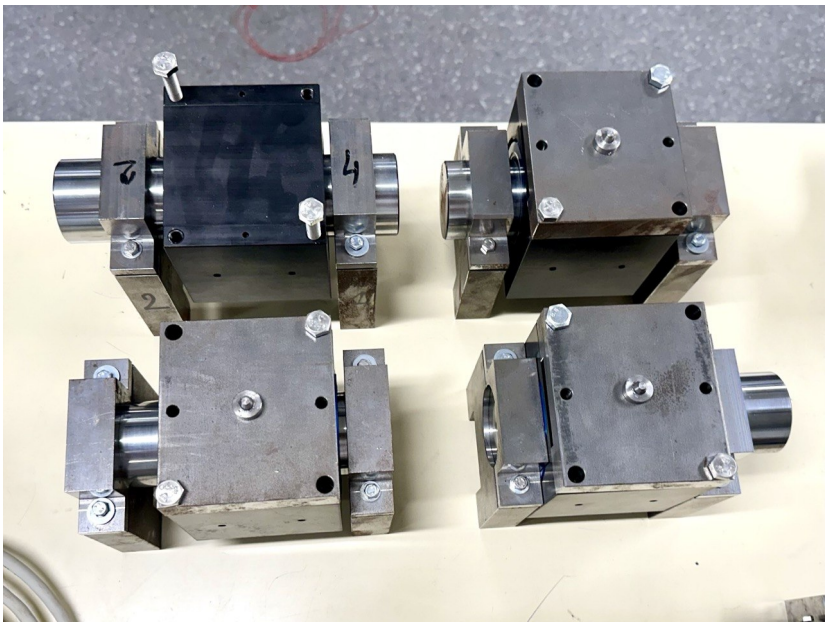

(b)

Figure 3.5: (a) Close-up of a NewWay bushing held in its aluminium-extrusion clamping block on the polished steel shaft. (b) The NewWay porous-graphite air bushings used in both stages.

The two longitudinal shafts in stage 1 double as the load path for the upper assembly and are ground to the bushing surface finish (New Way Air Bearings, 2006); stage 2 adds a perpendicular pair, set orthogonal against a granite reference. A T-slot aluminium frame carries the column and integrates the calibration-fixture mounts. Operating conditions and bushing cleaning are covered in Section 3.4. Figure 3.6 shows the stage 1 clamp together with a first floating test of the assembled column.

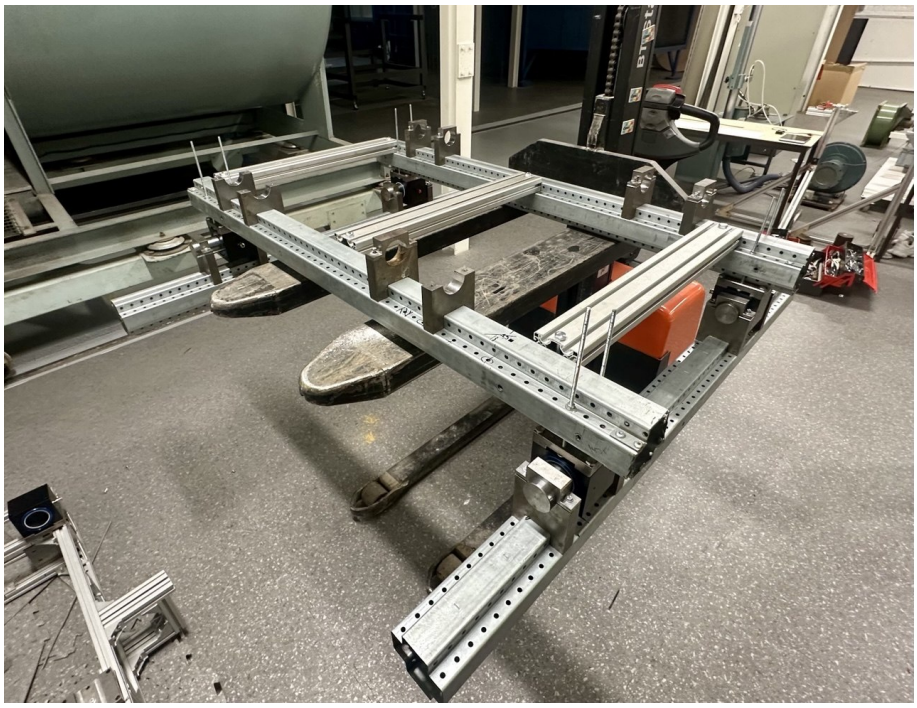

(a)

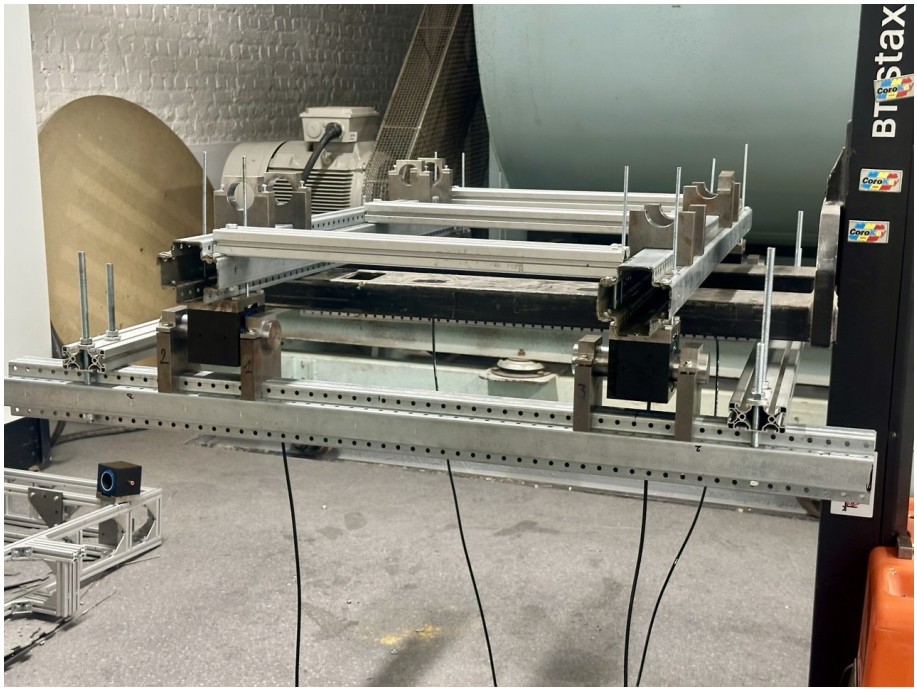

(b)

Figure 3.6: Two-stage air-bushing column: stage 1 detail with aluminium-extrusion clamps holding the ground steel shafts (a) and an early floating test of the assembled column (b).

3.3.3 Load-cell mechanical mounting

Each axis of the column is sensed by a single S-beam load cell that closes the mechanical loop between the moving platform and the fixed rig. The electrical chain (bridge excitation, amplifier, acquisition) is described in Section 3.5; this subsection covers only the mechanical interface.

The load cell is bolted rigidly to the rig on one side and connected to the moving platform through a rod-end bearing on the other (Figure 3.7). The rod-end allows three rotational degrees of freedom and transmits axial force through its centreline. Any residual moment or off-axis component that bypasses the rod-end is absorbed into the calibration matrix and the uncertainty budget reported in Chapter 4.

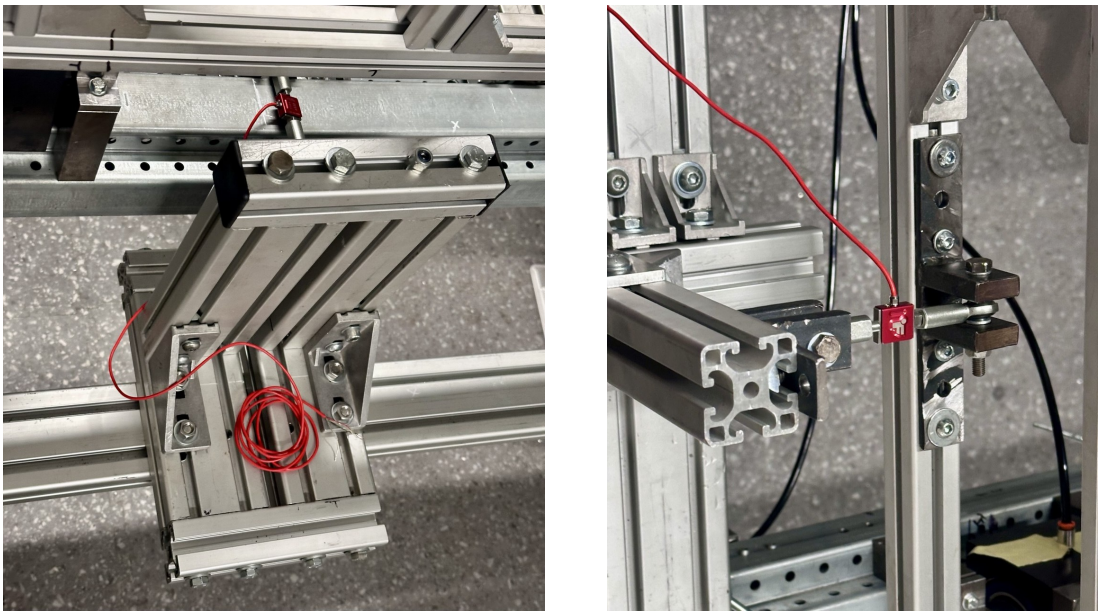

(a) **(b)**

Figure 3.7: Close-up of the two load cells as mounted on the balance: lift channel (a) and drag channel (b). One end is bolted to the rig; the other end connects to the moving platform through a rod-end bearing.

3.3.4 Turntable and model interface

Above stage 2 sits a 1.5 m slewing bearing that handles the angle-of-attack rotation about the vertical axis (Figure 3.8). On top of the bearing is a two-plate stack: a wooden lower plate bolted to the upper race, with a smaller secondary turntable above it. The stack provides vertical standoff and a regular bolt-pattern grid. The NACA 0012 wing, the cylinder, and the vertical-axis turbine all bolt onto that grid.

3.3.5 Mechanical verification

Two bench-side checks validate the column ahead of the pneumatic and DAQ chain. A spirit level on the upper plate is the primary levelling reference (Figure 3.9a). With the air supply at pressure, a pocket Newton meter then probes the residual friction of each bearing in turn (Figure 3.9b): the platform should accept a horizontal push of order 0.1 N and start moving without any threshold step. A failed friction floor on a single bearing motivated the bushing cleaning and the additional filter of Section 3.4.

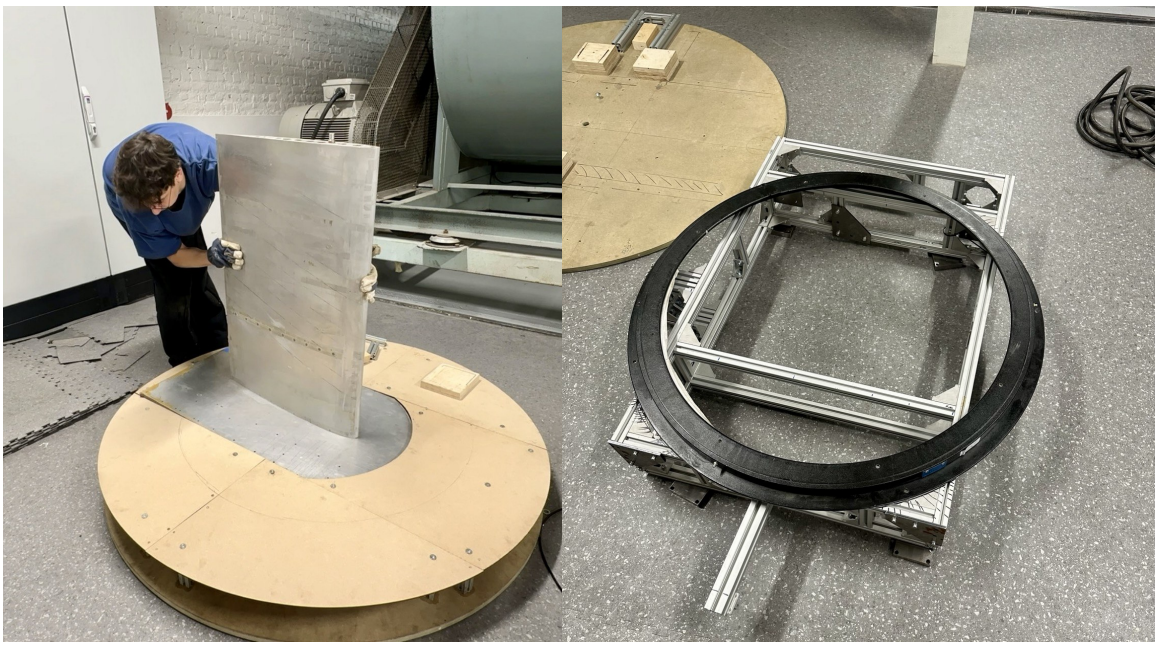

(a) **(b)**

Figure 3.8: Turntable and model interface: (a) two-plate turntable stack with model-mounting bolt pattern; (b) the large slewing bearing seated on the stage 2 rig.

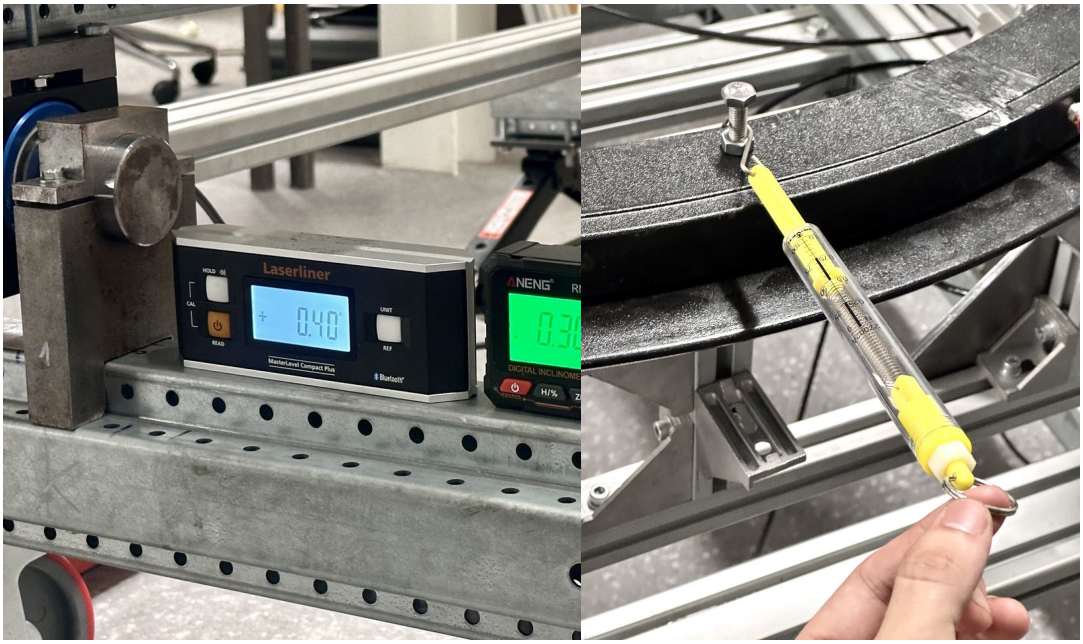

(a) **(b)**

Figure 3.9: End-of-build mechanical checks: (a) spirit level on the upper plate during installation; (b) Newton-meter probe of the bearing friction floor.

3.4 Pneumatic air supply and bushing maintenance

The air supply feeds the seven porous-graphite bushings of the two-stage column with oil-free, dry compressed air. The chain is laid out left-to-right in Figure 3.10: a single supply line runs from the compressor through two regulators in series, then through a fine separator, and finally splits into the manifold that feeds the bushings. The contamination event mentioned in Section 3.3.5 drove the addition of the fine-filter stage, because trapped particles in a porous bushing cannot be cleared from the running side once embedded.

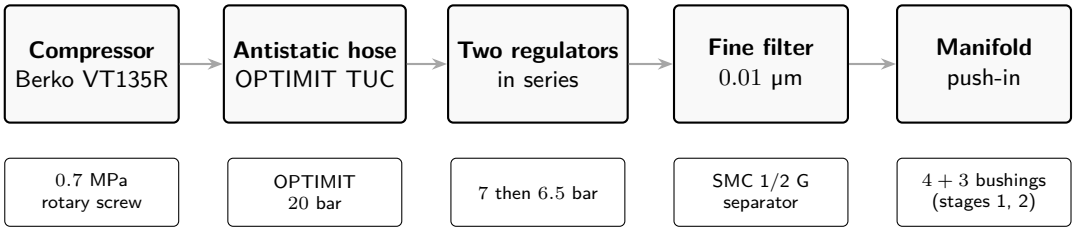

Figure 3.10: Pneumatic chain from compressor to bushings. Numbered stages match the per-component descriptions below.

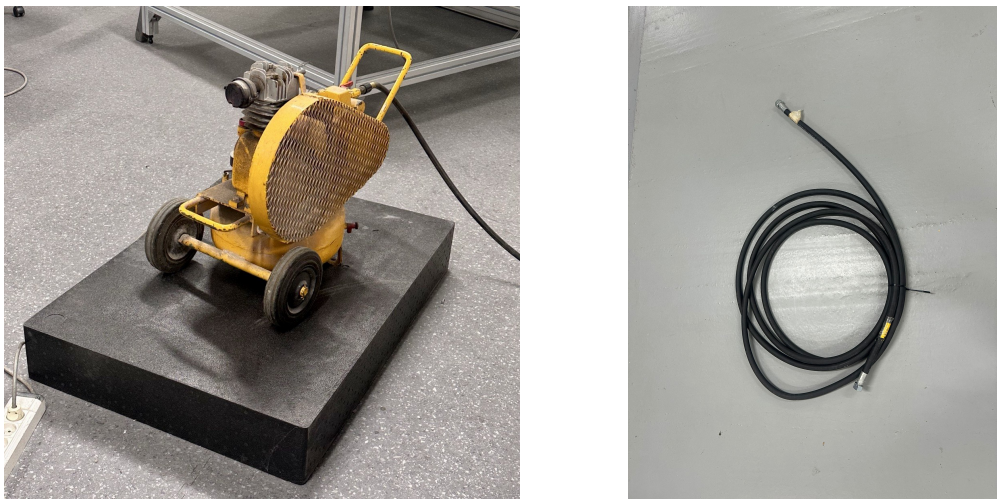

(a) **(b)**

Figure 3.11: (a) Berko VT135R compressor on its anti-vibration mat. (b) OPTIMIT TUC antistatic compressed-air hose between the compressor and the balance frame.

Compressor. A Berko VT 135R rotary-screw compressor supplies the laboratory line at 0.7 MPa. The unit sits on an anti-vibration mat (Figure 3.11a) to isolate the compressor pulsations from the balance frame; the impact of pulsation on the bridge baseline is discussed in Chapter 4.

Antistatic hose. The lab line is brought to the balance frame through an OPTIMIT TUC antistatic oil hose, rated to 20 bar and 13 mm bore (Figure 3.11b). It connects to the compressor outlet through a European-standard pneumatic quick-fitting, which was the simplest mating option for the existing hardware.

Two regulators in series. Two SMC regulators sit in series on the balance frame (Figure 3.12a): the first drops the line to 7 bar, the second trims it finely to 6.5 bar. Mixing the imperial threads from the donated stock with the metric tubing on this side of the rig took several adapter iterations to converge. The lower bucket traps condensation (Figure 3.12b) which would otherwise reach the bushings.

Fine filter. The final stage before the manifold is an SMC 1/2 G pneumatic separator with a 0.01 µm filtration rating, operating from 0.5 to 10 bar (Figure 3.12c). It traps any sub-micron oil aerosol and residual moisture droplets that escape the upstream stages; this safeguard was missing from the early layout, and the contamination event of Section 3.3.5 retroactively justified its addition.

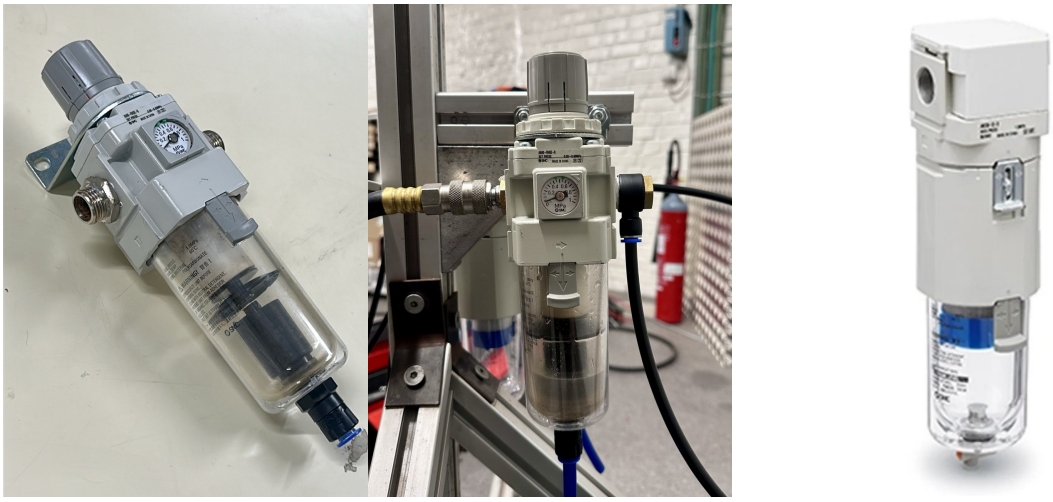

(a) **(b)** **(c)**

Figure 3.12: (a) The two SMC regulators in series on the balance frame, set to 7 bar then 6.5 bar. (b) Condensed water collected in the regulator bowl on a humid morning. (c) SMC 1/2 G pneumatic separator, 0.01 µm filtration, 0.5–10 bar.

Manifold and push-in distribution. After the fine filter, the line splits through push-in fittings into the manifold that feeds the seven bushings (4 + 3 over stages 1 and 2). The push-in system was chosen for tool-free reconfigurability; the redistribution rationale and the 6.5 bar set-point selection are revisited below.

Operating pressure. The 6.5 bar set-point sits within the manufacturer-recommended 40–100 PSI range (New Way Air Bearings, 2006). A screening at 5.0 bar and 6.5 bar returned drag-channel slope spreads of 9.1 % and 0.30 % respectively under a varying vertical load (Section 4.2.2); higher film pressure stiffens each bushing against the load-dependent tilt that drives off-axis cross-coupling.

Contamination and bushing cleaning. During early commissioning, a residual friction step was tracked back to a single contaminated bushing; the porous pore network acts as a one-way trap that cannot be cleared from the running side once oil mist or dust has settled in (Figure 3.13). The recovery procedure unbolted each affected bushing while keeping it pressurised, alternated 99 % ethanol and distilled-water rinses over several hours, and held the unit under continuous pressure during drying. Of the eight original bushings, one did not recover and was labelled defective.

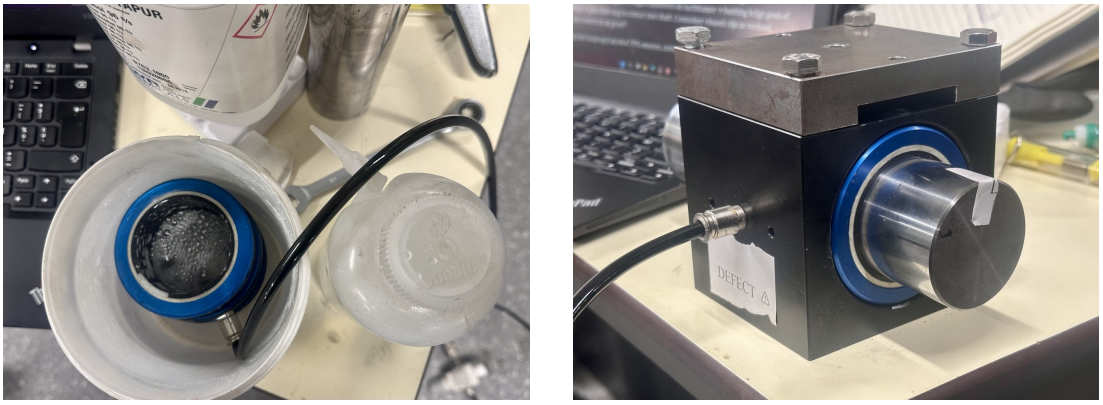

(a) **(b)**

Figure 3.13: In-place ethanol cleaning of a contaminated bushing (a) and the unit declared defective after the cleaning campaign (b).

Bushing redistribution. The column was fitted with eight bushings at the start of commissioning. At roughly 500 EUR a unit, replacing the one that cleaning had declared defective was hard to justify on the project budget, so the balance was run on the seven remaining units in an asymmetric four-plus-three $(4 + 3)$ distribution over the two stages. Stage 1 carries the bulk of the dead weight, so it takes four, set in a pyramid pattern for symmetric mass distribution. The remaining three sit on stage 2, on the orthogonal shaft pair. Late in the first commissioning phase a residual moment showed up on stage 2; a remount step cancelled it, with the diagnostic figure reported in Chapter 4. The Newton-meter friction-floor test on the final $4 + 3$ layout returned a residual threshold inside the cell-level target of Table 1.1.

Operational procedure. At the start of every campaign day the water trap is emptied, the compressor is brought up to setpoint, and the local regulator is checked. The bushings stay pressurised throughout the day. The air supply is only shut off after the column has been mechanically secured, because shutting off the air with the column free to translate risks contact between shaft and bushing.

3.5 Load cells and data acquisition

The mechanical chain of Section 3.3 ends at two single-axis load cells; the data chain starts at their Wheatstone bridges. Two independent USB branches carry the measurement back to the host computer. One handles the load cells through a bridge amplifier; the other handles the linear actuator that sets the angle of attack. Both branches share a single LabVIEW process, so that every commanded angle is time-aligned with the corresponding load-cell sample.

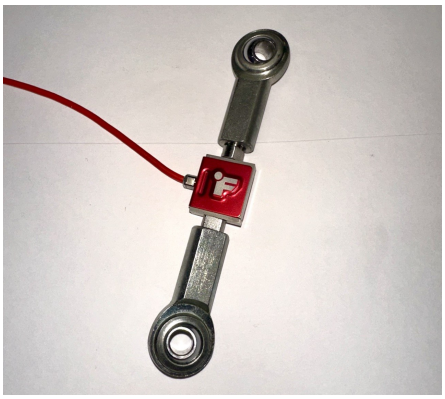

Figure 3.14: FUTEK LSB201 Miniature S-Beam load cell as supplied.

Load cells. Each measurement axis uses a FUTEK LSB201 Miniature S-Beam load cell, rated at 25 lb (111 N) with a 2 mV/V output at 5 V DC excitation. Every cell is bolted to the fixed rig on one side and connected to the moving plate through a rod-end bearing on the other, with the load transferred through a hardened shaft. The 111 N capacity covers the lift and drag of the validation models with margin (Table 1.1); the factory calibration sheet shipped per cell is reproduced in Appendix B.1. The mechanical mounting inside the column is described in Section 3.3.3.

Figure 3.15: Phidget Bridge 1046 four-channel bridge amplifier as supplied.

Bridge amplifier and acquisition. A Phidget Bridge 1046 supplies the 5 V DC excitation and digitises the load-cell output over USB through a four-channel 24-bit delta-sigma converter with gains from 1× to 128×. The quantity stored on disk is the bridge ratio V/V_{exc} in mV/V, which keeps the calibration model of Section 3.6 independent of the excitation voltage. Acquisition runs in LabVIEW on top of the open-source Phidget SDK; the full Python and LabVIEW source is hosted at the link given in Appendix A, and a screenshot of the calibration wizard during an in-situ run is shown in Appendix E.

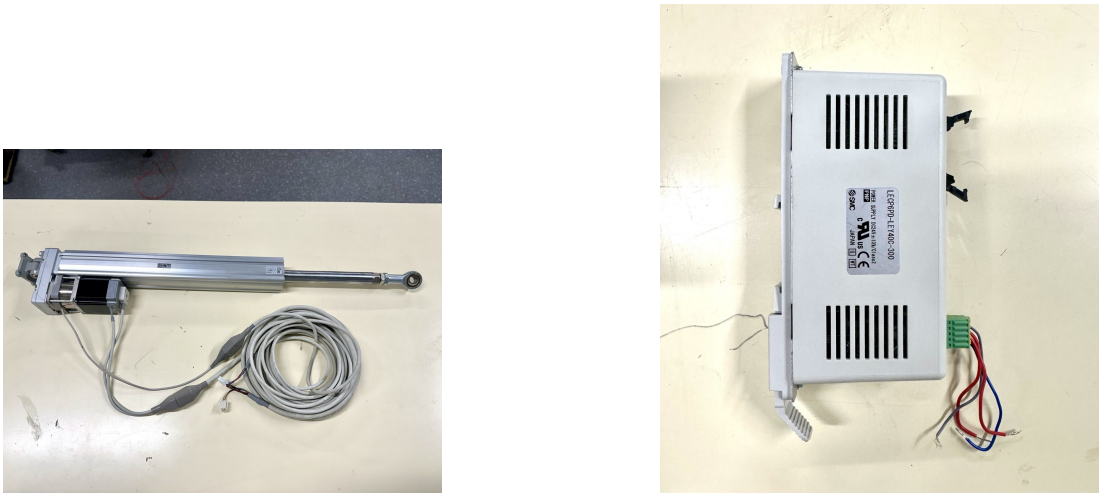

(a) **(b)**

Figure 3.16: Angle-of-attack actuator chain: SMC LEY40C electric actuator (a) and SMC LECP6 step driver (b), addressed over Modbus RTU through a USB-to-RS485 adapter.

Linear actuator drive chain. The angle of attack is set by an SMC LEY40C electric actuator driven by an SMC LECP6 step controller (SMC Corporation, 2023). The controller is addressed over Modbus RTU at 38 400 baud through a USB-to-RS485 adapter (WCH CH340), so that the actuator appears as a second, independent USB device on the host. Position commands and per-step move profiles are issued by the same LabVIEW process that records the bridge data, directly through the CH340 adapter without an intermediate vendor GUI. The actuator geometry and the calibration of commanded position against measured angle of attack are reported in Section 4.4.1.

Limitations of the chain. The Phidget Bridge is a consumer-grade USB amplifier rather than a laboratory-grade DAQ front-end. Its sequential channel readout, sample-rate cap, and gain stability are absorbed by the steady-state averaging window used in the wind-tunnel campaigns of Chapter 4. The chain also lacks an on-board shunt-calibration resistor, so every recalibration runs through the dead-weight loading sequence of Section 3.6.

Table 3.1: Measurement-chain components and key operating values used in the wind-tunnel campaigns of Chapter 4.

Component	Role	Operating value
FUTEK LSB201 (×2)	Force sensing (lift, drag)	25 lb (111 N) S-beam, 2 mV/V
Phidget Bridge 1046	Bridge excitation + ADC	5 V, 128× gain, $\leq$ 122 Hz, 24-bit
SMC LEY40C	Angle-of-attack actuator	300 mm stroke, stepper-driven
SMC LECP6	Step controller	Modbus RTU @ 38 400 baud
WCH CH340	USB↔RS485 adapter	USB endpoint for the actuator

3.6 Calibration methodology

The calibration ties the bridge ratio recorded by each load cell back to a force in newtons and removes the small cross-axis signal that the shared mechanical platform couples through. Both steps run inside the same dead-weight session. The same applied masses generate the on-axis sensitivity and the off-axis bleed used to fit the cross-talk model.

3.6.1 Bench-fixture iteration

The bench fixture that holds the load cell during the off-rig sensitivity test went through three iterations before reaching the chosen configuration. Configuration 1 introduced friction-driven hysteresis through its rod-end ball bearing. Configuration 2 added a flexure but failed at half scale. Both are shown in Figure 3.17. Configuration 3 (Figure 3.18) replaced the cable-and-pulley path with vertical gravity-aligned dead-weight loading and is the form used for every calibration in this work.

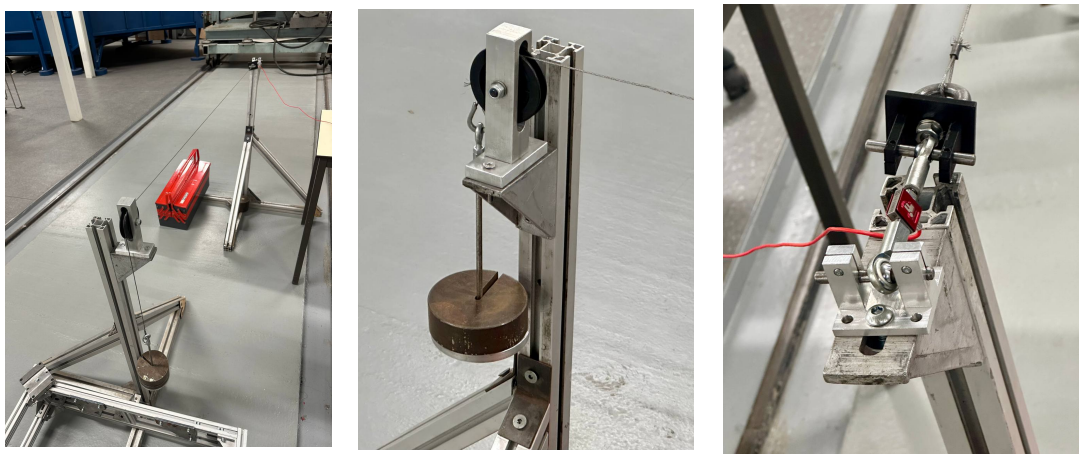

(a)

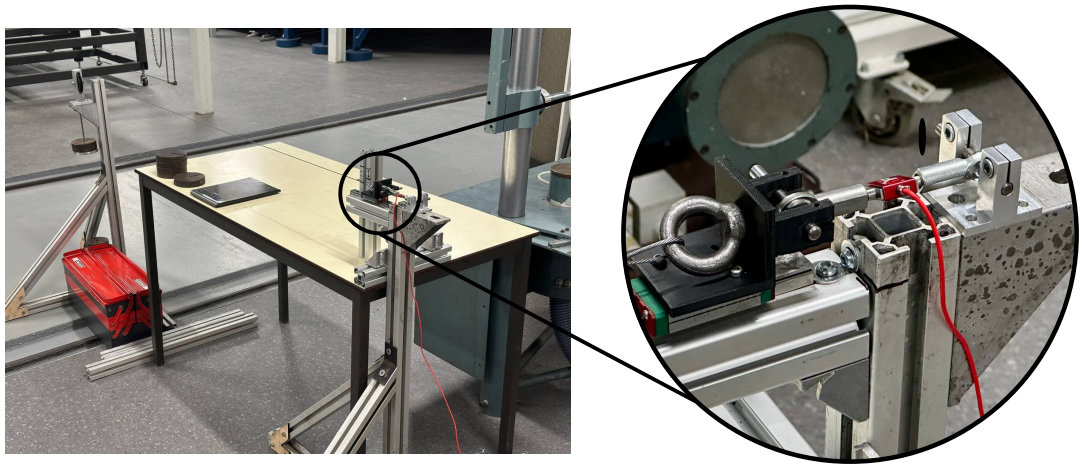

(b)

Figure 3.17: Early bench-fixture iterations that were discarded: (a) Configuration 1, horizontal cell with rod-end bearing and pulley redirect; (b) Configuration 2, added flexure on the loading-side carrier with cable over a 3D-printed pulley.

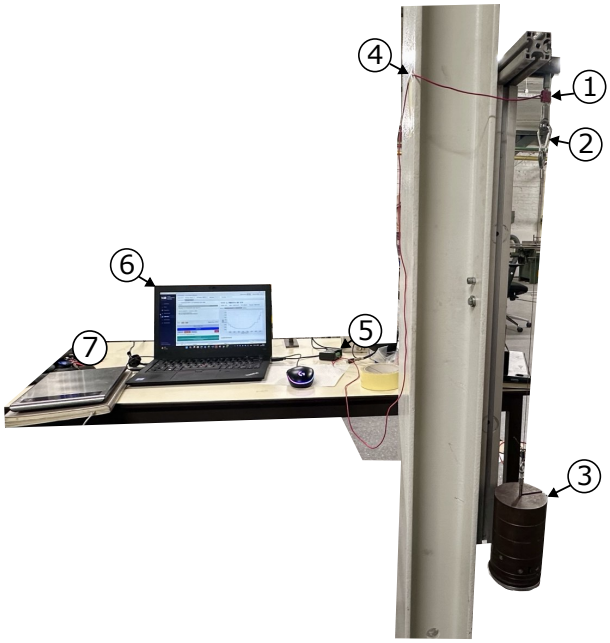

Figure 3.18: Configuration 3, the final bench fixture used for every load-cell calibration in this work. (1) FUTEK LSB201 load cell, mounted with its sensing axis vertical; (2) shackle linking the cell rod-end to the steel calibration cable; (3) aluminium calibration canister holding stacked OIML-class masses up to 9.5 kg; (4) cable-mass support pin near the top of the column, so that the cable's own weight loads the column and not the cell; (5) signal cabling from the cell to the PhidgetBridge 1046; (6) host PC running the custom calibration software; (7) precision laboratory scale used to verify each weight to within one gram before each run.

3.6.2 Cross-talk model

At the system level, the off-axis coupling is captured as a force-to-force model fitted directly from the bidirectional dead-weight runs. Each off-axis bleed picks up an intercept, a linear term, and a quadratic term per direction, in line with the AIAA R-091 calibration practice,

$$F_{ij}^{\text{bleed}}\left(F_j^{\text{meas}}\right) \;=\; a_{ij}^{(\sigma_j)} + b_{ij}^{(\sigma_j)}\, F_j^{\text{meas}} + c_{ij}^{(\sigma_j)}\, \left(F_j^{\text{meas}}\right)^2, \tag{3.2}$$

which gives twelve coefficients spread across the four direction-pairs (drag-tens, drag-comp, lift-tens, lift-comp). Collected per channel, the bleed and the corrected force then take the matrix form

$$\begin{bmatrix} F_{\text{drag}}^{\text{true}} \\ F_{\text{lift}}^{\text{true}} \end{bmatrix} = \begin{bmatrix} F_{\text{drag}}^{\text{meas}} \\ F_{\text{lift}}^{\text{meas}} \end{bmatrix} - \begin{bmatrix} 0 & F_{\text{drag,lift}}^{\text{bleed}}\left(F_{\text{lift}}^{\text{meas}}\right) \\ F_{\text{lift,drag}}^{\text{bleed}}\left(F_{\text{drag}}^{\text{meas}}\right) & 0 \end{bmatrix} \begin{bmatrix} 1 \\ 1 \end{bmatrix}, \tag{3.3}$$

where each off-diagonal entry is the polynomial of Equation 3.2 evaluated on the perpendicular measured force. The intercept a takes the constant offset at $F_j^{\text{meas}} = 0$; the quadratic c carries the load-dependent flexure of the multi-part assembly at higher loads. On the present rig, the modelled bleed stays under 2 % of the loaded force on every direction-pair, and the classical AIAA matrix-inverse step then drops out: a first-order forward subtraction is accurate to second order in the coupling magnitude. The fitted coefficients and the per-pair residuals are reported in Section 4.3.4.

3.6.3 In-situ calibration procedure

With the balance installed in the test section, the calibration sequence itself is short. The platform is first levelled with a spirit level and the bridges are zeroed at the operating pneumatic pressure of 6.5 bar. A calibrated mass is then applied through a pulley-and-rope arrangement on each axis in turn, alternating tension and compression across three load-up / unload cycles per axis. Each plateau is recorded for 30 s, of which the first 15 s is discarded as a settling allowance. Figure 3.19 shows the fixture in operation: a calibrated mass hanging from the steel cable that loads the cell directly through the bench-fixture mount. The on-axis cell response is reduced to a single sensitivity coefficient per direction,

$$F_i \;=\; s_i^{(\sigma_i)}\,\frac{V_i - V_{i,0}}{V_{\mathrm{exc}}}, \tag{3.4}$$

where $s_i^{(\sigma_i)}$ is the per-direction sensitivity in N per mV/V and $V_{i,0}$ is the zero reading captured at the start of the session. Two assumptions sit underneath the model: a linear bridge response over the loaded range, and a constant tare $V_{i,0}$ within a session. Both are verified against the zero-drift check at the end of every campaign.

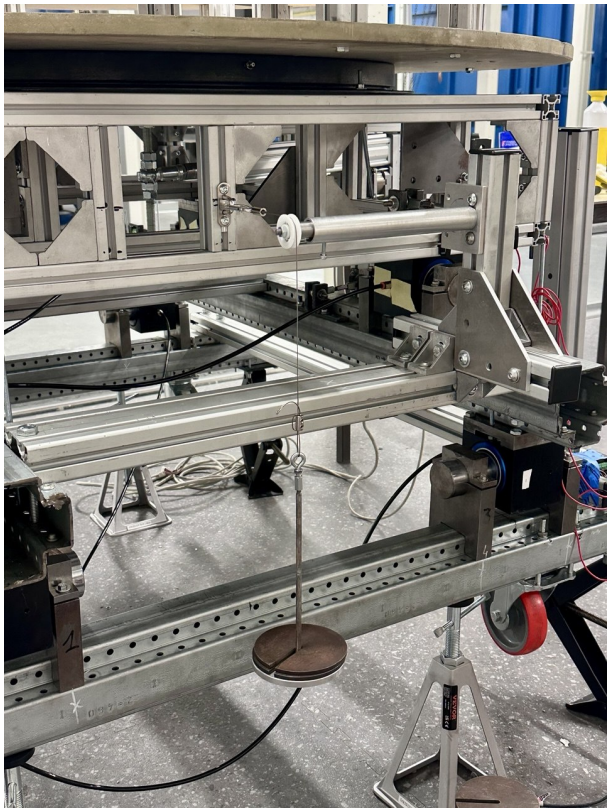

Figure 3.19: In-situ calibration fixture during a dead-weight loading run: the OIML calibration mass hangs from the steel cable that routes through the bench-fixture mount and loads the cell along its sensing axis.

3.6.4 Gravity-coupling check

Vertical-only loading runs alongside the horizontal calibration above. A known mass is hung from the platform without exciting either horizontal axis (Figure 3.20); whatever the cells then read is gravity-driven coupling, not in-plane cross-talk. Procedure and numbers are in Section 4.2.6. The residual feeds into the budget of Section 4.3.8 as a Type-B term.

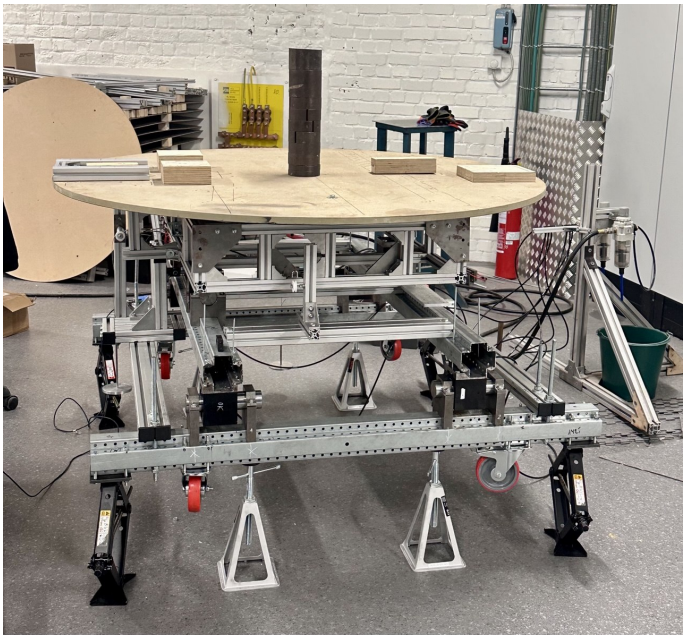

Figure 3.20: Workshop set-up for the gravity-coupling check: known dead weight stacked on the upper plate of the assembled balance.

3.6.5 Known limitation

One direction-pair (lift-compression to drag) keeps a residual of 0.87 N after the polynomial fit, an order of magnitude above the other three. The residue shape grows with the loaded force, peaks near half of full scale, and decreases at full scale: this is the signature of a load-engaged contact whose magnitude depends on the *simultaneous* value of both axes, not on the loaded axis alone. Resolving it would require a multi-axis simultaneous loading campaign that the present test schedule did not include; the residue is retained and propagated as a Type-B uncertainty contribution in the budget of Section 4.3.8.

3.7 Wind tunnel test methodology and data reduction

The calibration of Section 3.6 delivers a force in newtons in the balance frame. What remains is to put the rig in the tunnel, sweep three reference models through their operating envelope, and turn the recorded force trace into a dimensionless coefficient that can be compared to the literature. This section sets out the test environment, the three reference models, the operating points, and the chain of equations that closes the gap between a calibrated voltage and the aerodynamic coefficient reported in Chapter 4.

All wind-tunnel runs are conducted in the VUB subsonic open-circuit tunnel described in Section 2.2, with the free-stream velocity read from the upstream Pitot-static probe at the start of every plateau and the air density computed once per session from the laboratory temperature and barometric pressure. A photograph of the assembled rig installed under the tunnel test section is reproduced in Appendix E. Three reference models attach to the universal bolt pattern on the upper turntable (Section 3.3.4): the **NACA 0012** wing has a chord $c = 0.60$ m, an effective span $b = 0.942$ m, and a reference area $S = c\,b = 0.565$ m^2; the **circular cylinder** has a diameter $D = 0.25$ m and a span $L = 0.90$ m and is the same physical hardware used by Vardanyan (2023); the **vertical-axis wind turbine** is an H-Darrieus rotor whose swept area is taken from the rotor specification. The wing campaign runs at four nominal speeds, $V = 9$, 12, 15 and 18 m/s, with an angle-of-attack sweep at each speed and two independent sessions per speed for repeatability. The cylinder uses the same four speeds in a static, fixed-orientation

configuration. The turbine campaign sweeps tip-speed ratio at the rotor speed range of the controller; the operating-point list is reported in Section 4.6.

3.7.1 Data reduction

The chain from the raw bridge ratio to the aerodynamic coefficient runs in four steps.

Step 1: raw voltage to physical force. The per-direction sensitivity (Equation 3.4) and the cross-talk correction (Equation 3.2) of Section 3.6 are applied to every sample, returning the platform-frame force pair (F_{x_b}, F_{y_b}).

Step 2: platform to tunnel frame. The unified misalignment $\theta = 2.64^\circ$ rotates the platform forces into the wind-axis lift and drag through Equation 3.1 of Section 3.2.

Step 3: dimensionless coefficients. The lift and drag coefficients of the wing and cylinder use the standard definitions,

$$C_L = \frac{L}{\frac{1}{2}\rho V^2 S}, \qquad C_D = \frac{D_{\text{drag}}}{\frac{1}{2}\rho V^2 S}, \tag{3.5}$$

with the appropriate reference area S per model. The Strouhal number of the cylinder is identified from the lift-channel power spectral density,

$$St = \frac{f_s\, D}{V}, \tag{3.6}$$

where f_s is the dominant shedding frequency. The turbine uses the thrust coefficient

$$C_T = \frac{T}{\frac{1}{2}\rho V^2 A_{\text{swept}}}, \tag{3.7}$$

with A_{swept} taken from the rotor specification.

Step 4: averaging window. Each operating point is held for at least 30 s; the first 5 s is discarded as a settling allowance, and the remaining trace is reduced to a mean and a standard deviation per channel.

3.7.2 Uncertainty model

The combined standard uncertainty of every reported coefficient follows the GUM,

$$u_c^2(y) = \sum_i \left(\frac{\partial y}{\partial x_i}\right)^2 u^2(x_i), \tag{3.8}$$

expanded to $U_{95} = 2\,u_c$ for the reported coverage. The cell-level contribution is itself load-dependent,

$$u_{\text{cell}}(F) = \sqrt{a^2 + (b\,F)^2}, \tag{3.9}$$

with $a = 0.335$ N, $b = 1.77\,\%$ for the lift channel and $a = 0.456$ N, $b = 1.15\,\%$ for the drag channel, fitted from the audit residuals of the Phase II in-situ calibration. The full per-campaign budgets, including the tare drift, the velocity and the density contributions, are reported in Section 4.3.8 and in the NACA validation section of Chapter 4.

This chapter reports the data from the five-phase calibration and validation campaign defined in Chapter 3, Section 3.6: bench characterisation of each load cell (Phase 0, Section 4.1), first in-situ calibration in the workshop (Phase I, Section 4.2), refined in-situ calibration in the wind-tunnel test section (Phase II, Section 4.3), wind-tunnel validation versus the NACA 0012 airfoil and a circular cylinder in cross-flow (Phase III, Sections 4.4 and 4.5), and an application on a scale-model horizontal-axis wind-turbine rotor (Phase IV, Section 4.6). Figure 4.1 maps the phases against their deliverables. Every result block ends with a short *Discussion* paragraph in three steps: agreement with theory or literature, deviation with its quantified magnitude, and the most plausible physical mechanism. Throughout this chapter the abbreviations (t) and (c) denote the loading direction on a calibration cycle: tension and compression respectively.

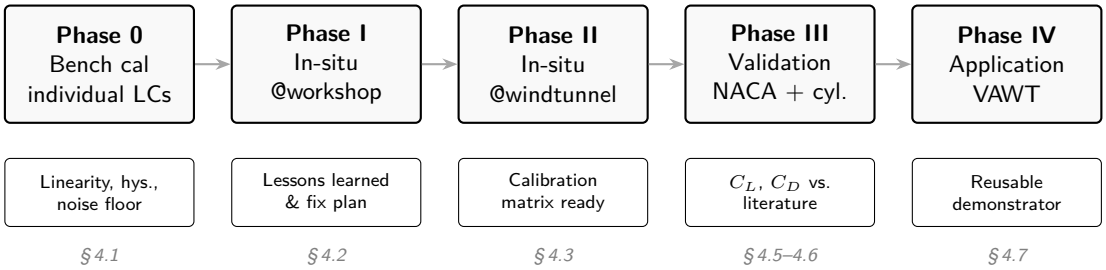

Figure 4.1: Roadmap of the chapter: bench characterisation (Phase 0), two in-situ calibrations in the workshop and in the wind tunnel (Phases I and II), validation on canonical reference cases (Phase III) and an application demonstration (Phase IV).

4.1 Bench calibration

Each FUTEK LSB201 is characterised on the dedicated bench fixture of Chapter 3, Section 3.6.1, before either cell is mounted on the balance. That separation is deliberate: with the bench result on the table as the clean transducer reference, any in-situ deviation in Phases I and II falls on the mechanical interface, the alignment, or the DAQ integration rather than on the cell itself. Across the chapter the PhidgetBridge (Phidgets Inc., 2024) runs at 128× gain and a 125 Hz sample rate. Statistical uncertainties carry Type A; Type B numbers come from the datasheet, the geometry, or prior knowledge. Both serial-number-specific factory calibration sheets are reproduced in Appendix B.1.

4.1.1 Raw signal, plateaus and creep

A load step has three time-domain phases: an unloaded baseline, a transient after weight placement, and a steady-state plateau. Post-processing trims the first 15 s of each 30 s recording and averages the remaining 1875 samples; the trim exceeds the worst observed settling time by a factor of 1.5, so the residual transient does not bias the plateau mean. Figures 4.2 and 4.3 show the three-cycle staircase per channel, with settling time growing from 2–5 s at the lightest loads to roughly 10 s at full scale. At zero load, the standard deviation over two minutes is $\sigma_V = 0.151\,\mu\text{V/V}$ on both channels, or $\sigma_F = 8.5\,\text{mN}$ at the bench sensitivity. A 3σ minimum detectable force change of 25 mN sits a factor of ten below the smallest calibration weight increment of 245 mN.

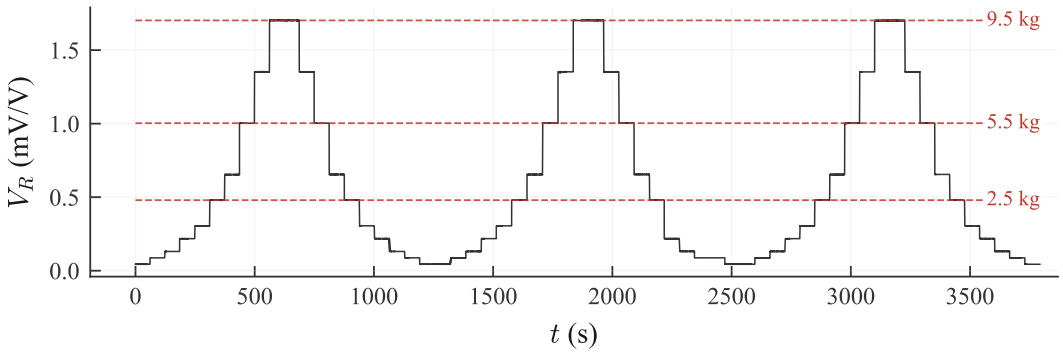

Figure 4.2: CH0 (S/N 883682) staircase voltage-ratio trace over the three ascending–descending cycles. Dashed lines mark the per-step plateau level at three representative calibration masses.

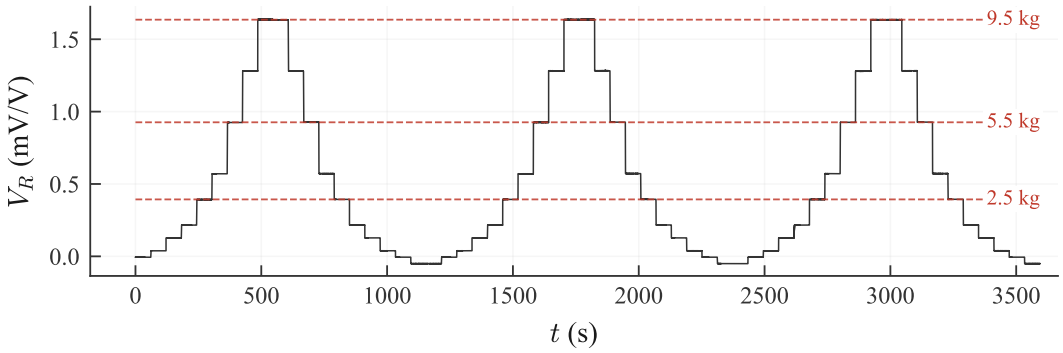

Figure 4.3: CH1 (S/N 999570) staircase voltage-ratio trace over the three ascending–descending cycles; same convention as Figure 4.2.

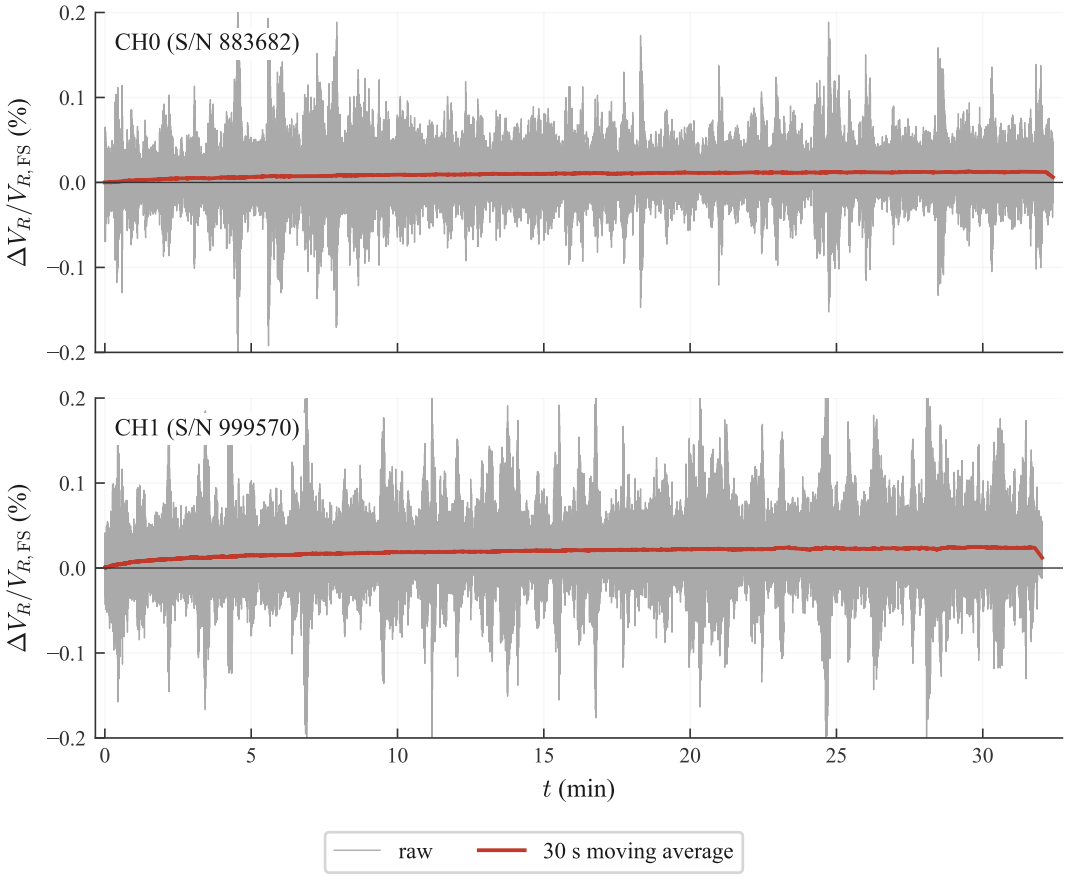

Figure 4.4: 30-min creep recording at the maximum calibration load: CH0 (top) and CH1 (bottom). Grey: raw drift relative to the first 10 s reference. Red: 30 s moving average. Y-axis zoomed to ±0.20 % FS to make the trend visible; the ±1.0 % FS visual reference sits well above this range.

Drift over time is checked separately. Each cell is loaded to the heaviest calibration plateau and the bridge output is recorded continuously for 30 minutes. Drift relative to the first 10 s reference reaches 0.008 % FS on CH0 and 0.012 % FS on CH1, well below the duration of any single calibration sweep. The 30-second moving average overlaid in red traces the slow trend underneath the bridge noise. Both channels rise monotonically in the first minutes after loading, then settle to a near-flat asymptote.

4.1.2 Calibration curves and metrics summary

An ordinary least-squares fit of the ascending plateau means against the applied reference force gives the curve for each channel. Per-cycle residuals are kept separate so hysteresis surfaces where it actually sits, not as an inflated linearity number. Linearity is therefore reported on the ascending leg alone; folding the descending residuals into the same fit would conflate the two effects and report neither one cleanly.

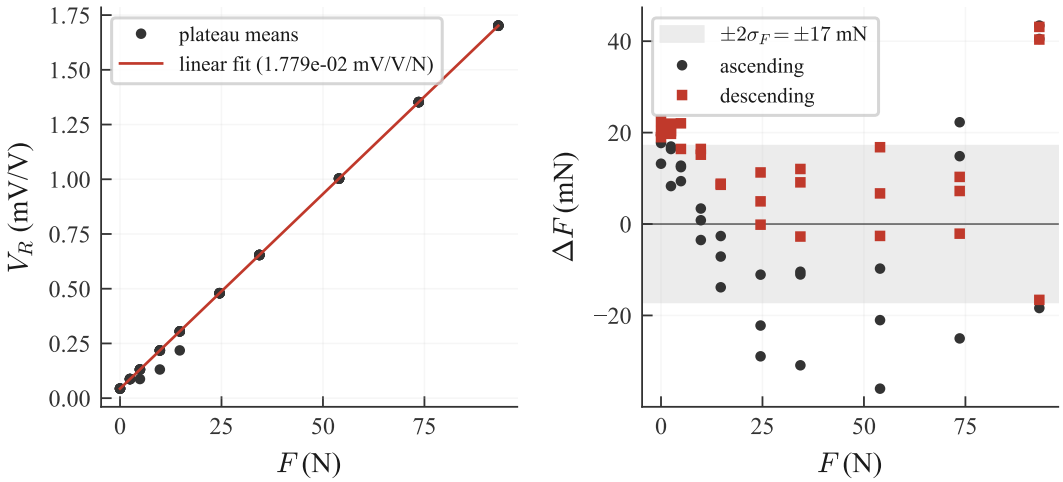

(a) CH0 (S/N 883682).

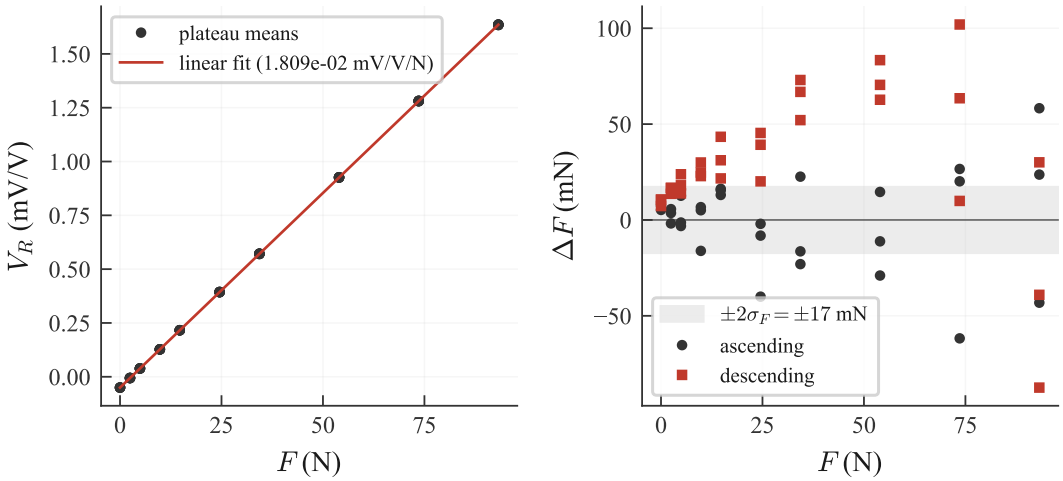

(b) CH1 (S/N 999570).

Figure 4.5: Linear least-squares fit (left) and per-cycle residuals (right) per channel. Shaded band: $\pm 2\sigma_F = \pm 17$ mN from the bench noise floor. CH0 sits inside the band; CH1 deviates at full load, source of the hysteresis in Table 4.1.

Table 4.1 reports the principal metrics for both channels. GUM uncertainty types (Joint Committee for Guides in Metrology, 2008) appear in the rightmost column. The protocol follows Bardera et al. (2024) and Reis et al. (2013).

CH0 sits at 0.046 % FS linearity, 0.041 % FS hysteresis and 0.065 % FS repeatability. CH1 matches CH0 on linearity (0.110 % FS) and repeatability (0.108 % FS) but stretches the hysteresis row to 0.156 % FS. Both cells are released to the in-situ stage; the CH1 hysteresis excess is dissected per cycle in Section 4.1.3 and its mechanism identified in Section 4.1.4.

Table 4.1: Bench calibration metrics per channel, with GUM type. Thresholds are not reported here; the comparison against the rig-level envelope is left to the discussion chapter.

Metric	CH0	CH1	GUM
R^2	0.9999997	0.9999999	-
Linearity (% FS)	0.046	0.110	B
Hysteresis (% FS)	0.041	0.156	B
Repeatability (% FS)	0.065	0.108	A
Zero drift between cycles (% FS)	0.003	0.005	A
Creep at FS over 30 min (% FS)	0.008	0.012	B
Per-cycle slope spread (%)	0.041	0.060	A
Sensitivity (mV/V per N)	1.779×10^{-2}	1.809×10^{-2}	-

Per-cycle slope spread sits at 0.04–0.06 % across the three cycles, with a relative standard error on the mean of 0.02–0.03 %. The bench therefore fixes the sensitivity of each isolated cell to within a few hundredths of a percent before either cell enters the balance.

4.1.3 Hysteresis per loading cycle

Figures 4.6a and 4.6b resolve the hysteresis $\Delta V_R/V_R(F_{\max})$ per cycle against applied force, with $F_{\max} = 93.2\,\mathrm{N}$ the heaviest calibration plateau. CH0 stays below 0.04 % across all three cycles and all force levels, with the peak at $F = 54\,\mathrm{N}$ on cycle 3. CH1 sits at the same magnitude up to $F \approx 30\,\mathrm{N}$, then climbs with load to a maximum of +0.156 % at $F = 93\,\mathrm{N}$ on cycle 1.

The CH1 envelope grows monotonically with F up to roughly 50–70 N, and the cycle-to-cycle scatter narrows at the highest loads. A load-dependent origin is therefore more plausible than a purely random one. The discussion below ties this to the rod-end interface of the bench fixture.

4.1.4 Discussion

The bench step exposes each cell on its own, before any bearing or rig coupling enters the chain. Both cells clear the gate: $R^2 > 0.9999$, linearity under 0.11 % FS, repeatability under 0.11 % FS, zero drift between cycles under 0.005 % FS. Both move on to the in-situ stage. The one number that does not line up is the CH1 hysteresis at high load, 0.156 % FS at $F = 93\,\mathrm{N}$, about four times the CH0 peak under the same protocol. Two features of the CH1 trace, the monotonic growth with load and the cycle scatter that narrows as load rises, read more naturally as residual friction in the rod-end of the bench fixture than as a defect of the transducer itself. The fault is at the interface, not the cell.

When the rod-end on the lift channel of the in-situ rig is swapped for a clamp (Section 4.2.9), the lift-channel hysteresis drops by roughly a factor of three. What remains is carried as a Type B uncertainty of 0.078 % FS, half the measured value, and propagated into the budget of Section 4.3.8. One caveat on this number: the bench fixture pulls but cannot push, so only the tension branch is logged here; bridge symmetry is taken from the LSB201 construction and re-checked in the bidirectional Phase I campaign of Section 4.2.3.

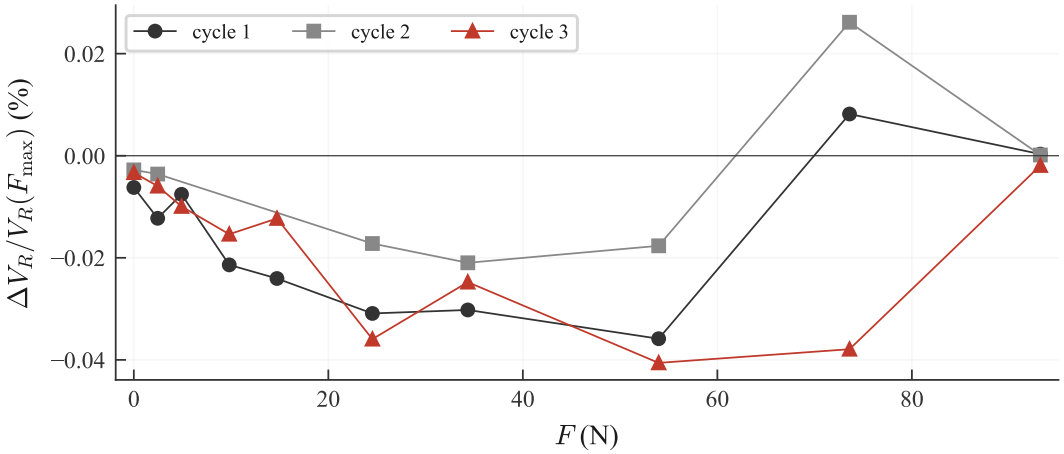

(a) CH0 (S/N 883682).

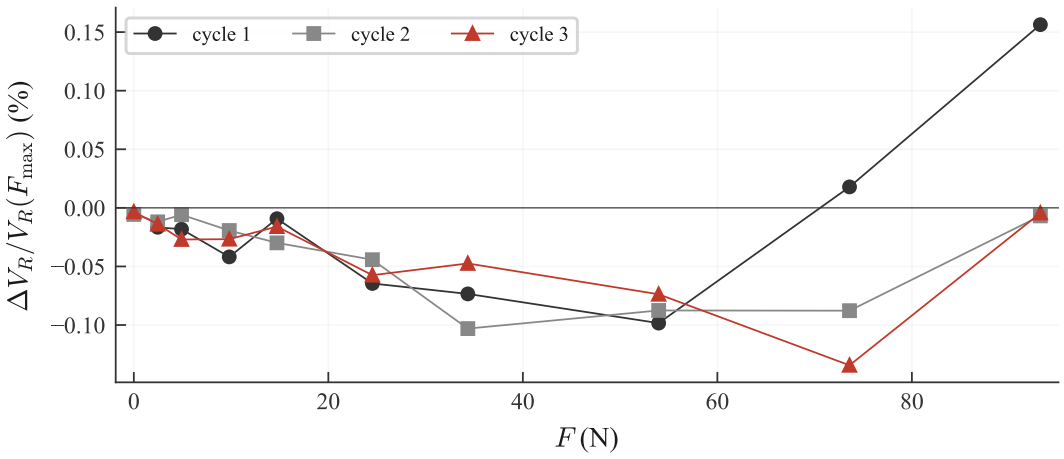

(b) CH1 (S/N 999570).

Figure 4.6: Hysteresis $\Delta V_R/V_R(F_{\max})$ at each force level, resolved per cycle. CH0 stays within 0.04 % across all loads; CH1 grows monotonically and reaches +0.156 % at $F = 93$ N.

4.2 Preliminary in-situ calibration

With both cells installed in the rig, the calibration is repeated as a system-level dead-weight campaign in the workshop. Each axis is now characterised end-to-end with loading-direction symmetry, cross-talk and off-axis behaviour all measured in the same session. The same baseline (Sections 4.2.1–4.2.6) is rerun later in the wind-tunnel test section (Section 4.3). Two closing subsections (Sections 4.2.8 and 4.2.9) cover specific principles that this campaign exposed. The goal of Phase I is therefore not the calibration itself but the lessons it produces: every conclusion drawn here is carried into the tunnel campaign of Section 4.3 and re-verified there, so the rig moves from workshop to tunnel through one continuous chain of evidence.

4.2.1 Bridge stabilisation

Every session opens with a bridge-stabilisation step: PhidgetBridge (Phidgets Inc., 2024) excitation is held on with zero applied load, and the drift is monitored over consecutive 60-s windows. The session is released once the most recent window falls below $1\,\mu$V/V. Here the criterion is reached at $0.61\,\mu$V/V on CH0 and $0.03\,\mu$V/V on CH1.

4.2.2 Pre-calibration checks

A short inspection list runs after warm-up and before the first weight is placed. The measured values are listed in Table 4.2.

Table 4.2: Pre-calibration checks at the start of the preliminary in-situ session.

Quantity	Value	Method
CH1-axis tilt β_1	$-0.15°$	Inclinometer ($\pm0.05°$)[a]
CH0-axis tilt β_0	$+0.20°$	Inclinometer ($\pm0.05°$)
Cable-to-axis angle, dead-weight rig	$\leq 1°$	Set square, geometrically bounded
Load-cell placement angle	$\leq 1°$	Set square, geometrically bounded
Alignment with N_0	Within visual tolerance	By eye, against rig reference edge
Air-bearing manifold pressure	5.0 / 6.5 bar	Manifold gauge
Ambient temperature	21.5 °C	Single reading at session start
Float breakaway friction	Geometrically bounded	Type B, see Section 4.3.8

[a]Laserliner MasterLevel Compact Plus, datasheet accuracy.

Both tilts give $\cos\beta > 0.99999$, so the obliquity loss on each axis stays below 6×10^{-4} % and the projection is treated as unity. The two supply pressures listed in Table 4.2 reflect an earlier methodology decision (Section 3.4): raising the manifold from 5.0 to 6.5 bar reduced the off-axis slope spread from 9.1 % to 0.30 % between $W = 0$ and $W = 8.7$ kg, and all Phase I data reported below use the 6.5 bar supply. The same checklist runs at the start of every subsequent calibration.

4.2.3 In-situ CH1 calibration

This section determines whether the bench-level sensitivity, linearity and repeatability of CH1 (Section 4.1) transfer to the assembled rig, and sets the bidirectional reference against which the wind-tunnel re-calibration of Section 4.3 is read. CH1 is calibrated in compression and tension with both cells installed, following the dead-weight protocol of Chapter 3, Section 3.6.3 (multi-cycle ascending–descending, in line with the in-situ practice of Bardera et al. (2024) and Reis et al. (2013)). Both channels are recorded in each session so that the cross-talk slope of Section 4.2.5 draws from the same data. Three figures on the next page summarise the result. The corresponding numbers appear in Table 4.3. The ±2 % FS reference band used throughout this chapter is the system-level acceptance limit of AIAA R-091:2002; ISO 376 sets the tighter ±0.5 % for the cell alone.

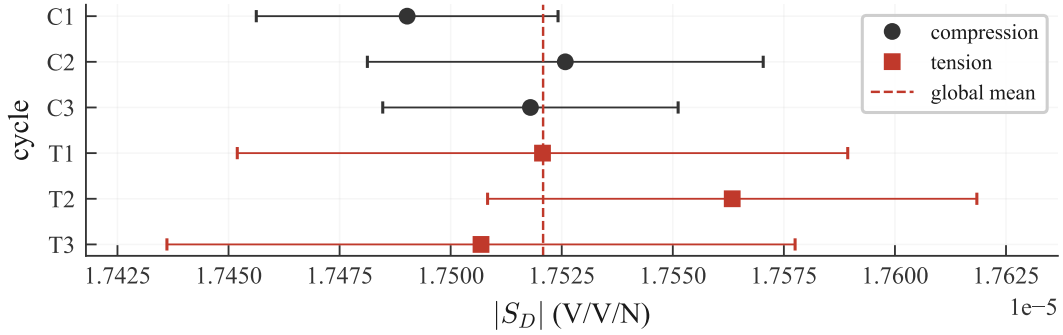

(a) Per-cycle slope magnitudes with OLS standard errors. The global mean across the six fits is the red dashed vertical.

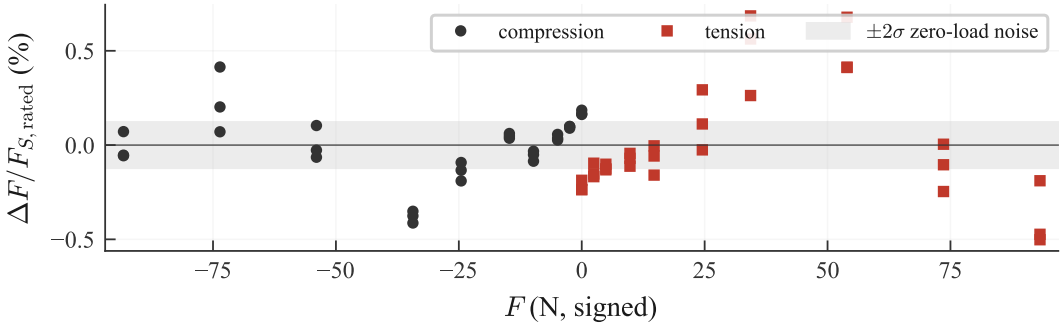

(b) Residual of each ascending plateau against the linear fit, in percent of $F_{S,\mathrm{rated}}$. Compression on the negative side, tension on the positive. Shaded band: $\pm 2\sigma$ zero-load noise.

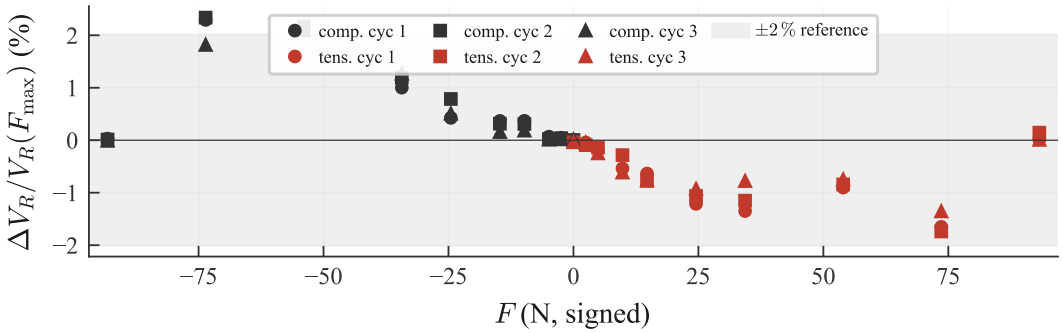

(c) Cycle-resolved hysteresis $\Delta V_R/V_R(F_{\mathrm{max}})$ against signed applied force. Shaded band: $\pm 2\,\%$ reference envelope.

Figure 4.7: Phase I drag-axis calibration of CH1: per-cycle slope reproducibility (top), ascending-plateau residuals against the linear fit (middle), and cycle-resolved hysteresis (bottom).

Table 4.3: CH1 baseline, per loading direction.

Quantity	**Compression**	**Tension**
Slope $\lvert S_D \rvert$ (V/V/N)	1.7511×10^{-5}	1.7530×10^{-5}
R^2	0.999962	0.999885
Per-cycle slope spread (%)	0.20	0.32
Zero-load force-equivalent noise (mN)	45	66
Hysteresis, mean (%)	0.67	0.61
Hysteresis, peak (%)	2.34	1.74
Global mean $\lvert S_D \rvert = 1.7521 \times 10^{-5}$ V/V/N; direction asymmetry 0.11 %.		

Discussion. Across both branches the linear fits return $R^2 > 0.9998$, with per-cycle slope spreads of 0.20 % in compression and 0.32 % in tension. All six slopes overlap the global mean within their OLS standard errors. The direction-resolved sensitivities differ by only 0.11 %. That is the bidirectional symmetry the air-bearing topology is expected to deliver, and it survives the transition from bench to rig. The in-situ magnitude of 1.7521×10^{-5} V/V/N reaches 96.9 % of the Phase 0 bench value of 1.809×10^{-5} V/V/N (Section 4.1). That is a 3.1 % transmission loss attributable to compliance in the bearing-clamp interface and the rod-end bushings between cell and platform.

Per-cycle hysteresis stays inside the ±2 % reference envelope over the full force range, with a single excursion: the 7.5 kg point on the compression branch peaks at 2.34 %. At zero load the cell reads 45 mN noise in compression, 66 mN in tension. Both are above the bench floor of $\sigma_F \approx 8.5$ mN, which is expected once the air-bearing supply and ambient floor coupling sit in the chain. The 30-min creep test at full load returns 0.083 N of residual drift, two decades below the 111.2 N rated full-scale. Nothing on the drag baseline departs from what the bench predicted; the bidirectional extension simply mirrors that result.

4.2.4 In-situ CH0 calibration

This section determines whether the CH0 bench reference of Section 4.1 transfers to the assembled rig, and isolates the mechanism that breaks that transfer in the present workshop campaign. CH0 is calibrated bidirectionally with the same dead-weight protocol of Chapter 3, Section 3.6.3 (Bardera et al., 2024; Reis et al., 2013). A mechanical change in the CH0 bearing stage between the early and the final runs separates two states of the rig (pre-fix and post-fix), characterised here and resolved mechanically in Section 4.2.9.

Figure 4.8 on the next page shows the four cycle-groups, the residuals against the per-direction linear fit on the pre-fix consistent dataset (compression run plus mean of the two same-day tension runs), and the cycle-resolved hysteresis on that same dataset. The headline numbers move into Tables 4.4 and 4.5.

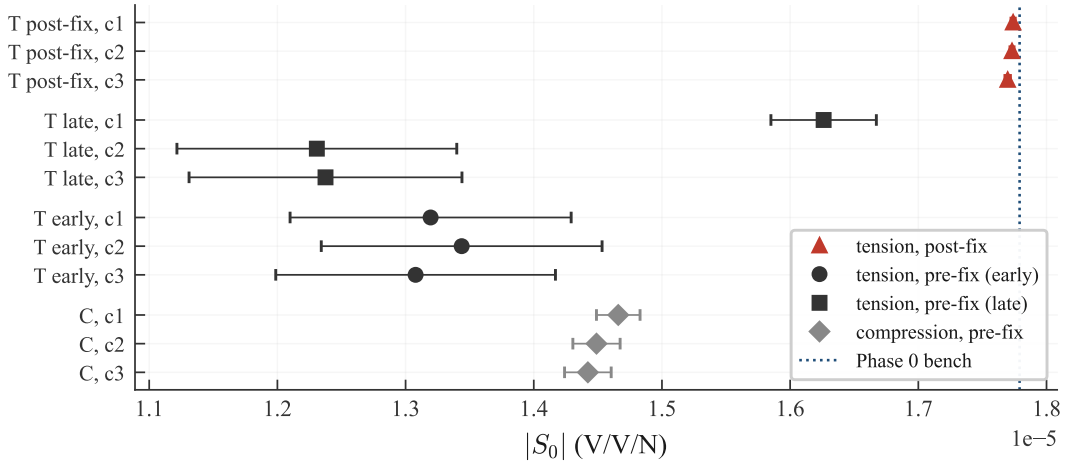

(a) Per-cycle slope magnitudes with OLS standard errors for every CH0 loading run, against the Phase 0 bench reference (blue dotted). The three pre-fix groups sit to the left; the post-fix tension run lies on the bench reference.

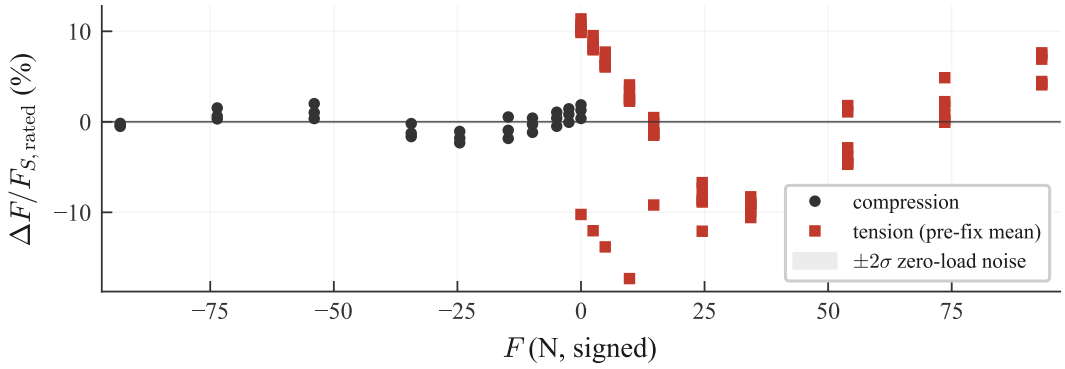

(b) Residual of each ascending plateau against the per-direction linear fit on the pre-fix consistent CH0 dataset. Compression on the negative side, tension on the positive. Shaded band: $\pm 2\sigma$ zero-load noise.

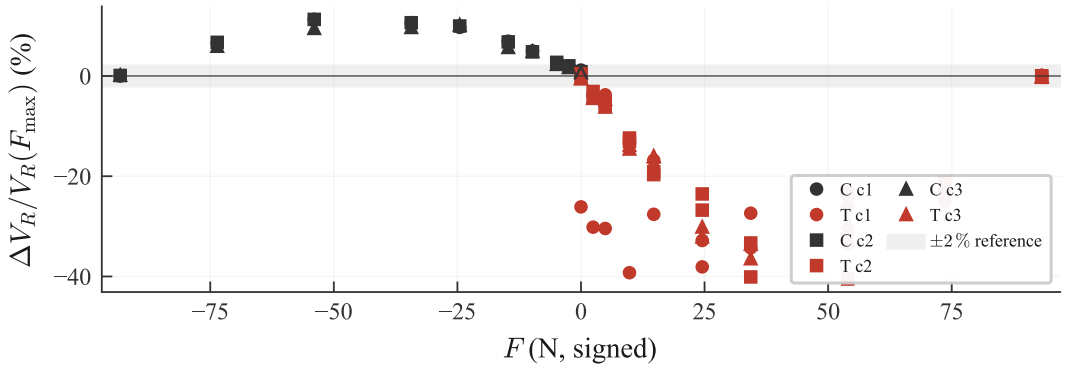

(c) Cycle-resolved hysteresis $\Delta V_R/V_R(F_{\max})$ against signed applied force, pre-fix dataset. Shaded band: $\pm 2\,\%$ reference envelope.

Figure 4.8: Phase I lift-axis calibration of CH0: per-cycle slope reproducibility across pre- and post-fix runs (top), ascending-plateau residuals on the pre-fix consistent dataset (middle), and cycle-resolved hysteresis on the same dataset (bottom).

Table 4.4: Tension-run consistency on CH0. Ratios are computed on the merged ascending-branch slope of each run.

Comparison	**Ratio**	**Difference**
Tens early vs Tens late (both pre-fix, same day)	97.0 %	3.0 %
Pre-fix tension mean vs Tens post-fix (run 4)	75.9 %	24.1 %
Tens post-fix vs Phase 0 bench reference	99.6 %	0.4 %

Table 4.5: CH0 baseline in the pre-fix state, per loading direction.

Quantity	**Compression**	**Tension (early+late)**
Mechanical state	pre-fix	pre-fix
Slope $\lvert S_0 \rvert$ (V/V/N)	1.4523×10^{-5}	1.3443×10^{-5}
R^2	0.9983	0.9321
Per-cycle slope spread (%)	1.63	3.0[a]
Zero-load force-equivalent noise (mN)	17	22
Hysteresis, mean (%)	5.4	17.8
Hysteresis, peak (%)	11.3	40.5
Transmission ratio vs bench (%)	81.6	75.6

[a]Between-run, not within-run; see Table 4.4.

Discussion. Two pre-fix tension runs on the same day disagree by 3.0 % in slope, and the merged-tension mean sits 24.1 % below the bench reference of Section 4.1. The compression branch sits 18.4 % below. Hysteresis runs an order of magnitude above the ±2 % envelope on both branches (peak 11.3 % in compression, 40.5 % in tension), and the ascending residuals reach ±17 % $\mathrm{FS}_{\mathrm{rated}}$ at low force. The signature is mechanical, not electrical. A clamped element in the 4+3 asymmetric CH0 bearing stage releases stick-slip at every plateau.

The bearing intervention of Section 4.2.9 clears it: a small custom plate clamps the lone stage 2 bushing at its housing, so the trapped moment unloads at the single contact instead of sticking there. The post-fix tension run (run 4) then returns to 99.62 % of the bench reference with $R^2 = 0.99999$ on the same protocol. CH0 is mechanically restored. The pre-fix dataset above survives in the analysis solely as the input to the interaction matrix of Section 4.2.5; bidirectional symmetry on the corrected rig is the subject of Section 4.3, where the wind-tunnel campaign reads the post-fix balance.

4.2.5 Cross-talk and interaction matrix

This section measures how much one loaded axis bleeds into the unloaded channel and assembles the linear interaction matrix used by the early-development pipeline. The diagonal sensitivities of Sections 4.2.3 and 4.2.4 are read against the four off-diagonal force-bleed coefficients fitted on the same in-situ campaign. Phase II later replaces this linear matrix with the polynomial cross-talk form of Section 4.3.4.

The four signed force-bleed fractions are M_{01} when CH1 is loaded and CH0 bleeds, and M_{10} when CH0 is loaded and CH1 bleeds, each resolved by loading direction. Table 4.6 gives the values and Figure 4.9 plots them against the ±2 % FS reference envelope used throughout this chapter. CH1-axis direction symmetry is 0.11 % (Table 4.3); CH0 carries a 7.4 % direction asymmetry in the pre-fix state that the per-direction matrix coefficients preserve rather than smooth out.

Table 4.6: Phase I direction-resolved interaction-matrix coefficients, pre-fix consistent.

Coefficient	Loaded → unloaded	Loading	Value
$M_{01}^{(t)}$	CH1 → CH0	Tension	−1.68 %
$M_{01}^{(c)}$	CH1 → CH0	Compression	+0.96 %
$M_{10}^{(t)}$	CH0 → CH1	Tension	+0.10 %
$M_{10}^{(c)}$	CH0 → CH1	Compression	+0.45 %

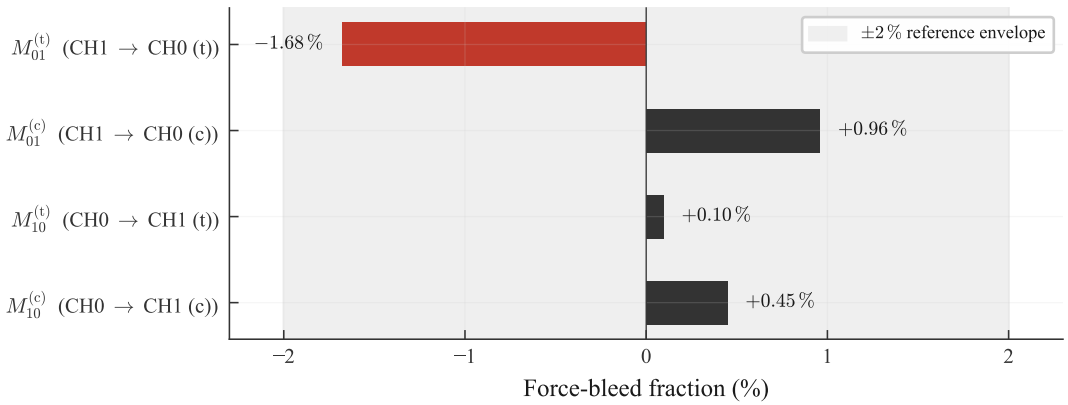

Figure 4.9: Signed direction-resolved interaction coefficients for Phase I, in per cent of force bleed. Shaded band: ±2 % FS reference envelope. The sign change of M_{01} between (t) and (c) reflects the pulley-geometry reversal of the cable load path.

Discussion. All four coefficients fit inside the ±2 % envelope. The dominant coupling on the rig is CH1-tension → CH0 at −1.68 %. There is a sign reversal between CH1 tension and CH1 compression; that one is geometric, not a measurement artefact. When the loading direction flips, the dead-weight pulley moves to the other side and the residual side-moment changes sign with it. The direction-resolved formulation carries that sign through into the runtime matrix selection.

M_{10} stays small (≤ 0.45 %), and the reason is simple: the clamped CH0 bearing of the pre-fix state stiffens the platform and damps cross-axis transmission. This linear matrix is the cross-talk correction the early-development pipeline used. Once Phase II adds an intercept term and a quadratic load-dependence to the coupling, after the bearing intervention and the wind-tunnel install, the polynomial form of Section 4.3.4 takes over.

4.2.6 Gravity coupling

This section measures how much a pure vertical load on the platform leaks into the horizontal channels. A perfectly decoupled balance reads zero on both regardless of the weight; any non-zero output is parasitic. Five vertical loads ($W = 0$, 2, 6, 14, 22.7 kg) are cycled up–down three times with both horizontal channels recorded throughout (Figure 4.10).

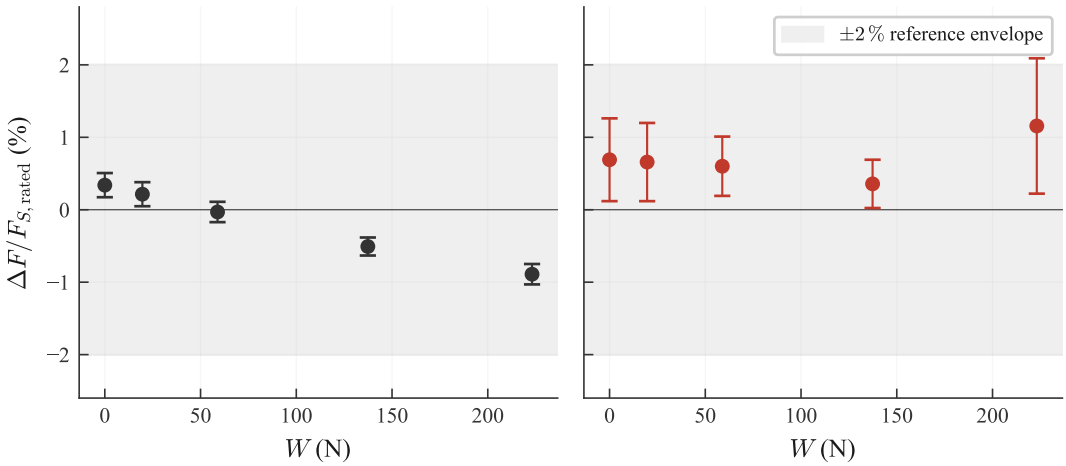

Figure 4.10: Horizontal-channel coupling against vertical load: CH0 (left), CH1 (right). Markers are the mean over three loading cycles (6 plateaus per load); error bars are the across-plateau standard deviation. Shaded band: ±2 % FS reference envelope.

Numbers at full load ($W = 22.7$ kg): CH0 mean $-0.89\,\%\,\mathrm{FS}_{\mathrm{rated}}$, $\sigma = 0.14\,\%$. CH1 reads $+1.16\,\%\,\mathrm{FS}_{\mathrm{rated}}$, $\sigma = 0.93\,\%$. One CH1 plateau crosses to $+2.34\,\%$, but the mean still sits inside the ±2 % envelope. Implied platform tilts via $\sin^{-1}\left(F_{\mathrm{coupling}}/W\right)$ are added in Table 4.7, with F_{coupling} converted through the Phase 0 bench slope of the relevant channel.

Table 4.7: Gravity coupling statistics at $W = 22.7$ kg.

Channel	Mean (% FS)	σ (% FS)	Peak (% FS)	Tilt [a]	Inclinometer [b]
CH0	−0.89	0.14	−1.07	0.25°	+0.20°
CH1	+1.16	0.93	**+2.34**	0.33°	−0.15°

[a] Implied from the cycle mean via $\sin^{-1}\left(F_{\mathrm{coupling}}/W\right)$. [b] Static inclinometer reading from Section 4.2.2.

Discussion. CH0 passes the check. The mean sits inside the ±2 % envelope by a factor of two, and the implied tilt of 0.25° matches the inclinometer reading of +0.20° within accuracy. CH1 stays inside the envelope on the mean (+1.16 %) but one plateau crosses to +2.34 %, the cycle spread is six times wider than on CH0, and the implied tilt of 0.33° disagrees with the inclinometer reading of −0.15° in both sign and magnitude. The CH1 response is therefore not a platform-tilt effect.

The source is the CH0 bearing-stage; three lines of evidence point at it. First, the $M_{10}^{(\mathrm{c})}$ coefficient of Section 4.2.5 predicts 1.00 N of CH1 bleed at $W \cdot g = 223$ N, which the observed cycle mean of 1.29 N matches inside 30 %. Second, the off-axis check of Section 4.2.7 picks up a 0.30 % CH1-slope modulation under vertical load, the signature of crosstalk routed via the CH0 stage. Third, the cycle-spread is tight on CH0 and loose on CH1, which mirrors the asymmetric 4+3 bushing layout analysed in Section 4.2.9. Three threads, one stage. The bearing intervention of that section is the same root-cause fix.

4.2.7 Off-axis sensitivity

This section measures whether the CH1 calibration slope changes when a static vertical weight is placed on the platform: a perfectly decoupled air-bearing balance must return the same slope under any W, and any sensitivity exposes binding, friction asymmetry or geometric coupling between the two bearing stages (Ostafichuk and Green, 2002). The protocol places a known weight on CH0 first, then runs a standard CH1 dead-weight sweep through the cable-and-pulley fixture, and fits the CH1 slope as usual. The result is read against the published cycle-to-cycle slope spread of Ostafichuk and Green (2002), who report 0.18 % across 11 trials with varied vertical loads on a comparable air-bushing balance.

Table 4.8: Off-axis sensitivity check on CH1 at 6.5 bar supply pressure.

Vertical load W (kg)	$\lvert S_1 \rvert$ **(V/V/N)**	R^2	**Deviation**
0	1.7975×10^{-5}	0.99993	reference
8.74	1.8030×10^{-5}	0.99965	+0.30 %
Spread 0.30 %; reference 0.18 % from Ostafichuk and Green (2002).			

The two-load measurement gives a CH1-slope spread of 0.30 % between $W = 0$ and $W = 8.74$ kg, with $R^2 \geq 0.9996$ on both fits (Table 4.8). That sits a factor 1.7 above the Ostafichuk reference of 0.18 % on a comparable two-axis air-bushing balance.

Discussion. The slope spread of 0.30 % is well inside the 1 % acceptance margin the rig is designed for, but it sits 1.7× above the Ostafichuk reference. The position is honest: the present balance is in the middle of the published distribution, neither best-in-class nor unfit.

Two completeness gaps are carried into Phase II. The protocol nominally calls for a third vertical-load point near 4–5 kg to confirm linearity of the load-vs-slope dependence; that point was not recorded in the workshop. The complementary CH0 off-axis check (a vertical sweep on CH0 while a horizontal weight sits on CH1) was not performed either because the CH0 bearing was in the pre-fix state of Section 4.2.9. Both items are scheduled for the wind-tunnel campaign of Section 4.3.

4.2.8 Compressor noise

A first workshop run, lab compressor sitting on bare concrete, exposed a problem: the iterative tare of Section 3.6.3 would not converge inside its 50-step ceiling. Two changes fixed it. The compressor was moved onto a vibration-isolation mat; the supply pressure was bumped from 5.0 to 6.5 bar. Both were in place before any of the data above were recorded. What this subsection does is quantify what those two changes bought.

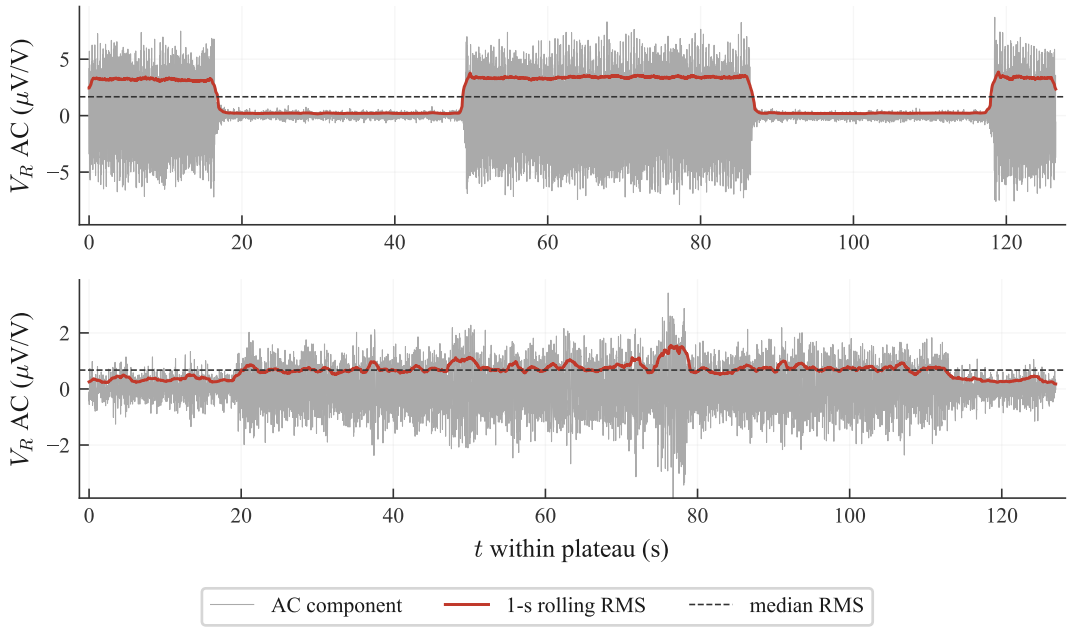

Figure 4.11: Longest zero-load CH1 rest plateau ($\sim$ 126 s). Top: pre-mitigation, median RMS = 1.67 μV/V. Bottom: post-mitigation, median RMS = 0.67 μV/V.

The pre-mitigation panel shows the compressor cycling on the bridge baseline: the rolling RMS jumps to roughly 3–4 μV/V whenever the motor runs, then settles back to the median during idle. The post-mitigation panel collapses that swing onto a near-flat band around 0.7 μV/V; the compressor cycle is still present but its imprint on the bridge stays inside the noise floor of the cell itself. Table 4.9 reports the headline statistics.

Table 4.9: Baseline-noise statistics on the zero-load CH1 voltage ratio.

Configuration	**Median RMS** (μV/V)	**Peak RMS** (μV/V)	**High-noise duty** (%)
Pre-mitigation (5 bar, no mat)	1.67	3.87	49
Post-mitigation (6.5 bar, mat)	0.67	1.56	6
Reduction	×2.5	×2.5	×8

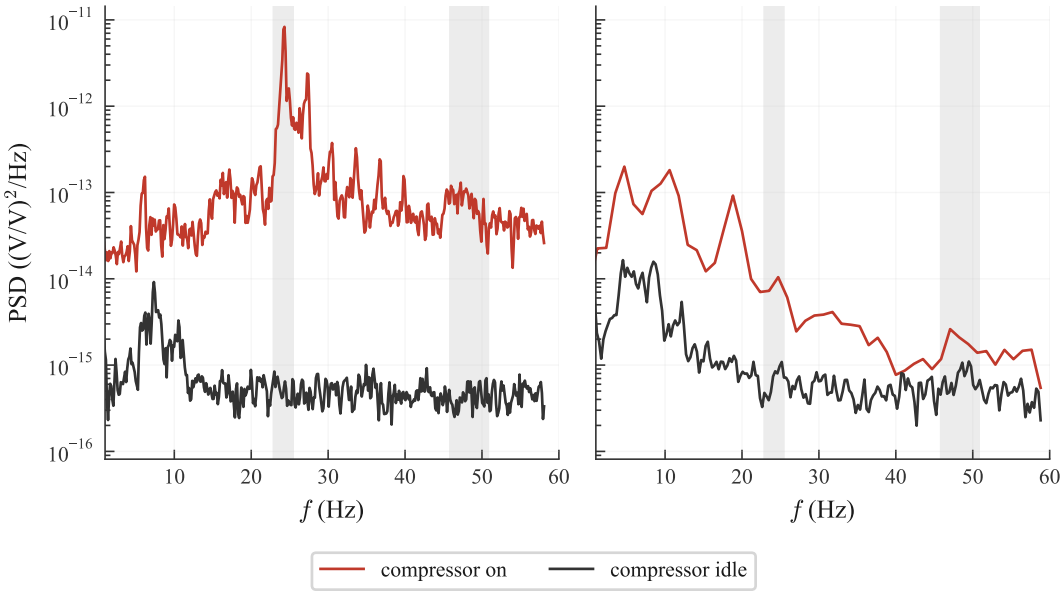

Figure 4.12: Power spectral density of the zero-load CH1 signal, segmented by the rolling-RMS criterion. Red: compressor-on epochs; dark: compressor-idle epochs. Shaded bands: compressor rotation $f_1 \approx 24\,\text{Hz}$ and piston harmonic $f_2 \approx 48\,\text{Hz}$ at a nominal 1450 RPM. Left: pre-mitigation; right: post-mitigation.

Discussion. The segmented PSD localises the gain inside the 20–50 Hz compressor band: the red (compressor-on) curve sits clearly above the dark (idle) curve inside both shaded harmonics, and the gap collapses outside that band. After mitigation the two curves move closer together and the absolute level drops by an order of magnitude across the same frequencies. The compressor harmonics sit well above the bandwidth of any static aerodynamic measurement, so a low-pass cutoff at $f_c \leq 20\,\text{Hz}$ on the time-domain bridge output removes the residual signature without affecting the signal of interest (Bardera et al., 2024). The same configuration is used for the wind-tunnel campaign of Section 4.3, where the compressor sits at $\sim 6\,\text{m}$ from the rig instead of $\sim 3\,\text{m}$ in the workshop.

4.2.9 Bearing-stage asymmetry analysis

The rig uses two stacked linear bearing stages oriented perpendicular to each other (Figure 4.13): stage 1 carries the CH1 axis, stage 2 carries CH0, each originally fitted with four NewWay porous-graphite air bushings (New Way Air Bearings, 2006). During the pre-calibration walk-through one stage 1 bushing was found contaminated and removed. Stage 1 carries the full vertical reaction of the rig, so it had to keep four bushings; the lighter stage 2 surrendered one to bring the operational configuration to $4 + 3$.

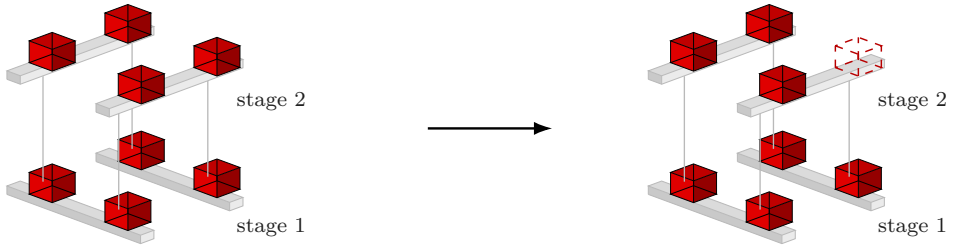

Figure 4.13: Bearing layout of the two stages: (a) the original $4+4$ configuration; (b) the operational $4 + 3$ configuration after one bushing was transferred from stage 2 to stage 1. The dashed outline in panel (b) marks the original position of the transferred bushing.

Going from $4 + 4$ to $4 + 3$ left one rail of stage 2 with a single contact where the other carried two. That lone bushing then absorbed every upstream moment by itself, and stick-slip friction at the zero-crossing of the load was the result (see the CH0 compression branch in Figure 4.8c). The fix was a small custom plate welded onto the upper mount. It clamps the asymmetric bushing at its housing rather than rigidly fixing it to the frame, so the moment unloads at the single contact instead of sticking there. Recovery on CH0 is quantified in Table 4.10. What is left over is a rocking mode, carried forward as a Type B term in the budget of Section 4.3.8.

Table 4.10: CH0 tension-branch metrics: pre-fix and post-fix states.

State	$\lvert S_0 \rvert$ (V/V/N)	Transmission	R^2	Hyst. peak (%)
Pre-fix tension	1.3443×10^{-5}	75.6 %	0.9321	36.9
Post-fix (run 4)	1.7722×10^{-5}	99.6 %	0.99999	0.8

The two contrast figures on the next page complete the picture: Figure 4.14 shows the ascending-residuals collapse from $\pm 9\,\%\,\mathrm{FS}_{\mathrm{rated}}$ into the $\pm 2\,\%$ envelope, and Figure 4.15 shows the cycle-resolved hysteresis dropping from a 37 % peak to below 1 %.

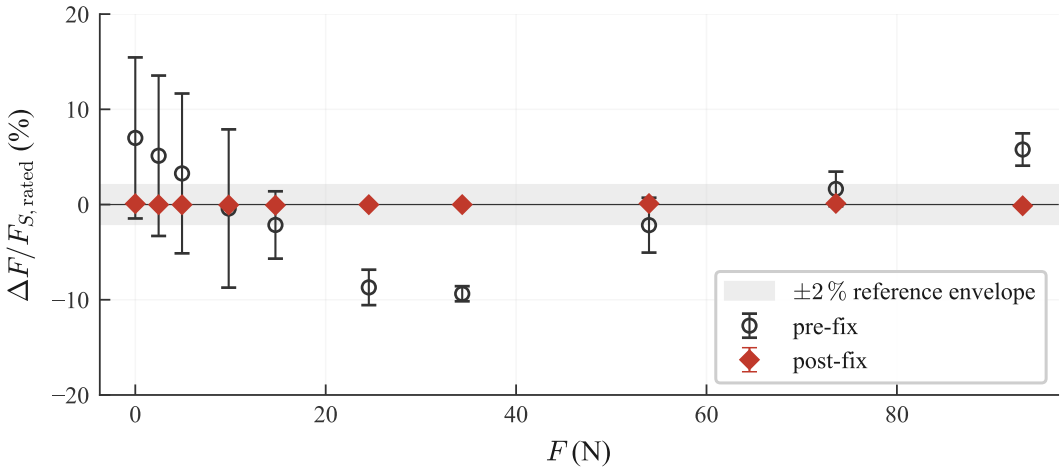

Figure 4.14: Per-force-level mean ± cycle σ of $\Delta F/F_{S,\mathrm{rated}}$ on the ascending tension branch. Open grey circles: pre-fix; red diamonds: post-fix run 4. Shaded band: ±2 % FS reference envelope.

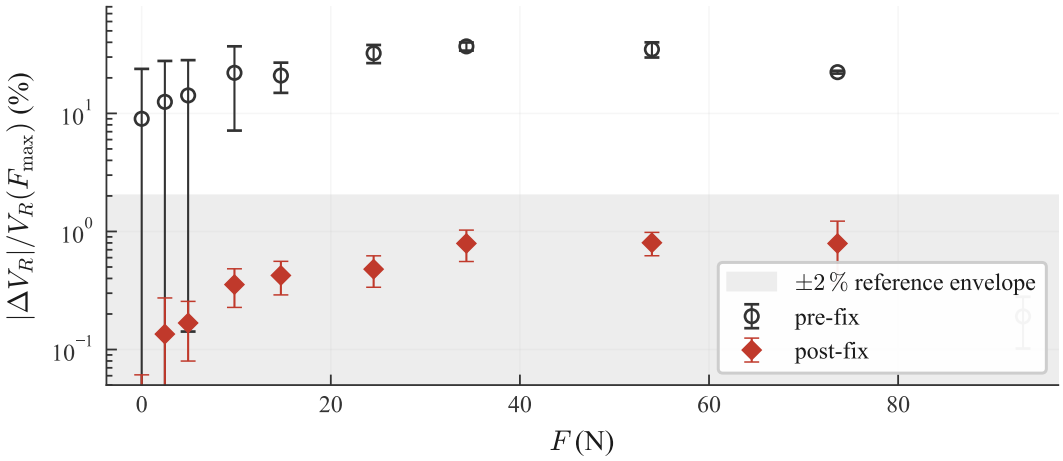

Figure 4.15: Per-force-level mean ± cycle σ of $|\Delta V_R|/V_R(F_{\max})$ on the tension branch (log y-axis). Open grey circles: pre-fix; red diamonds: post-fix run 4. Shaded band: ±2 % reference envelope.

4.3 Wind-tunnel in-situ calibration

Phase II is the calibration that the wind-tunnel applications of this chapter actually use: the cylinder benchmark, the turbine reference and the NACA 0012 polar. The bearing intervention of Section 4.2.9 is in place, the compressor sits at roughly 6 m from the rig on a vibration mat instead of 3 m on bare floor, and the rig itself is mounted in the tunnel test section (Figure 4.16). The mounting fixes the physical interpretation of each cell: one bridge reads the force along the flow direction (*drag*) and the other reads the horizontal component perpendicular to it. That second component is a side-force in the strict sense, but the name *lift* is kept for continuity with Section 4.2. A residual angle θ between the balance principal axes and the tunnel frame is unavoidable. The rig carries a dedicated alignment mechanism that brings θ down to a small but non-zero residual. Section 4.3.6 then measures this residual and folds it into the conversion pipeline.

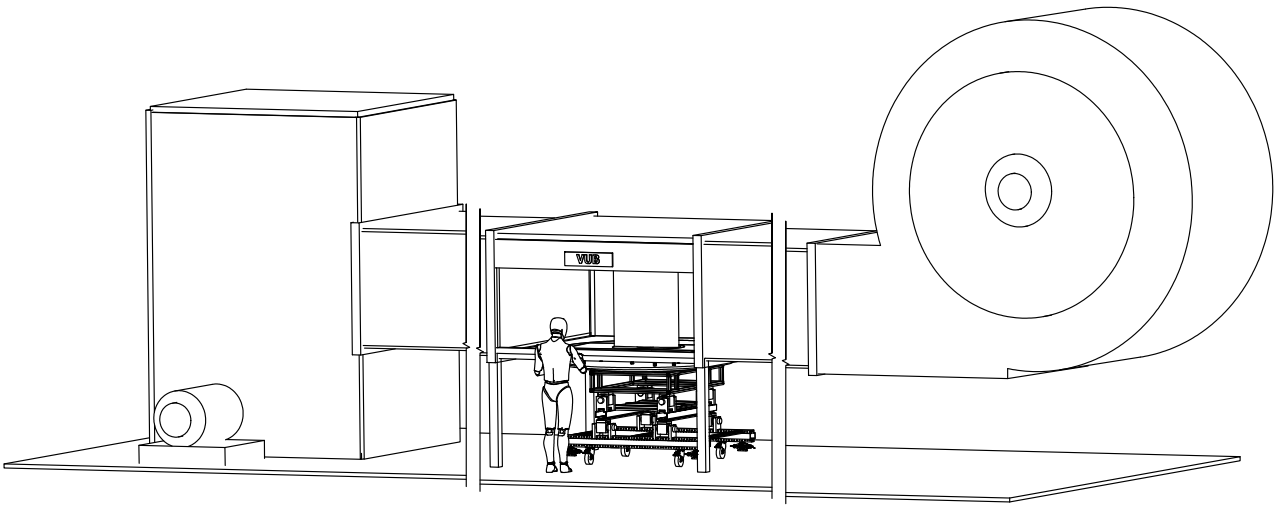

Figure 4.16: Wind-tunnel installation. The rig with the scissor lift and the balance under the model sits in the open test section of the VUB tunnel. The compressor on the left supplies the air bushings; the centrifugal fan on the right drives the flow.

From this section onward the axis names *lift* and *drag* replace the cell labels CH0 and CH1 of Section 4.2, since the tunnel frame fixes which force each cell records. Six subsections build up the calibration: a zero-preload check (Section 4.3.1), two bidirectional load campaigns that anchor the slopes (Sections 4.3.2 and 4.3.3), a cross-talk fit (Section 4.3.4), a tunnel-angle calibration that recovers θ (Section 4.3.6), a short noise re-check (Section 4.3.7), and the combined uncertainty budget that closes the section (Section 4.3.8). The cross-phase comparison with the bench and the workshop is left to the discussion chapter.

4.3.1 Pre-calibration checks

The pre-calibration survey covers four items: rig levelling, turntable centring below the tunnel-floor cutout, supply-line state, and bridge zero-preload. Manifold pressure, cell-to-cable angles and ambient temperature carry over from Section 4.2.2; the new measurements are the per-rail inclinometer readings and the turntable gap (Table 4.11).

Rail levelling. A digital inclinometer is read along each of the four rails of the two bearing stages, at three positions per rail. The reported value is the mean over those positions, the operationally meaningful number for the moving carriage. The side-force stage reads dead level on both rails; the drag-axis stage carries a small bias on its right rail. The largest reading stays an order of magnitude below the threshold at which a residual gravity preload becomes comparable to the bridge noise, so no shimming is needed.

Turntable alignment. The turntable that carries the rig is positioned under the tunnel-floor cutout to a radial gap of ~ 5 mm around the full circumference. The air-bushing stages let the assembly translate freely once raised: the operator sets the turntable height, releases the bushings, slides the rig until four plumb-line markers hung from the tunnel-hole rim touch four reference points on the turntable rim, and then re-engages the cells.

Bridge zero-preload. Both bridge outputs are recorded for six seconds with the bare rig in the tunnel. Noise levels (Table 4.11) sit below the Phase I post-mitigation reference of 0.7 μV/V (Section 4.2.8) and roughly two orders of magnitude under the smallest load-induced signal change of the runs that follow (≈ 182 μV/V at one kilogram on drag, Section 4.3.3). The rig is in mechanical equilibrium and no thermal or pneumatic transient is masking the calibration signal.

Table 4.11: Pre-calibration survey before the Phase II bidirectional runs.

Group	Item	Value
Environment	Laboratory temperature	22 °C
	Manifold pressure (Section 4.2.2)	6.5 bar
Cell mounting	Cell-to-cable placement angle, both ends	$< 1^\circ$
	Cable two-axis angle, both ends	$< 1^\circ$
Rail levelling	Drag-axis stage, rail 1	0.05°
	Drag-axis stage, rail 2	0.10°
	Side-force stage, rail 1	0.00°
	Side-force stage, rail 2	0.00°
Turntable gap	Radial gap to tunnel-floor cutout	~ 5 mm
	(reference: BikeValley installation)	~ 50 mm
Bridge zero	Lift bridge mean (six-second window)	$+29.5$ μV/V
	Lift bridge noise, σ	0.5 μV/V
	Drag bridge mean	-114.4 μV/V
	Drag bridge noise, σ	0.6 μV/V

4.3.2 Bidirectional lift-axis calibration

The lift axis is calibrated bidirectionally with the FUTEK LSB201 cell loaded along its own axis through the same cable-and-pulley fixture used in Phase I. Compression and tension are recorded as separate runs of three load–unload cycles each, from 0 to 93.2 N. The two branches are reduced jointly with a bidirectional shared-intercept fit: the per-branch slopes are identified independently while a single voltage-ratio intercept is shared across the zero-crossing, which removes the discontinuity at $F = 0$ that an independent two-line fit would introduce (American Institute of Aeronautics and Astronautics, 2002). The polynomial cross-talk matrix of Section 4.3.4 and the unified θ of Section 4.3.6 are not yet folded in here: this subsection isolates the diagonal sensitivity of the lift cell.

Table 4.12: Lift-axis calibration metrics from the joint shared-intercept fit. Linearity is the maximum residual relative to $F_{S,\mathrm{rated}}$ on the ascending leg; hysteresis is the worst cycle-resolved value $|\Delta V_R|/V_R(F_{\max})$.

Branch	$\lvert S\rvert$ (V/V/N)	R^2	Lin. (%FS)	Hyst. (%FS)
Compression	1.84691×10^{-5}	0.99766	1.85	1.35
Tension	1.84813×10^{-5}	0.99788	1.64	1.85
			Shared intercept b (V/V)	-1.187×10^{-4}
			Bidirectional asymmetry $\lvert\Delta S\rvert/\langle\lvert S\rvert\rangle$	0.066 %

Compression and tension agree to 0.066 % in slope, well under the 0.18 % benchmark of Ostafichuk and Green (2002). The intercept fitted across both branches, -1.187×10^{-4} V/V, picks up the residual zero-load offset and stops the conversion jumping at $F = 0$. Linearity sits under 1.9 % FS on each branch. Worst-cycle hysteresis touches 1.9 % FS on the tension side, just inside the ±2 % FS envelope used everywhere else in this chapter.

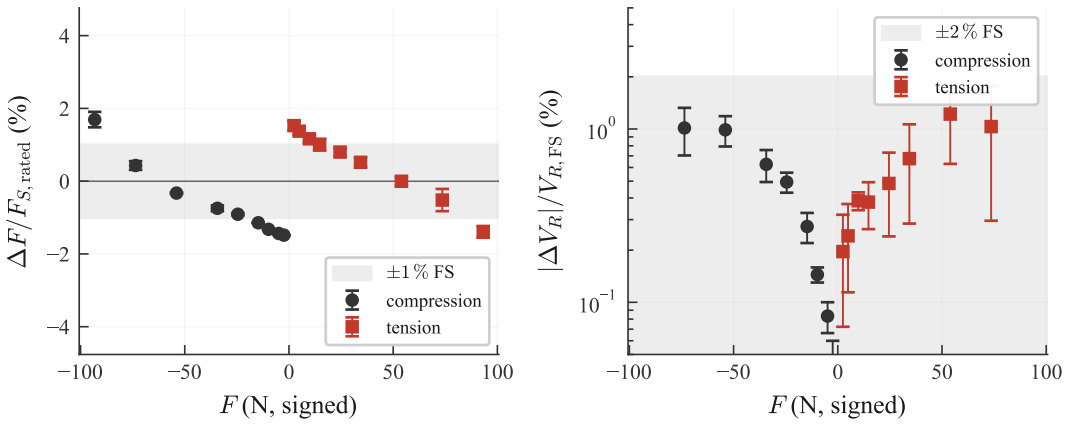

Figure 4.17: Per-force-level mean ± cycle σ of the ascending residual $\Delta F/F_{S,\mathrm{rated}}$ (left) and cycle-resolved hysteresis $|\Delta V_R|/V_R(F_{\max})$ (right, log axis). Compression grey, tension red. Shaded bands: ±1 % FS (left) and ±2 % (right).

4.3.3 Bidirectional drag-axis calibration

The drag axis is calibrated bidirectionally with the FUTEK LSB201 drag cell (Phase 0 bench slope $S_{D,\mathrm{bench}} = 1.8088 \times 10^{-5}$ V/V/N) loaded along its own axis through the cable-and-pulley fixture. Compression and tension are recorded as separate runs of three load–unload cycles each, from 0 to 93.2 N, with the same bidirectional shared-intercept formulation (American Institute of Aeronautics and Astronautics, 2002) §3.1.1 used on the lift axis (Section 4.3.2). The polynomial cross-talk matrix of Section 4.3.4 and the unified θ of Section 4.3.6 are not folded in here.

Table 4.13: Drag-axis calibration metrics from the joint shared-intercept fit. Bench agreement is the in-situ slope divided by the Phase 0 bench slope 1.8088×10^{-5} V/V/N; hysteresis is the worst-cycle $|\Delta V_R|/V_R(F_{\max})$.

Branch	$\lvert S\rvert$ (V/V/N)	R^2	Bench agr.	Lin. / Hyst. (%FS)
Compression	1.75617×10^{-5}	0.99895	97.09 %	1.36 / 1.49
Tension	1.86003×10^{-5}	0.99502	102.83 %	2.41 / 1.22
			Shared intercept b (V/V)	$+9.60 \times 10^{-6}$
			Bidirectional asymmetry $\lvert\Delta S\rvert/\langle\lvert S\rvert\rangle$	5.74 %

The drag cell shows a 5.74 % bidirectional asymmetry between the two slopes, with the bench-anchored Phase 0 slope sitting between them at ±2.9 percentage points. The lift cell on the same tunnel mount returned only 0.066 % (Section 4.3.2), so the asymmetry is a property of the drag cell-and-rig pair, not of the tunnel environment. The tension-branch linearity reaches 2.4 % FS at the highest plateau, just outside the ±1 % envelope and the dominant non-linearity on the drag axis; the polynomial cross-talk matrix of Section 4.3.4 selects the appropriate slope per sample on the sign of the measured force, and the residual contribution propagates into the budget of Section 4.3.8. Hysteresis on both axes stays inside the ±2 % FS envelope on every force level (Tables 4.12 and 4.13), so the clamp-fix of Section 4.2.9 holds in the tunnel installation without further intervention.

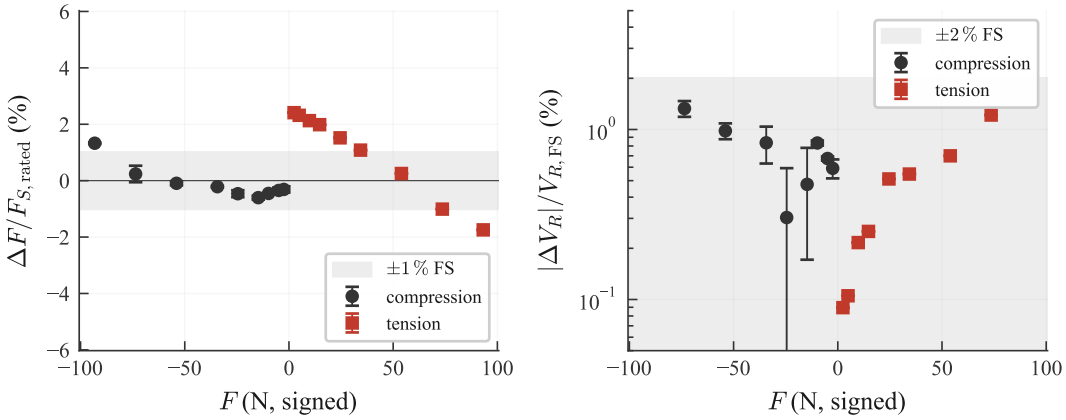

Figure 4.18: Per-force-level mean ± cycle σ of the ascending residual $\Delta F/F_{S,\mathrm{rated}}$ (left) and cycle-resolved hysteresis $|\Delta V_R|/V_R(F_{\max})$ (right, log axis). Compression grey, tension red. Shaded bands: ±1 % FS (left) and ±2 % (right).

4.3.4 Cross-talk: polynomial calibration matrix

The cross-talk between the two cells in the wind-tunnel state is fitted with the polynomial form introduced in Section 3.6:

$$F_{ij}^{\mathrm{bleed}}\left(F_j^{\mathrm{meas}}\right) \;=\; a_{ij}^{(\sigma_j)} \;+\; b_{ij}^{(\sigma_j)}\, F_j^{\mathrm{meas}} \;+\; c_{ij}^{(\sigma_j)}\left(F_j^{\mathrm{meas}}\right)^2, \tag{4.1}$$

one (a, b, c) triple per loading direction-pair. The runtime correction is the forward subtraction of Equation 3.2. Table 4.14 reports the twelve coefficients fitted from the in-tunnel bidirectional runs of Sections 4.3.2 and 4.3.3; Figure 4.19 plots the data and the fit per direction.

Table 4.14: Polynomial coefficients per direction-pair (AIAA R-091:2002 §3.1.1 form, intercept + linear + quadratic). Pooled residual over 180 plateaus: $u_{\mathrm{xt}} = 0.48$ N (propagated in Section 4.3.8).

Direction-pair	a (N)	b (%)	c (N^{-1})	RMS (N)
M_{01}, drag-tens → lift	+0.1512	−0.245	-1.5×10^{-6}	0.011
M_{01}, drag-comp → lift	−0.0064	+0.025	$+3.4 \times 10^{-6}$	0.003
M_{10}, lift-tens → drag	+1.2081	−1.045	$+3.7 \times 10^{-6}$	0.026
M_{10}, lift-comp → drag	+0.7273	−0.016	$+3.3 \times 10^{-4}$	0.870

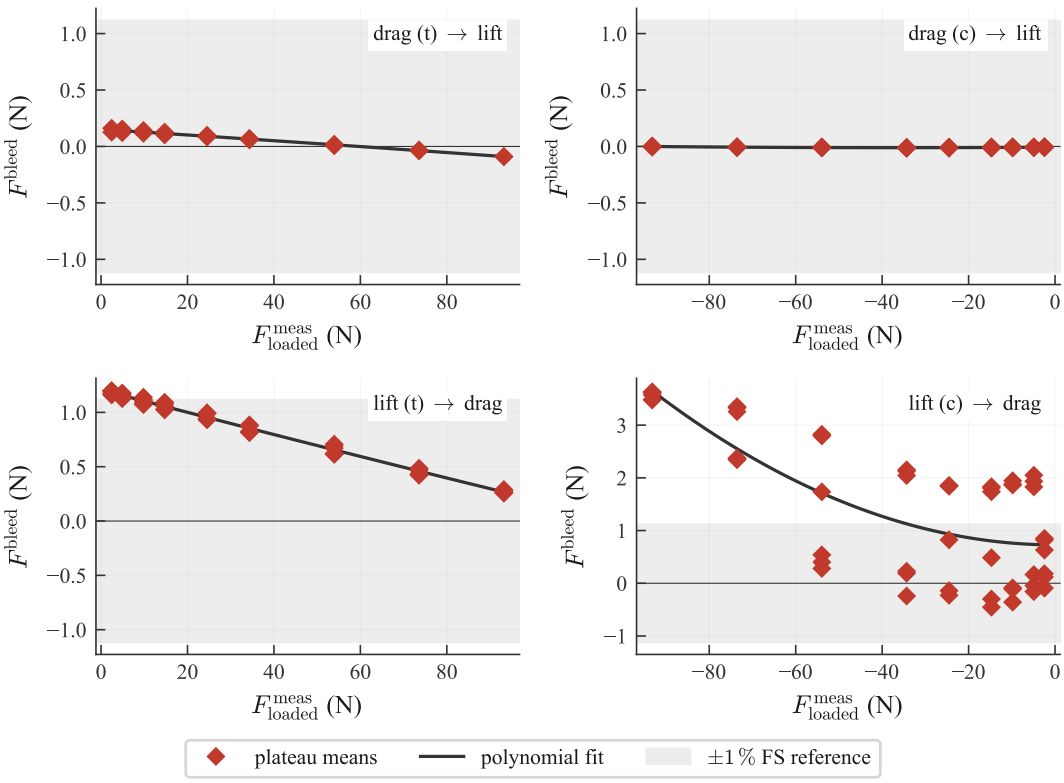

Figure 4.19: Off-axis bleed against loaded force for the four direction-pairs of Table 4.14. Abbreviations: (t) tension, (c) compression.

Discussion. Three couplings (M_{01} both polarities, M_{10} lift-tens) fit to within 0.03 N RMS. The fourth, lift-comp → drag, retains an 0.87 N residue that grows with the loaded lift force and carries the signature of a load-engaged contact depending on the simultaneous value of both axes. Resolving it cleanly would require a multi-axis simultaneous loading campaign outside the present scope; the residue is retained inside the pooled u_{xt} as a Type-B contribution in the budget of Section 4.3.8.

4.3.5 Lift-tension obstruction

The first lift-tension run failed the live linearity and hysteresis monitor: a 28 % slope deficit below the bench-validated sensitivity, with linearity at 9.94 % FS and hysteresis at 3.47 % FS. Inspection of the turntable revealed a foreign fragment lodged in the $\sim$ 5 mm rim gap that contacted the rotating disk only once the rig settled under sustained load (Figure 4.20, panel a). The fragment was removed and the run was repeated under the identical protocol; the corrective run (panel b) recovered the bench-validated slope of 1.79×10^{-5} V/V/N with $R^2 = 0.9998$, confirming that the load-dependent deviation in panel (a) was a one-off mechanical obstruction rather than a balance characteristic.

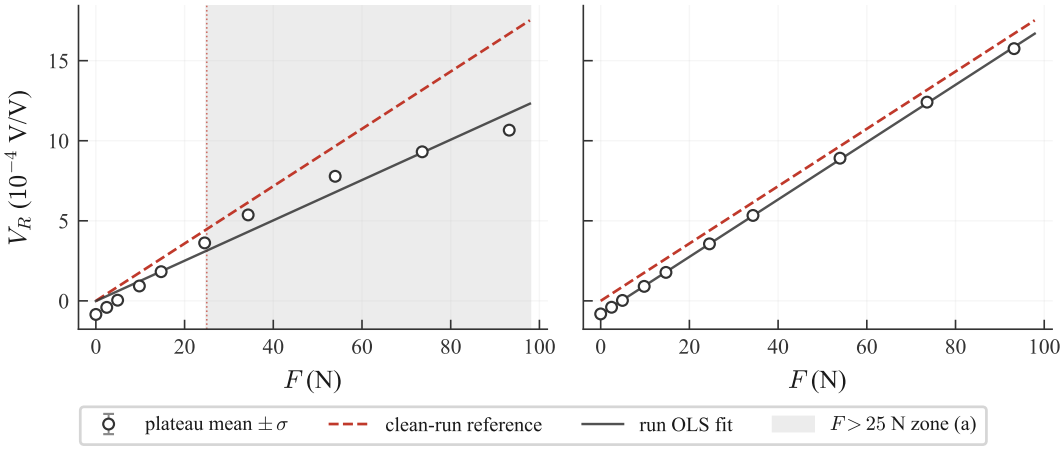

Figure 4.20: Plateau mean V_R vs. applied force F, with the clean-run slope as the dashed reference. (a) Initial run with a load-dependent deviation above $\sim$ 25 N. (b) After removing the turntable rim contact, plateaus collapse onto the reference.

4.3.6 Balance-to-tunnel rotation

The rotation θ between the balance principal axes and the tunnel frame is quantified by a dead-weight calibration: a cable routed over a low-friction pulley applies a known horizontal force F_{app} along the nominal drag axis at three loading masses (Figure 4.21). For each load, the calibrated force pair $(F_L^{\text{bal}}, F_D^{\text{bal}})$ is recorded in the balance frame; the rotation that projects the applied load purely onto the drag axis is

$$\theta_i \;=\; \arctan\!\left(\frac{F_L^{\text{bal}}}{F_D^{\text{bal}}}\right)_i , \tag{4.2}$$

and the calibrated value is the mean across the ascending load steps; the standard deviation propagates into the budget of Section 4.3.8. The calibrated rotation is $\theta = 2.64°$, applied at every plateau of the wind-tunnel polar of Section 4.4.

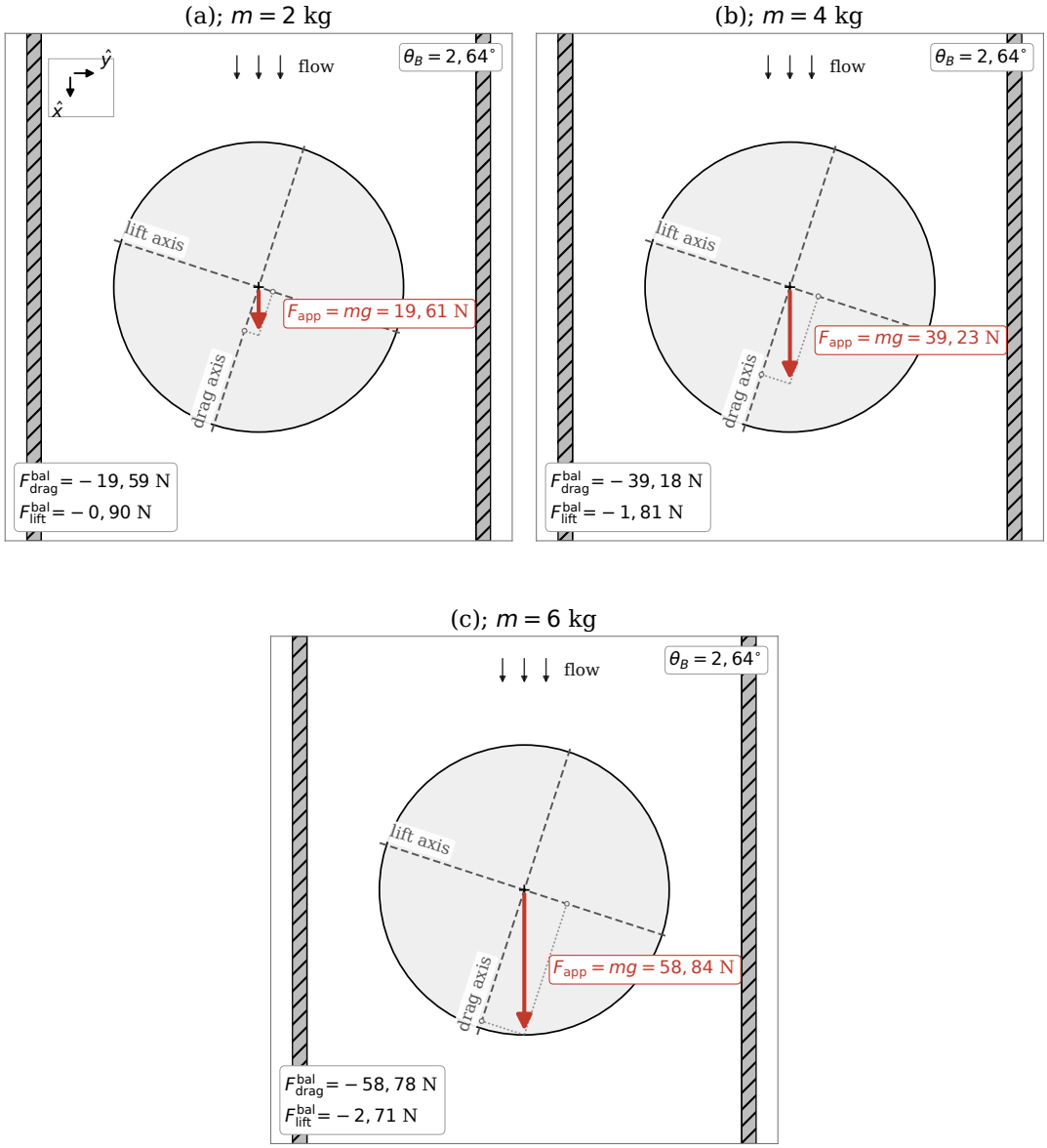

Figure 4.21: Top view at the three loading masses. $\mathbf{F}_{\text{app}}$ (red) acts along the tunnel drag direction; the balance axes (dashed) are rotated by $\theta = 2.64°$ (visually exaggerated). Projections give F_D^{bal}, F_L^{bal}.

4.3.7 Noise-floor spectral check

The thirty-minute creep-hold doubles as a noise-floor check on each channel. Two passes are run on the same data. A rolling root-mean-square in time isolates the compressor on/off cycles; a Welch PSD, computed separately on the on- and off-windows that detector returns, then exposes which mechanical modes ride the on-cycle and which sit underneath as background. The point is to confirm that the channel's noise floor sits well below the smallest load signal the rig is asked to resolve.

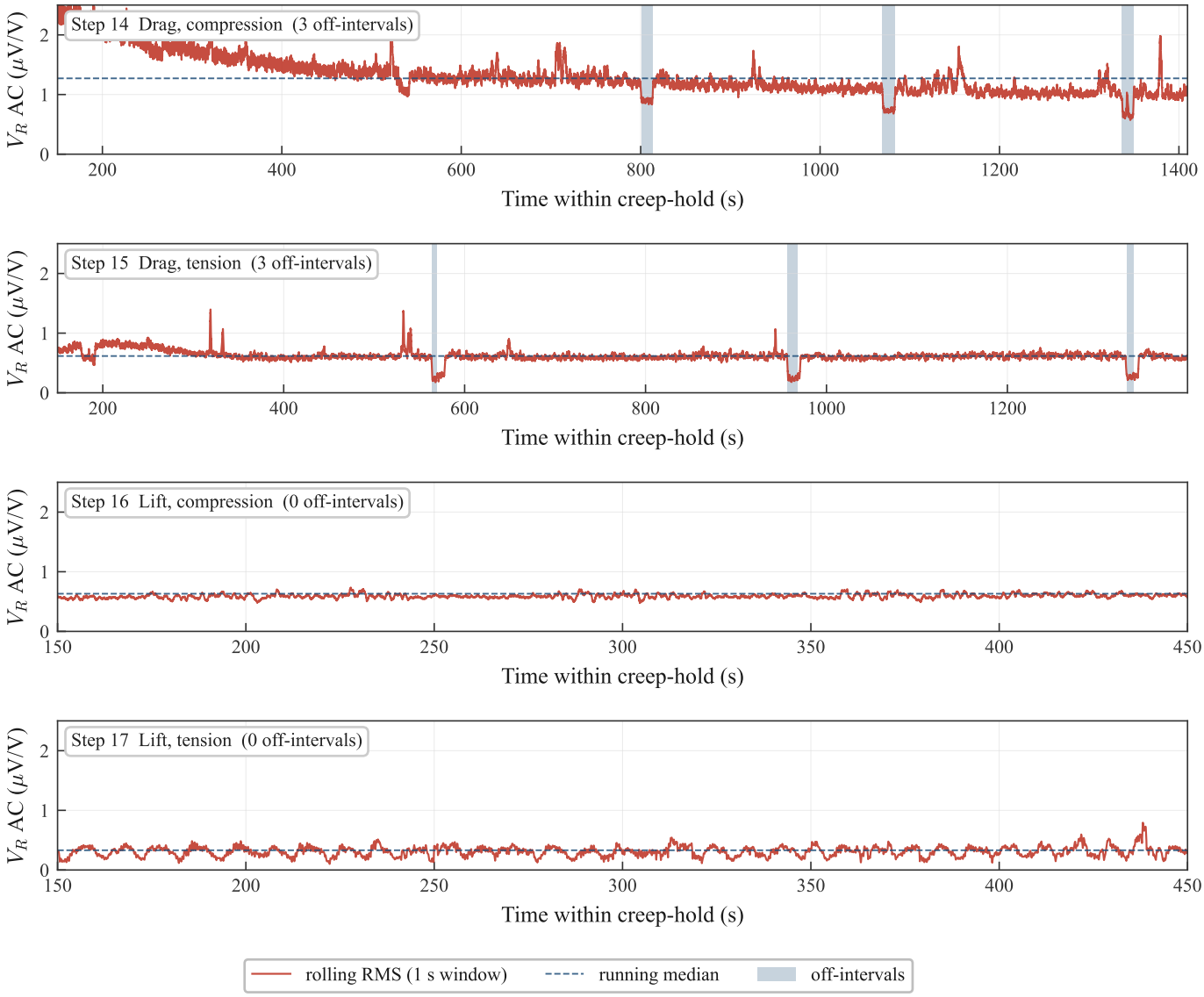

Figure 4.22: Rolling-RMS of the AC voltage-ratio component on the thirty-minute creep-hold of each Phase II run (one-second window). Dashed line: running median; shaded bands: detector-flagged compressor-off intervals.

On the drag-channel runs a three-criterion detector (relative drop below 0.75× the running median, absolute drop above 0.30 μV/V, sustained for at least 4 s) resolves three off-intervals on each of Steps 14 and 15. These intervals partition the AC residue into compressor-on and compressor-off subsets, on which a separate Welch PSD is computed (Figure 4.23). At 24 Hz the on-window peak exceeds the off-window peak by a factor of 35.2 on Step 14 and 21.7 on Step 15, as expected from a stationary mechanical source coupled into the rig. Lift-channel runs

return no off-intervals, either because the channel is less sensitive to the coupling or because the compressor did not cycle during those two windows.

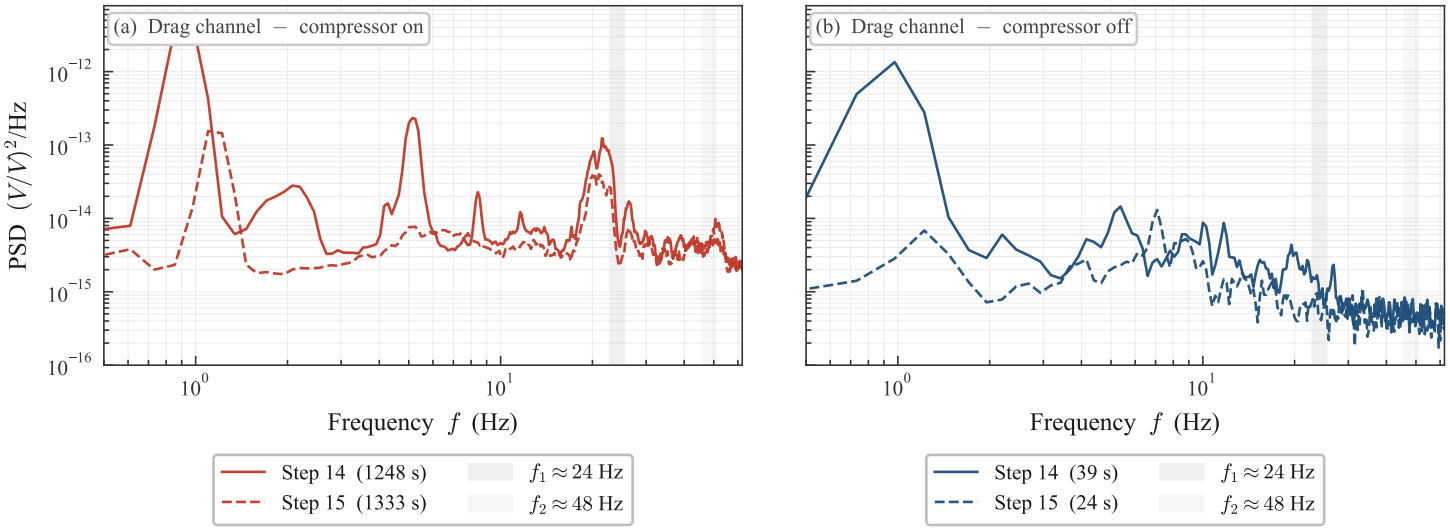

Figure 4.23: Drag-channel Welch PSD on the creep-hold. **(a)** compressor-on, **(b)** compressor-off. Step 14 solid, Step 15 dashed.

The dominant spectral feature in both drag runs is not the compressor band but a structural peak near 1 Hz, present in the on and off subsets at comparable magnitude. Its location coincides with the pendulum natural frequency of the dead-weight on the cable–pulley loop, $f \approx (1/2\pi)\sqrt{g/L}$, which for $L \approx 0.25$ m yields $f \approx 1.0$ Hz. Step 14 (drag compression) carries about 29× more PSD in the 0.85–1.22 Hz pendulum band than Step 15 (drag tension) and a factor of 3.6 more in the 22–26 Hz compressor fundamental, evidence of a different load-transfer geometry through the cable–pulley path.

Table 4.15: Per-run noise summary on the thirty-minute creep-hold of each calibration run.

Step	Run	Median (μV/V)	Off intervals	On/off PSD ratio @ 24 Hz
14	Drag, compression	1.27	3	35.2×
15	Drag, tension	0.62	3	21.7×
16	Lift, compression	0.63	0	-
17	Lift, tension	0.33	0	-

Across all four runs the worst median rolling-RMS is 1.27 μV/V on Step 14. That value already wraps in every noise-floor source, the structural 1 Hz mode included. From the bidirectional drag slope of Section 4.3.3, $s_{\mathrm{drag,t}} = 1.86 \times 10^{-5}$ (V/V)/N, one kilogram of applied load produces $\Delta V_R = s \cdot g \approx 182$ μV/V. The total broadband noise therefore sits a factor of about 140 below that smallest load signal and is absorbed by the residual-scatter term of Section 4.3.8 (0.73 % FS) without a separate line item.

4.3.8 Force-domain uncertainty budget

The per-axis force uncertainty at the Phase II calibration state combines three Type-B sources (cell-intrinsic residue, cross-talk residual, tare drift) and a Type-A cycle term carried at the coefficient stage; DAQ noise on the 30 s dwell mean (< 3 mN, variance share $< 10^{-6}$) is dropped after a one-line check. The cross-talk residual is the pooled RMS of the polynomial-fit residuals of Section 4.3.4. The cell-intrinsic residue is force-dependent, fit as $u_{\text{cell}}(F) = \sqrt{a^2 + (bF)^2}$ on the in-situ residuals per axis (Sor et al., 2019; Santamaría et al., 2024). Standard propagation for uncorrelated inputs at unit sensitivity gives

$$u_c^2(F) \;=\; u_{\text{cell}}^2(F) + u_{\text{xt}}^2 + u_{\text{tare}}^2, \qquad U(F) = 2\,u_c(F), \tag{4.3}$$

with coverage factor $k = 2$ for an approximately 95 % interval (Joint Committee for Guides in Metrology, 2008).

Table 4.16: Per-axis contributors and combined envelope at $F = 18$ N (operational) and $F_{\text{rated}} = 111.21$ N (full scale). $u_{\text{cyc}}(V)$ is propagated in the coefficient budget of Section 4.4.5.

Source	Symbol	Type	$u(F_L)$ (N)	$u(F_D)$ (N)
Cell-intrinsic, $\sqrt{a^2 + (bF)^2}$	$u_{\text{cell}}(F)$	B	a=0.335, b=1.77 %	a=0.456, b=1.15 %
Cross-talk residual, pooled	u_{xt}	B	0.477	0.477
Tare drift, preflight to park	u_{tare}	B	0.30	0.30
Cycle-to-cycle, per V	$u_{\text{cyc}}(V)$	A	0.07–0.80	0.02–0.34
At $F = 18$ N:				
$u_{\text{cell}}(18)$			0.46	0.50
Combined standard u_c			0.73	0.75
Expanded U at $k = 2$			**±1.46**	**±1.51**
At $F_{rated} = 111.21$ N:				
$u_{\text{cell}}(F_{\text{rated}})$			2.00	1.36
Combined standard u_c			2.08	1.47
Expanded U at $k = 2$			**±4.16**	**±2.94**

The single residual that the polynomial matrix could not absorb is the lift-compression → drag standalone term of 0.87 N in Table 4.14, a load-engaged deflection that would require a multi-axis simultaneous loading campaign to resolve; it is carried inside the pooled u_{xt} and recorded as a known limitation. These per-axis envelopes feed the coefficient-domain budget of Section 4.4.5 as the L and D rows of Table 4.23, with the per-V cycle term added there.

4.4 NACA 0012 airfoil validation

The first validation case applies the calibrated balance of Section 4.3 to a NACA 0012 wing mounted vertically on the turntable of the VUB subsonic tunnel test section (Figure 4.24). The model is a full-aluminium structural section recovered from an actual aircraft wing rather than a scale model, with chord $c = 0.60$ m and a physical span of 1.00 m equal to the tunnel height; with the 58 mm tip-to-ceiling gap subtracted the aerodynamically effective span is $b = 0.942$ m, giving aspect ratio $\mathrm{AR} = b/c = 1.57$ and reference area $S = c \cdot b = 0.565$ m^2. The rig is pre-checked before each session per the operational protocol described in Chapter 3.

Figure 4.24: NACA 0012 wing mounted vertically on the turntable inside the VUB subsonic tunnel test section.

The NACA 0012 is the headline validation case of this thesis because it carries the largest body of independent reference data at the present Reynolds range, and the specific wing used here is the same model that supports the aerodynamics laboratory sessions of the third-year bachelor course at VUB. The campaign sweeps the angle of attack from $-16°$ to $+16°$ in three ascending–descending cycles at four freestream velocities, $V = 9$, 12, 15 and 18 m/s ($\mathrm{Re}_c = 3.6$ to 7.2×10^5). The Phase II calibration pipeline of Section 4.3 is applied to every raw measurement of the campaign, and the subsections that follow benchmark the resulting polar against the established literature envelope one layer at a time.

4.4.1 Angle-of-attack reference

The angle of attack reported by the pipeline is inferred from the extension X of the linear actuator that drives the turntable (Figure 4.25). The relation $\alpha(X)$ is calibrated empirically once and held fixed for the campaign.

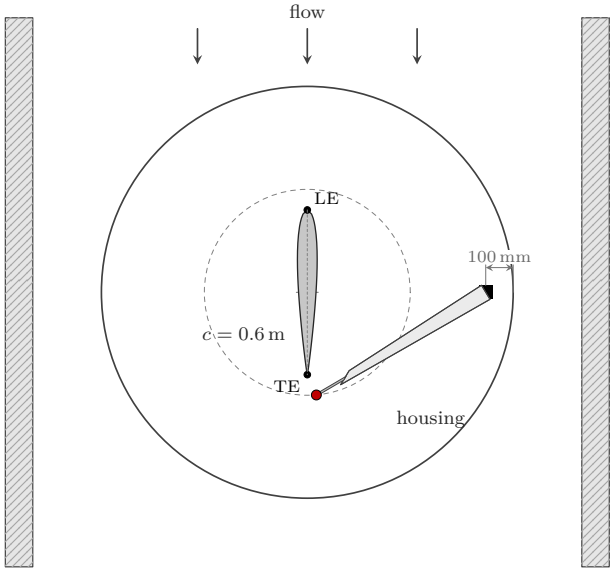

Figure 4.25: Top view of the AoA actuation chain at the visual zero-AoA reference ($X_0 = 123.4$ mm). Tunnel section width 2.0 m, turntable diameter 1.5 m, wing chord 0.6 m; the rod-end attachment (red) sits at radius 0.375 m on the turntable. The wing is mounted with its chord along a turntable diameter, approximately centred on the turntable, so the angle of attack is the rotation of this chord line about the turntable axis.

The wing is first driven to a visual $\alpha = 0°$ and the corresponding actuator extension is locked as the zero-AoA anchor at $X_0 = 123.4$ mm. The actuator is then stepped through fourteen extensions across the working stroke, and the absolute turntable angle at each station is read off a custom-made MDF rotary protractor sized to the turntable. A degree-two polynomial fitted to the fourteen $(X, \alpha_{\text{meas}})$ pairs gives

$$\alpha(X) \;=\; 0.192 \;+\; 0.1511\,X \;+\; 9.43\times10^{-5}\,X^2 \qquad (\alpha \text{ in deg, } X \text{ in mm}); \tag{4.4}$$

the angle then enters every downstream polar as the offset form $\alpha_{\text{op}}(X) = \alpha(X) - \alpha(X_0)$.

Table 4.17: Calibration quality of the empirical $\alpha(X)$ polynomial.

Metric	Value
Calibration points	14
Operational α range	$-20°$ to $+26°$
Coefficient of determination	$R^2 = 0.99991$
RMS residue	$0.133°$
Zero-AoA anchor	$X_0 = 123.4$ mm

The protractor is read to $\pm1°$ per point, and repeat checks across the measurement campaign confirmed only marginal play in the actuation chain. The $0.133°$ RMS residual and the per-point read uncertainty together set the AoA contribution to the α-budget of Section 4.4.5.

4.4.2 Mechanical baseline

A wind-off reference sweep is recorded each measurement morning: the model is driven through the polar α-grid at $V = 0$, held 30 s per plateau, with the air bushings at the same 6.5 bar. The calm-window mean per plateau gives the per-α tare. The drag baseline shows a reproducible monotone α-trend with a peak-to-peak range of ~ 0.3 N across the operational α-window; the lift baseline is an order of magnitude flatter and exhibits no resolved α-trend (Figure 4.26).

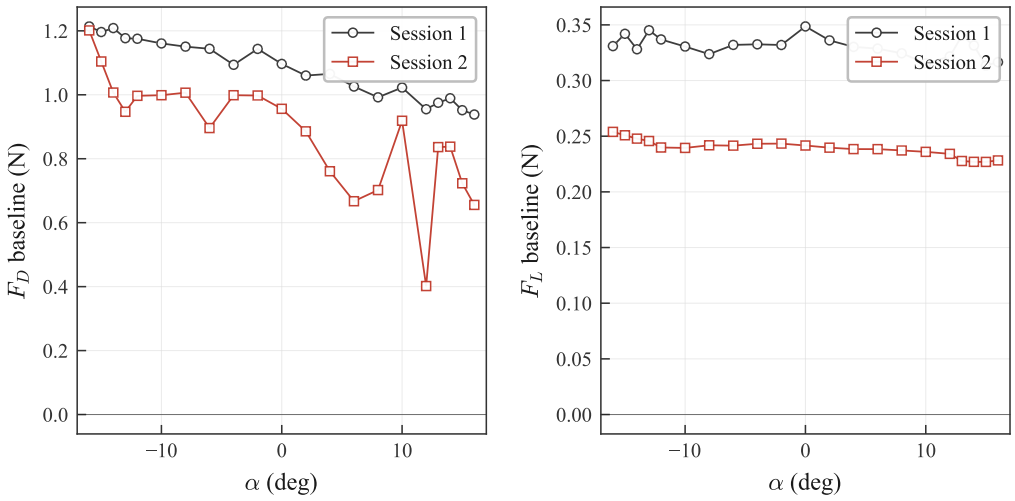

Figure 4.26: Wind-off baseline at $V = 0$ across the polar α-grid. The Session 2 value at $\alpha = -15°$ is linearly interpolated from neighbouring plateaus to suppress a one-off servo-overshoot artefact at this point; the per-α tare applied in the pipeline retains the raw value.

Per-α subtraction is applied to the drag channel only: the drag baseline contains the wing-mount preload on the load cells that has to be removed before C_D can be compared against the airfoil-only literature reference. The lift channel is left at its calibration intercept of Section 4.3.2; subtracting a per-α lift baseline would force $|C_L(\alpha = 0)|$ to zero by construction and remove the internal-consistency check of Section 4.4.3. Two morning sessions span the four polars, with the per-session drag tare at $\alpha = 0$ and its extremes listed in Table 4.18; cross-validation against the in-run wind-off segment at the start of each polar is reported in Section 4.4.4.

Table 4.18: Drag tare per session, applied to both polars run on the same day (V = 9 and 15 on 3 May; V = 12 and 18 on 4 May). Balance frame, $F_{D,\mathrm{tare}}^{\mathrm{min\,/\,max}}$ are the extremes across the α-sweep.

V [m/s]	$F_{D,\mathrm{tare}}(\alpha = 0)$ [N]	$F_{D,\mathrm{tare}}^{\mathrm{min}}$ [N]	$F_{D,\mathrm{tare}}^{\mathrm{max}}$ [N]
9	+1.097	+0.938	+1.214
12	+0.956	+0.402	+1.579
15	+1.097	+0.938	+1.214
18	+0.956	+0.402	+1.579

4.4.3 Polars

The campaign sweeps the angle of attack from -16 to $+16°$ at four freestream velocities, $V = 9$, 12, 15 and 18 m/s (Re_c between 3.6×10^5 and 7.2×10^5), in three ascending–descending cycles so each α value is sampled on six plateaus. On each plateau the bidirectional Phase II calibration of Section 4.3 converts the load-cell voltages into lift and drag, and the per-α drag tare of Section 4.4.2 subtracts the wing-mount preload before C_L and C_D are formed. Figure 4.27 shows one full cycle at $V = 12$ m/s: the stall regions stand out as vibration bands on both bridge channels, separated by stable plateaus that sit between the linear-actuator step transients. The next section turns these settled plateaus into $C_L(\alpha)$ and $C_D(\alpha)$.

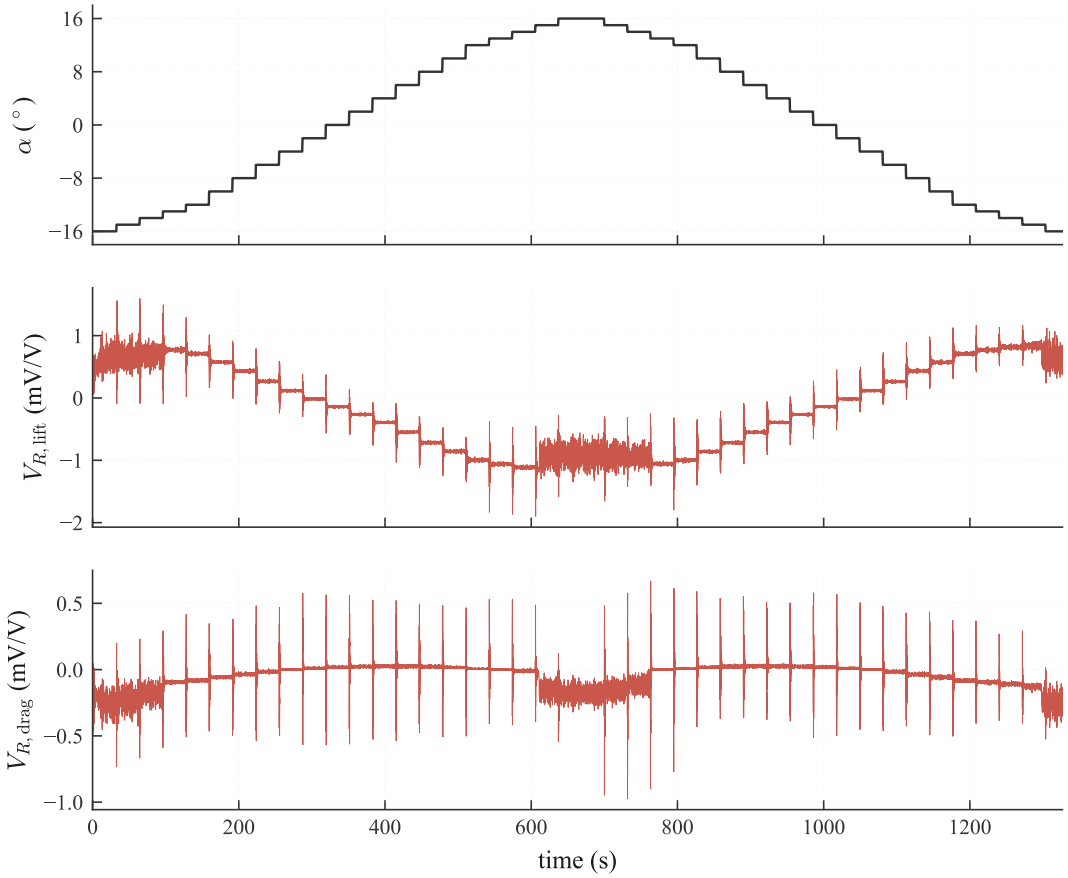

Figure 4.27: One full sweep cycle of the raw acquisition at $V = 12$ m/s. *Top:* commanded angle of attack. *Middle and bottom:* raw bridge voltage ratios V_R of the lift- and drag-channel load cells, before the Phase II calibration converts them into force.

Averaging the settled plateaus per cycle and dividing by qS gives one $C_L(\alpha)$ and one $C_D(\alpha)$ curve per velocity. Figures 4.28 and 4.29 show the four pairs, plotted here without any wall-interference correction. Section 4.4.3 runs its model-independent consistency checks on these raw curves; the wall corrections are introduced where the measurement is brought onto the free-air literature reference (Sections 4.4.6 and 4.4.6) and quantified in the budget of Section 4.4.5.

Each α setting is visited six times per session (three ascending + three descending sweeps); the marker is the mean and the shaded band the standard deviation across those six plateaus, i.e. session-internal scatter only; systematic contributions from calibration, tare, q, S and α are added in the GUM budget of Section 4.4.5. On both channels the polar passes smoothly through $\alpha = 0$ with no visible step at the bidirectional zero-crossing of Section 4.3.3: the cross-talk push from the lift channel and the per-α tare residue produce a continuous C_D curve across

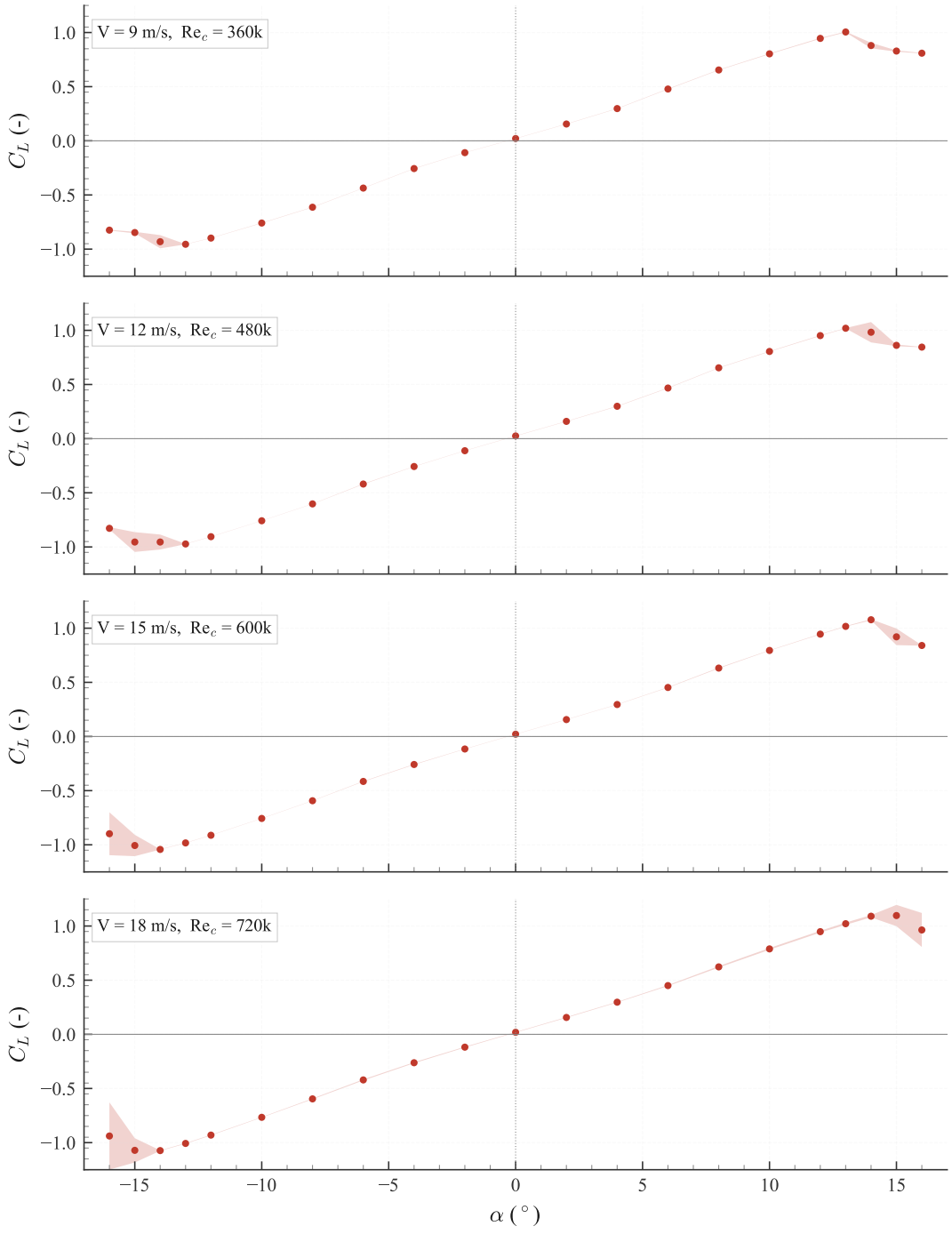

Figure 4.28: Reduced $C_L(\alpha)$ at $V = 9$, 12, 15 and 18 m/s. Markers are the per-α mean over the six plateaus (three cycles × two sweep directions); the shaded band is the $\pm 1\sigma$ plateau spread.

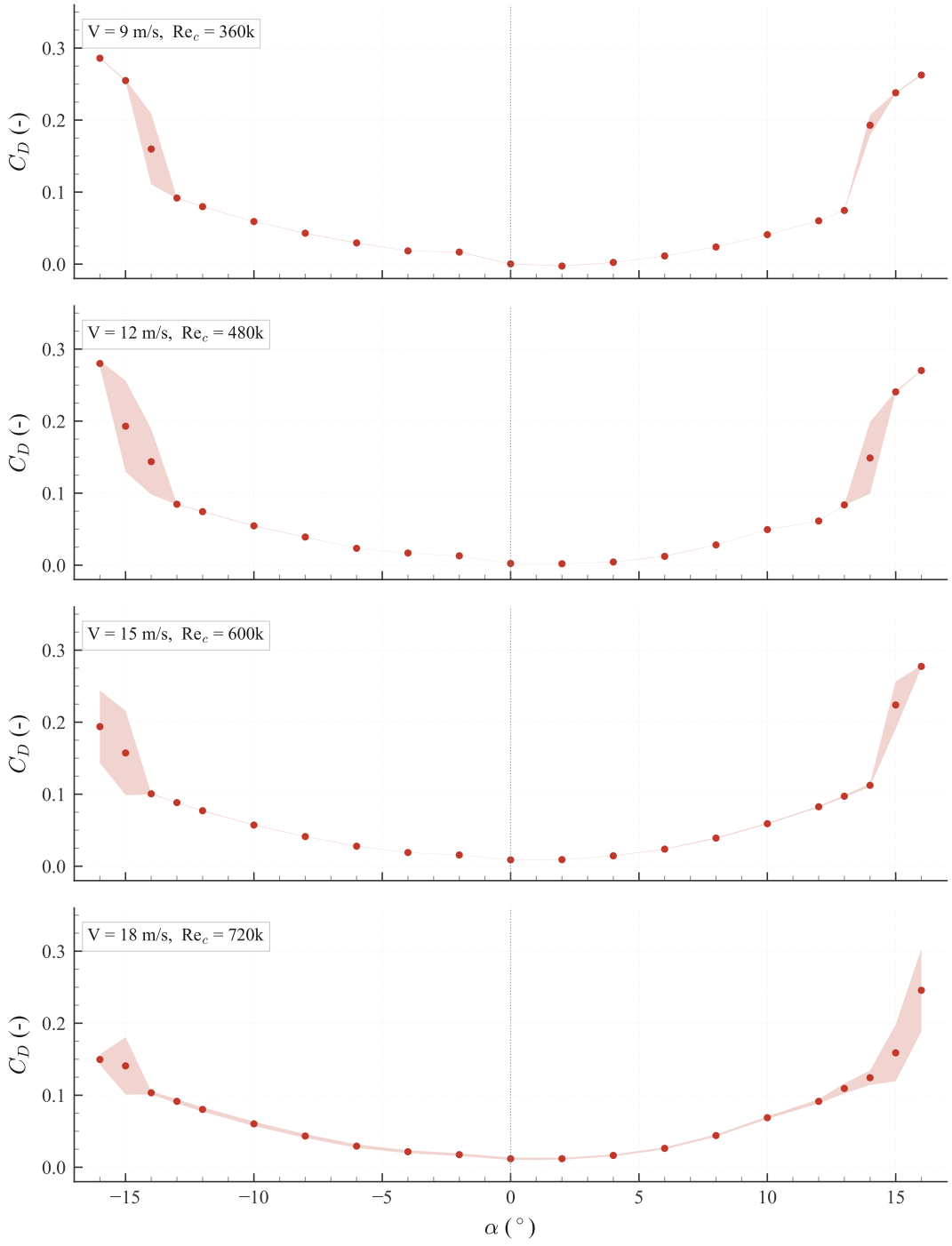

Figure 4.29: Reduced $C_D(\alpha)$ at $V = 9$, 12, 15 and 18 m/s. Markers are the per-α mean over the six plateaus (three cycles × two sweep directions); the shaded band is the $\pm 1\sigma$ plateau spread.

$\alpha = 0$ as the direct visual confirmation. Before the second-session repeatability of Section 4.4.4, the coefficient-domain uncertainty budget of Section 4.4.5 and the literature comparisons of Sections 4.4.6–4.4.6, three model-independent geometric checks of the symmetric NACA 0012 profile are applied to the polar across the four campaign velocities together: the zero references of the lift and drag floors, the mirror behaviour across $\alpha = 0$, and the linearity of the lift curve in the attached-flow region.

Lift-zero residual and minimum-drag floor. A symmetric profile must return $C_L(\alpha = 0) = 0$. The measurement leaves $|C_L(0)|$ between 0.019 and 0.025, staying close to 0.02 at every velocity (Figure 4.30, left). A fixed balance-side bias would scale as $1/qS$ and vary by a factor four between $V = 9$ and $V = 18$, which the residue does not; it is therefore an angle-reference offset, not a force bias. Quantitatively,

$$\delta\alpha \;=\; \frac{|C_L(\alpha = 0)|}{\mathrm{d}C_L/\mathrm{d}\alpha}, \tag{4.5}$$

gives $0.27°/0.33°/0.28°/0.26°$ at $V = 9/12/15/18$ m/s ($\bar{\delta\alpha} = 0.29° \pm 0.03°$), well inside the $\pm 1°$ visual-alignment uncertainty of the installation protractor and captured by the conservative $u(\alpha) = \pm 0.2°$ carried into Section 4.4.5. Drag floors run from a small negative residual at $V = 9$ m/s ($C_{D,\min} = -0.003$) up to $+0.012$ at $V = 18$ m/s (Figure 4.30, right). The negative value at the lowest velocity is not aerodynamic. It traces to the constant intercept of the lift-into-drag polynomial (Table 4.14), a residual zero-offset not fully removed by the per-α tare. As a fixed force it divides by qS into a $1/qS$ coefficient offset, largest at the smallest dynamic pressure, where it dominates the sub-newton aerodynamic drag and tips the minimum a few thousandths below zero. Setting that constant term to zero lifts every $C_{D,\min}$ to between $+0.012$ and $+0.016$, a velocity-consistent floor that confirms the offset as the controlling term; the term is retained as part of the calibrated matrix, with its clean separation from genuine coupling left to the combined-load campaign of Chapter 7. The residual stays well inside the per-velocity $\pm U(C_D)$ band, which falls beneath the McCroskey scatter envelope at $V = 9$ and 12 m/s.

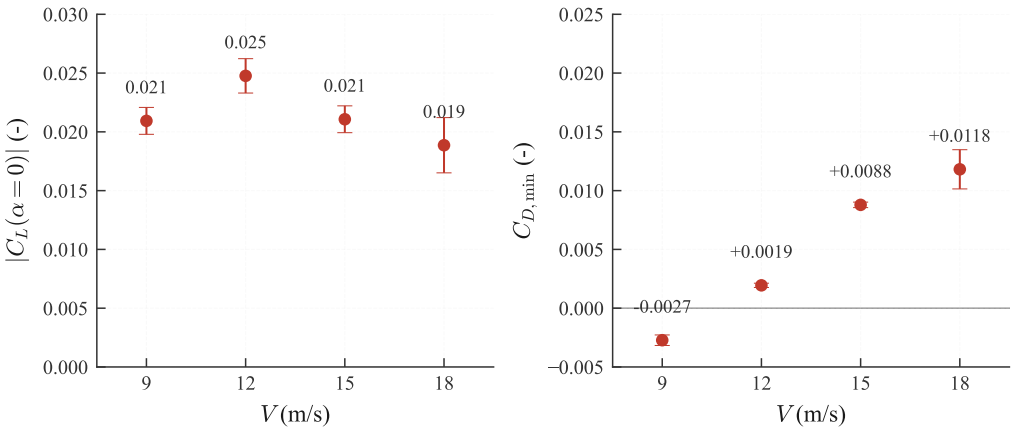

Figure 4.30: $|C_L(\alpha = 0)|$ (left) and $C_{D,\min}$ (right) at the four campaign velocities; error bars are the within-session σ across the six plateaus per α setting.

Mirror symmetry across the geometric zero. A geometrically symmetric profile mirrors its own polar around $\alpha = 0$: the lift branch is odd, the drag branch is even, and the two stall onsets sit at the same magnitude of angle. The three identities read

$$C_L(+\alpha) = -\,C_L(-\alpha), \tag{4.6}$$

$$C_D(+\alpha) = +\,C_D(-\alpha), \tag{4.7}$$

$$\left|\alpha^{+}_{\text{stall}}\right| = \left|\alpha^{-}_{\text{stall}}\right|, \qquad |\alpha| \le \alpha_{\text{stall}}. \tag{4.8}$$

The first two are evaluated on the folded $|\alpha|$ grid as the RMS deviation of the paired branches for C_L and C_D; the third compares the absolute angle at which $|C_L|$ peaks on each branch. Residuals per velocity are reported in Table 4.19 and visualised in Figure 4.31.

Lift-antisymmetry RMS sits between 0.024 and 0.050 with no monotonic V-trend; its magnitude is fully accounted for by the same $\delta\alpha \approx 0.25°$ visual-to-aerodynamic offset of Equation (4.5). Drag-symmetry RMS lies between 0.023 and 0.056 and concentrates at high $|\alpha|$ where the bucket rises steeply: a sub-degree α shift becomes visible once $\mathrm{d}C_D/\mathrm{d}\alpha$ exceeds $0.05/°$ post-bucket, while symmetry near the floor stays tight. Stall edges sit within one 1° AoA-grid step of each other at every velocity.

Table 4.19: Numerical results of the three mirror-symmetry checks. RMS lift antisym and RMS drag sym are the dimensionless residues of Equation (4.6); the stall-edge columns list the AoA-grid angles at which $|C_L|$ peaks.

V (m/s)	RMS lift antisym	RMS drag sym	$+\alpha_s$	$-\alpha_s$
9	0.042	0.023	+13°	−13°
12	0.050	0.033	+13°	−13°
15	0.048	0.056	+14°	−14°
18	0.024	0.056	+15°	−14°

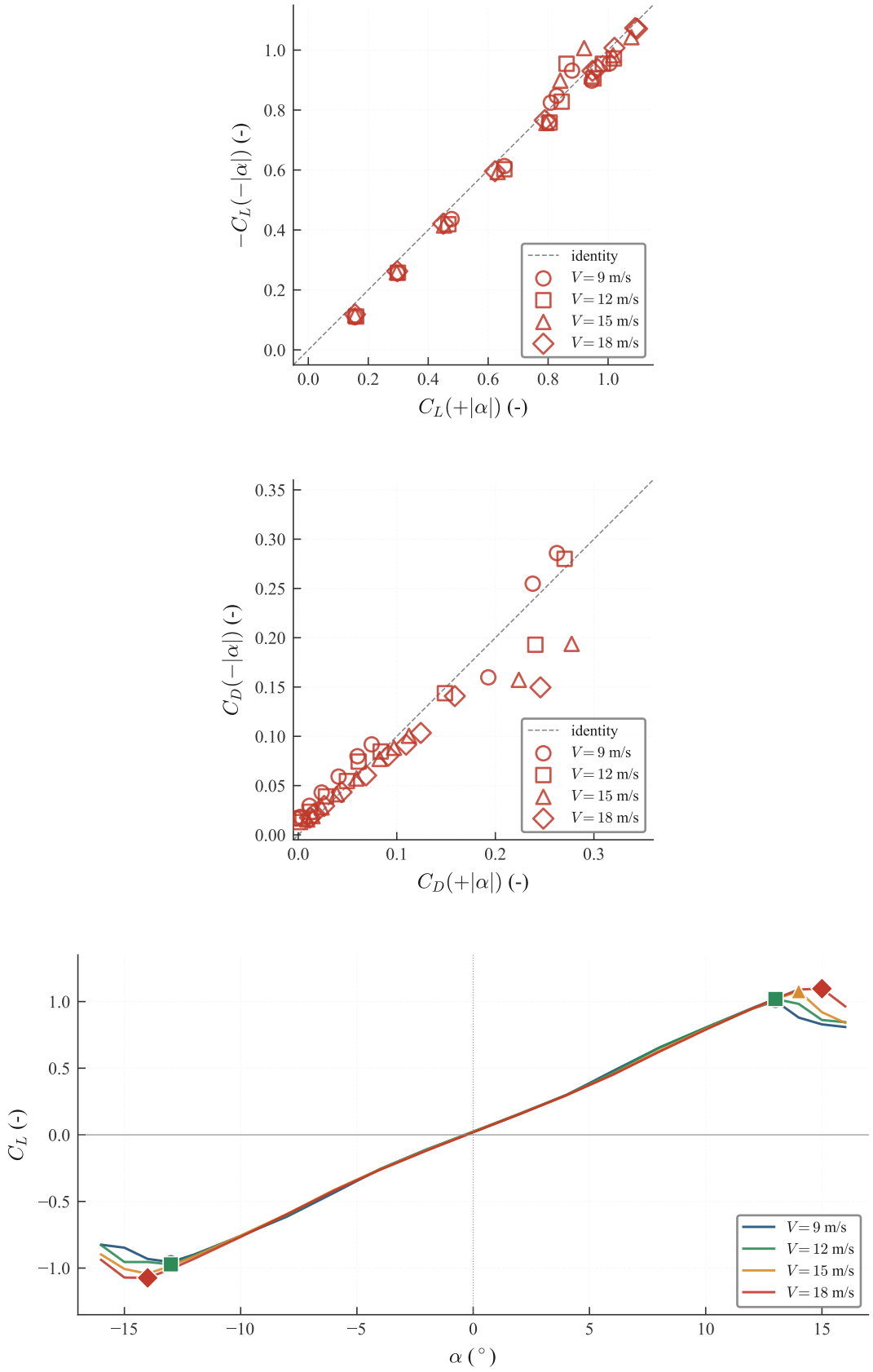

Figure 4.31: Three checks of Equation (4.6). *Top:* $-C_L(-|\alpha|)$ vs $C_L(+|\alpha|)$. *Middle:* $C_D(-|\alpha|)$ vs $C_D(+|\alpha|)$. *Bottom:* full polar with stall edges per branch. Markers: ◯ = V_9, □ = V_{12}, △ = V_{15}, ◊ = V_{18} m/s; dashed = identity. The bottom panel is additionally coloured by velocity.

Linearity and slope of the lift curve. On the attached-flow range $|\alpha| \le 8^\circ$ the lift curve is straight, and its slope must lie between two physical limits set by the geometry alone:

$$\underbrace{\frac{a_0 \cdot \mathrm{AR}_{\mathrm{eff}}}{\mathrm{AR}_{\mathrm{eff}} + 2} = 0.0670/^\circ}_{\text{Prandtl elliptic lower bound}} \;\le\; \frac{\mathrm{d}C_L}{\mathrm{d}\alpha} \;\le\; \underbrace{a_0 = 2\pi/\mathrm{rad} = 0.1097/^\circ}_{\text{thin-airfoil upper bound}}, \tag{4.9}$$

with $\mathrm{AR}_{\mathrm{eff}} = 2 \cdot \mathrm{AR}_{\mathrm{geom}} = 3.14$ for the wall-mounted semi-span. The upper bound is the inviscid thin-airfoil value $a_0 = 2\pi$ per radian at infinite aspect ratio, which follows from the Kutta–Joukowski theorem together with the Kutta condition (Anderson, 2017); the lower bound is the Prandtl elliptic lifting-line rescaling of that result to the present finite aspect ratio in the linear form after Tank et al. (2017).

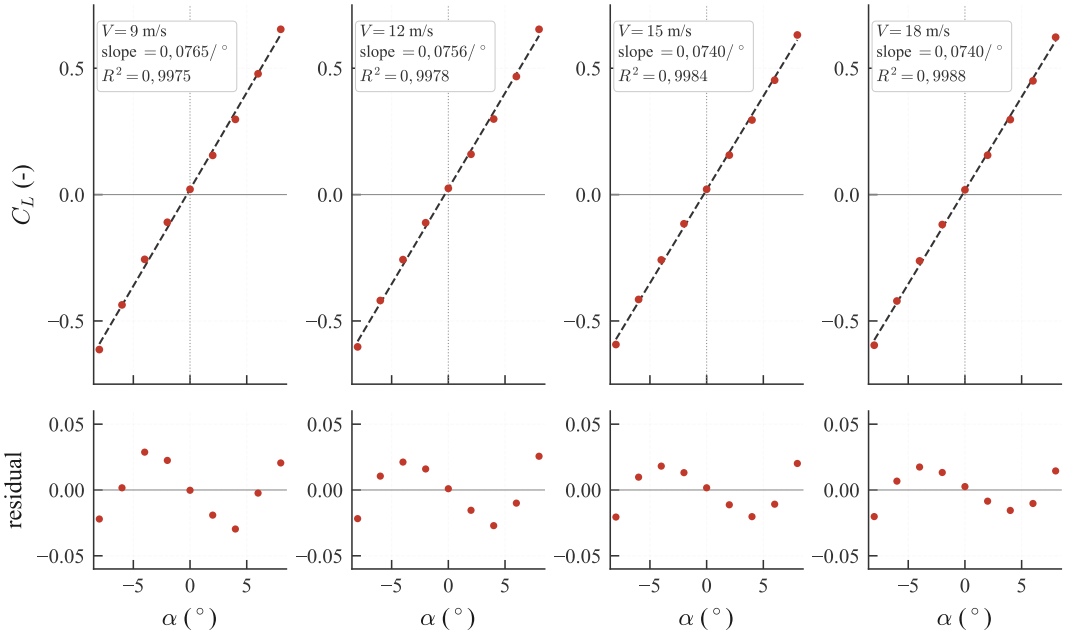

Figure 4.32: Linear region of the lift curve at the four campaign velocities. *Top:* $C_L(\alpha)$ with linear fit (dashed) and per-velocity slope and R^2. *Bottom:* fit residuals.

The measured slopes lie inside the window at every velocity, between 0.0740 and 0.0766/° (Table 4.20), all four comfortably above the Prandtl elliptic lower bound and well below the thin-airfoil ceiling. The fit returns $R^2 \ge 0.998$ at every velocity, with no operating point falling below the others.

Table 4.20: Linear-fit slope and coefficient of determination on $|\alpha| \le 8^\circ$. The slope window follows from Equation (4.9); the R^2 column is a quantitative descriptor of linearity rather than an acceptance threshold.

V (m/s)	$\mathrm{d}C_L/\mathrm{d}\alpha$ (/°)	R^2
9	0.0766	0.9975
12	0.0756	0.9978
15	0.0740	0.9984
18	0.0740	0.9988

A slight downward drift in slope with Reynolds number is visible across the table, from 0.0766/° at $V = 9$ m/s to 0.0740/° at $V = 18$ m/s. The drift is of the order of the per-fit standard error and stays inside the window at every velocity; the absolute comparison against the Prandtl elliptic prediction at each Reynolds number is the subject of Section 4.4.6.

Summary. Table 4.21 collects the seven quantities monitored in this subsection. The polar data set passes each model-independent geometric check on the following points:

- Zero-lift residue stays close to 0.02 at all four velocities, with no $1/qS$ scaling; the implied angle offset $\delta\alpha = |C_L(0)|/(dC_L/d\alpha)$ sits in $[0.26°; 0.33°]$ across the full envelope, i.e. V-independent within $\pm 0.04°$. A force-domain bias would scale as $1/V^2$ and produce a factor-four spread; the measured factor-of-1.3 spread is a hard falsification of any force-bias hypothesis and confirms a pure geometric AoA-installation offset, conservatively captured by $u(\alpha) = \pm 0.2°$ in Section 4.4.5.
- Drag floor runs from a small negative residual at $V = 9$ ($C_{D,\min} = -0.003$, the constant cross-talk intercept dominating the sub-newton drag at the smallest qS, not aerodynamic) up to $+0.012$ at $V = 18$; below the McCroskey scatter envelope at $V = 9$ and 12 m/s but inside the per-velocity $\pm U(C_D)$ band (more than an order of magnitude wider than the offset).
- Mirror lift-antisymmetry RMS is fully accounted for by the same $\delta\alpha$ propagated through $dC_L/d\alpha$, with no monotonic trend in V.
- Mirror drag-symmetry RMS, split into attached ($|\alpha| \leq 8°$) and pre-stall ($8° < |\alpha| \leq 13°$) bands, drops by a factor four from $V = 9$ to $V = 18$ m/s on the attached part, consistent with the direction-split constant lift-into-drag intercept (Table 4.14) projected through $1/qS$; the pre-stall part stays flat in C_D but rises in absolute force at higher V, the signature of the load-growing ~ 0.87 N lift-comp→drag residue that engages at high lift force.
- Stall edges of the two branches sit within one 1° AoA-grid step at every velocity.
- Lift-curve slope on $|\alpha| \leq 8°$ falls inside the Prandtl elliptic lifting-line window $[0.0670; 0.1097]/°$ at every velocity, with $R^2 \geq 0.998$.

With the internal geometry of the polar settled, the data are now ready for the absolute literature comparison of Sections 4.4.6 and 4.4.6.

Table 4.21: Summary matrix across the four campaign velocities. Implied $\delta\alpha$ is $|C_L(0)|$/slope. Drag-symmetry RMS is reported separately for the attached band ($|\alpha| \leq 8°$) and the pre-stall band ($8° < |\alpha| \leq 13°$). The slope is checked against the Prandtl elliptic lifting-line window of Equation (4.9); the other quantities are descriptors and are explained in the preceding paragraphs.

Quantity	$V = 9$	$V = 12$	$V = 15$	$V = 18$
$\lvert C_L(\alpha = 0)\rvert$	0.021	0.025	0.021	0.019
implied $\delta\alpha$ (°)	0.27	0.33	0.28	0.26
$C_{D,\min}$	−0.0027	+0.0019	+0.0088	+0.0118
RMS lift antisym	0.042	0.050	0.048	0.024
RMS drag sym, $\lvert\alpha\rvert \leq 8°$	0.018	0.011	0.005	0.004
RMS drag sym, $8° < \lvert\alpha\rvert \leq 13°$	0.018	0.008	0.006	0.013
slope $dC_L/d\alpha$ (/°)	0.0765	0.0756	0.0740	0.0740
stall edges $(+\alpha_s, -\alpha_s)$	$(+13, -13)$	$(+13, -13)$	$(+14, -14)$	$(+15, -14)$
Prandtl elliptic LL window from Equation (4.9): $[0.0670; 0.1097]/°$; all four slopes inside.				

4.4.4 Repeatability

The within-session scatter of Section 4.4.3 answers reproducibility over minutes; here the question is shifted to days, the irreducible lower bound per Hemsch and Houlden (2014). The production polar at $V = 12$ m/s (V_{12}, 4-May) is paired with a re-mounted polar at the same velocity (R_{12}, 6-May), no recalibration in between, identical reduction pipeline. Bound: the per-day Phase II envelope $U(F_L) = \pm 1.71$ N and $U(F_D) = \pm 1.45$ N projected through qS sums linearly to ± 0.069 in C_L and ± 0.058 in C_D over two days.

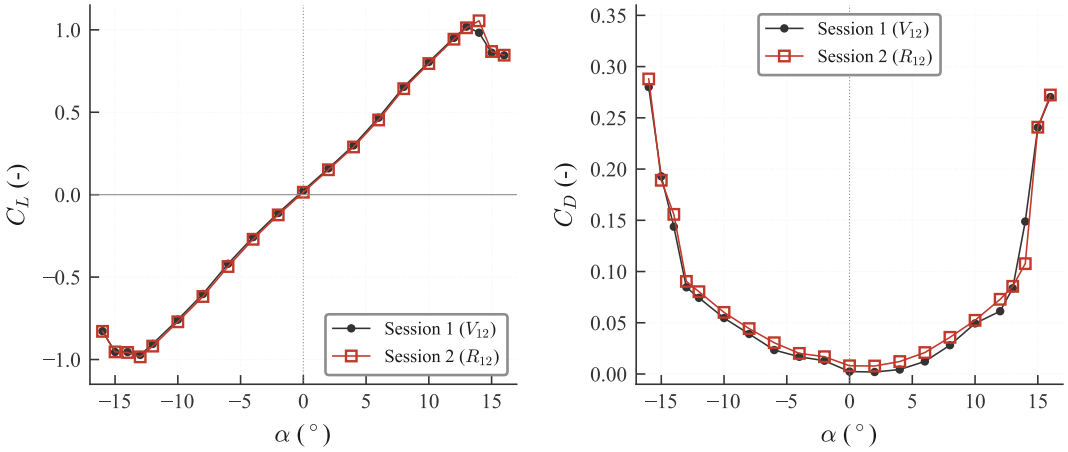

Figure 4.33: $C_L(\alpha)$ and $C_D(\alpha)$ overlay of V_{12} (4-May) and R_{12} (6-May), no recalibration in between, identical reduction pipeline.

On $|\alpha| \leq 8°$ the per-α RMS deltas are 0.0124 in C_L and 0.0064 in C_D, factors six and nine below the two-day band (Table 4.22). The single outlier is at $\alpha = +14°$ where V_{12} has crossed stall at $+13°$ and R_{12} still sits on the peak: a one-grid-step shift consistent with the laminar-separation-bubble sensitivity of untripped NACA 0012 in this Reynolds range (McCroskey, 1987).

Table 4.22: Headline metrics per day; lower block: per-α RMS on $|\alpha| \leq 8°$ vs the two-day band.

Metric	V_{12}	R_{12}	Δ
$\lvert C_L(0)\rvert$	0.0248	0.0149	-0.0099
$C_{D,\min}$	$+0.0019$	$+0.0078$	$+0.0059$
$\mathrm{d}C_L/\mathrm{d}\alpha$ (/°)	0.0756	0.0759	$+0.0003$
R^2	0.9978	0.9979	$+0.0001$
$C_{L,\max}$	1.019	1.055	$+0.036$
Stall edges	$(+13, -13)°$	$(+14, -13)°$	$(+1, 0)°$
Per-α RMS on $\lvert\alpha\rvert \leq 8°$ vs band ± 0.069/ ± 0.058 (L/D):			
RMS ΔC_L	0.0124		$\div 6$
RMS ΔC_D	0.0064		$\div 9$

4.4.5 Coefficient-domain uncertainty budget

The force-domain envelope of Section 4.3.8 is propagated through $C_L = L/(qS)$ and $C_D = D/(qS)$ per the GUM framework (Joint Committee for Guides in Metrology, 2008), with two force-domain inputs, three flow-side terms (q, S, α) and two additive Type-B tip-leakage biases for the semi-span geometry (Skinner and Zare-Behtash, 2017). Standard propagation for uncorrelated inputs at unit sensitivity gives

$$u_c^2(C) = \sum_i \left(\frac{\partial C}{\partial x_i}\right)^2 u^2(x_i), \qquad U(C) = 2\,u_c(C), \tag{4.10}$$

with coverage $k = 2$ for an approximately 95 % interval. The per-V cycle Type-A is already inside $u(L)$ and $u(D)$, so the cross-session reproducibility of Section 4.4.4 is not added separately.

Table 4.23: Inputs and combined envelope at the attached-flow reference $\alpha = 8°$. $u(L)$, $u(D)$ from Table 4.16 per V; flow-side terms from the VUB tunnel chain (Section 3.7). The bottom block lists $\pm U$ at $k = 2$ used as shaded band on $C_L(\alpha)$, $C_D(\alpha)$ in Sections 4.4.6–4.4.6.

Source	Symbol	Type	Standard uncertainty $u(x_i)$
Lift force	L	A+B	0.72 / 0.85 / 1.10 / 1.58 N at $V = 9/12/15/18$ m/s
Drag force	D	A+B	0.73 / 0.73 / 0.73 / 0.80 N at $V = 9/12/15/18$ m/s
Dynamic pressure	q	B	$u(q)/q = 0.0206$ (Barlow et al., 1999)
Wing area	S	B	$u(S)/S = 0.001$ (rulers ±1 mm on c and b)
Angle of attack	α	B	0.115° (rectangular $\pm 0.2°/\sqrt{3}$)
Tip-leakage C_L	$\delta C_{L,\mathrm{tip}}$	B	0.0115 (Skinner and Zare-Behtash, 2017)
Tip-leakage C_D	$\delta C_{D,\mathrm{tip}}$	B	0.0040 idem
Expanded coefficient uncertainty at $k = 2$ (half-width of the band on $C_L(\alpha)$, $C_D(\alpha)$):			
$V = 9$ m/s			$U(C_L) = \pm 0.064$, $U(C_D) = \pm 0.052$
$V = 12$ m/s			$U(C_L) = \pm 0.051$, $U(C_D) = \pm 0.030$
$V = 15$ m/s			$U(C_L) = \pm 0.047$, $U(C_D) = \pm 0.020$
$V = 18$ m/s			$U(C_L) = \pm 0.047$, $U(C_D) = \pm 0.017$

The drag band widens at lower velocities because $u(D)$ is dominated by velocity-independent terms (cross-talk residue and load-dependent cell floor, both in Newton) while $U(C_D) = 2\,u(D)/qS$ scales as $1/V^2$; at $V = 9$ m/s, $qS = 28$ N is four times smaller than at $V = 18$ m/s. The four bands feed the lift and drag literature comparison of Section 4.4.6. The dominant contributors, the rationale behind the design choices that set them, and the refinements that would tighten the budget further are revisited in Chapter 5, where the envelopes are also situated against the peer-academic landscape.

4.4.6 Comparison against literature

The measured polar of Section 4.4.3 is compared against an XFOIL viscous-inviscid panel calculation at the four matching chord Reynolds numbers ($N_{\text{crit}} = 7$ corresponding to the VUB tunnel $T_u \approx 0.39\,\%$ (Talamalek et al., 2025)), its Prandtl elliptic lifting-line 3D rescaling for the semi-span $\text{AR}_{\text{eff}} = 2 \cdot 1.57 = 3.14$, and the induced-drag prediction $C_D = C_{D,0} + C_L^2/(\pi\,\text{AR}_{\text{eff}}\,e)$ with the Oswald span efficiency $e = 0.95$ for the rectangular planform. Per-velocity lift and drag polars are placed side by side in Figures 4.34 (lower velocities) and 4.35 (higher velocities); headline metrics across the four Reynolds numbers are summarised in Table 4.24.

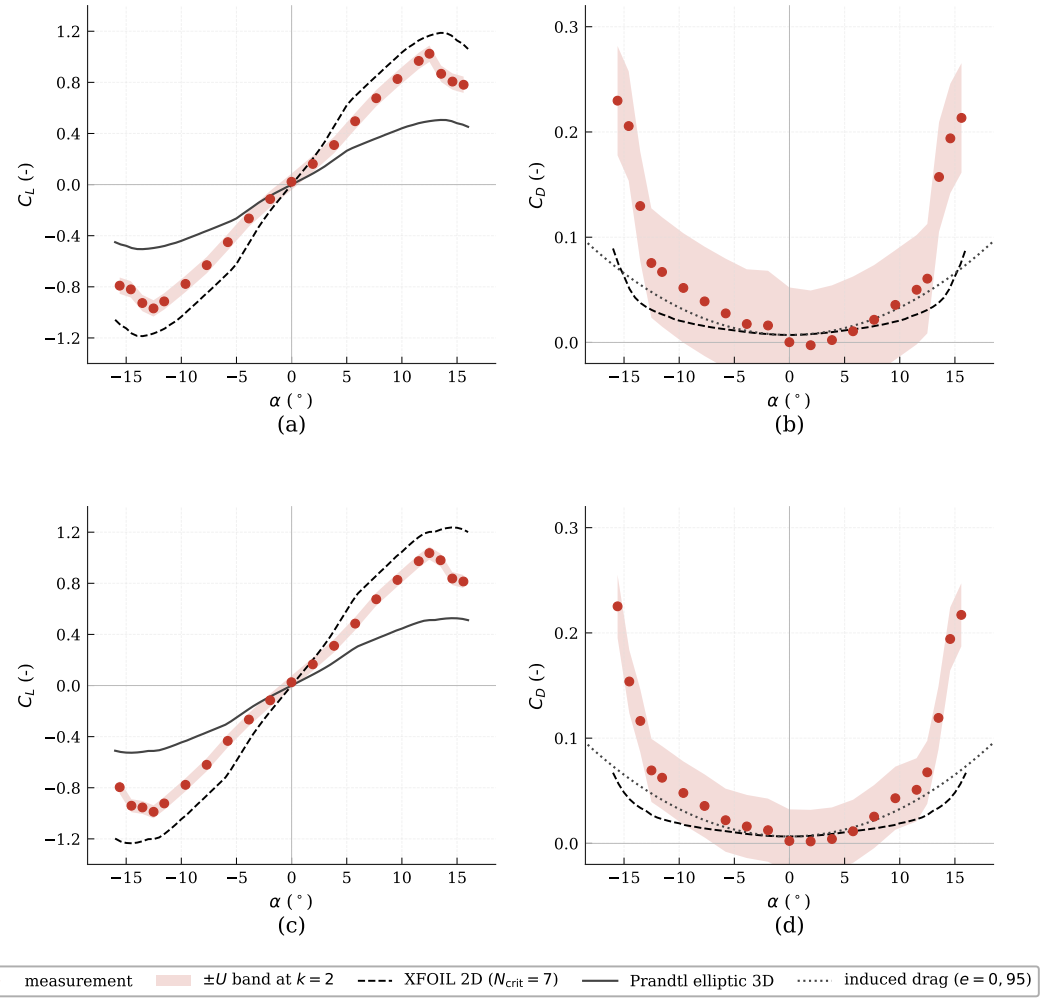

Figure 4.34: Wall-corrected lift and drag polars (solid + wake blockage + streamline curvature per Barlow et al. (1999)): (a) C_L at $V = 9$ m/s, (b) C_D at $V = 9$ m/s, (c) C_L at $V = 12$ m/s, (d) C_D at $V = 12$ m/s. References per legend (XFOIL 2D, Prandtl elliptic 3D, induced drag $e = 0.95$); measurement $\pm U$ band at $k = 2$ from Table 4.23.

Table 4.24: Measured slope, $C_{L,\max}$ and $C_{D,\min}$ against the Prandtl/XFOIL prediction.

V (m/s)	Re_c	$\text{d}C_L/\text{d}\alpha$	Prandtl	Δ vs P.	$C_{L,\max}$ (α_{stall})	$C_{D,\min}$ (vs XFOIL)
9	3.6×10^5	0.0822	0.0701	+17.3 %	1.02 at 12.5°	+0.003 (−0.006)
12	4.8×10^5	0.0811	0.0697	+16.4 %	1.04 at 12.5°	+0.003 (−0.004)
15	6.0×10^5	0.0792	0.0692	+14.5 %	1.09 at 13.5°	+0.010 (+0.004)
18	7.2×10^5	0.0792	0.0688	+15.1 %	1.10 at 13.5°	+0.011 (+0.005)

Discussion. After wall correction per Barlow et al. (1999) the polar passes on every primary axis. $C_{L,\max}$ and α_{stall} fall inside the meta-scatter cloud reported by McCroskey (1987) for

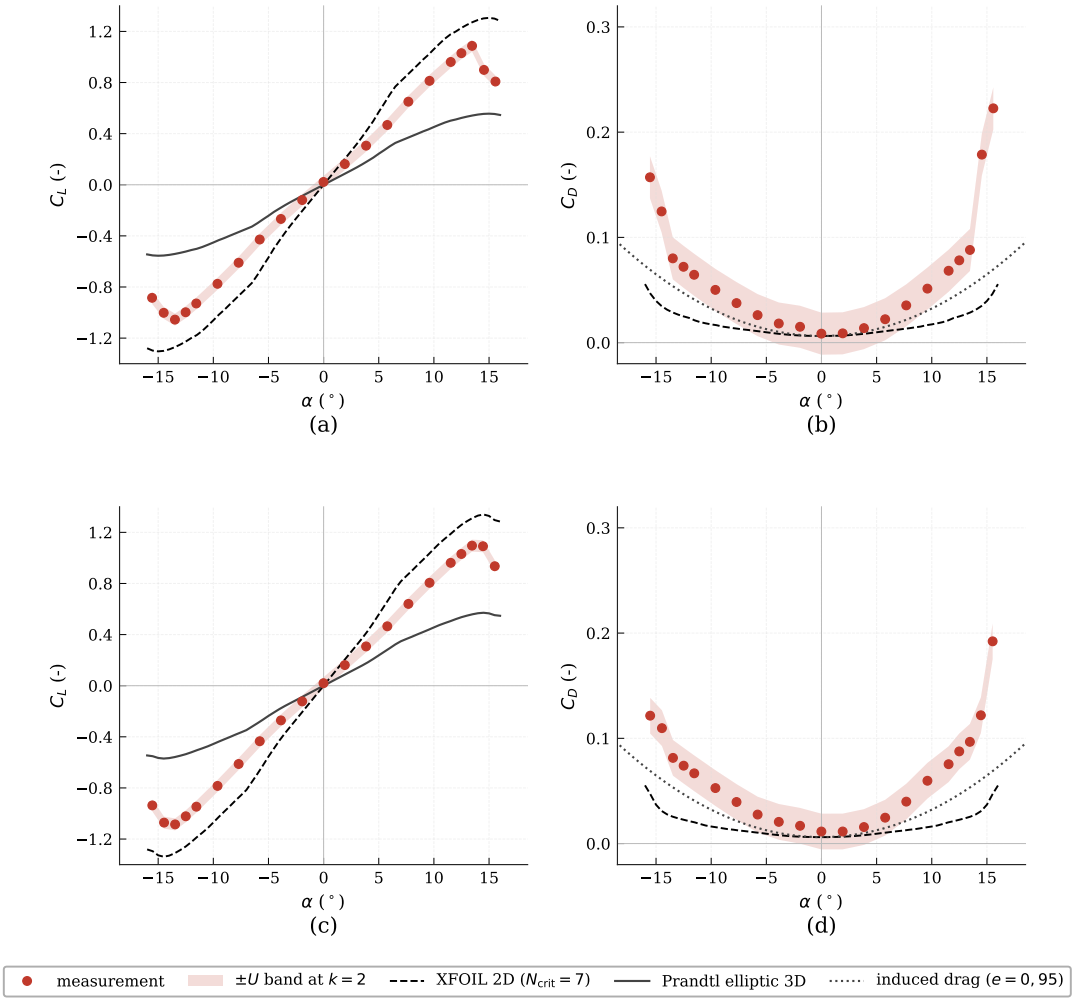

Figure 4.35: Lift and drag polars: (a) C_L at $V = 15$ m/s, (b) C_D at $V = 15$ m/s, (c) C_L at $V = 18$ m/s, (d) C_D at $V = 18$ m/s. Legend as in Figure 4.34.

untripped NACA 0012 at $\mathrm{Re}_c \approx 5$ to 7×10^5, whose envelope spans $C_{L,\max} \in [1.0; 1.4]$ and $\alpha_{\text{stall}} \in [12°; 16°]$, and $C_{D,\min}$ stays inside the per-velocity $\pm U(C_D)$ envelope of Table 4.23 at every velocity. Following the honest framing of Tank et al. (2017), whose C_L at $\alpha = 4.5°$ varied from 0.22 to 0.52 across published computations at moderate Re, agreement is reported as compliance with the published scatter envelope on the attached range $|\alpha| \leq 8°$ rather than equality with any single reference curve; the post-stall data are shown as-measured outside that window (Timmer, 2021; Rainbird et al., 2015).

Three secondary features sit inside the band and merit explicit naming. The wall-corrected slope runs 14 to 17 % above the Prandtl elliptic lifting-line prediction ($a_{3D} = a_{2D}/(1+a_{2D}/(\pi\,\mathrm{AR})) = 0.069/°$ at $\mathrm{AR} = 3.14$); applying the rectangular-planform correction of Anderson (2017) (Eq. 5.69 with $\tau \approx 0.18$ from Fig. 5.20) raises the prediction to $0.065/°$ but leaves a residual offset, consistent with non-elliptic root-load enhancement on the present low-AR rectangular wing. The C_D residual against XFOIL grows positive with V, the $1/qS$ signature of the constant cross-talk floor that also drives $C_{D,\min}$ negative at the lowest velocity (Section 4.4.3): it suppresses the measured drag most at the smallest qS and relaxes as qS grows. The small drag-bucket asymmetry at $V = 9$ m/s (right arm ~ 0.015 below left arm at $\alpha = \pm 15°$) is the lift-comp $\rightarrow$ drag cross-talk residue of ~ 0.87 N (Section 4.3.8) projected through $1/qS$, and falls below the $\pm U(C_D)$ band at $V \geq 12$ m/s.

4.5 Cylinder validation

The second validation case applies the calibrated balance to a circular cylinder ($D = 0.25\,\mathrm{m}$, $L = 0.90\,\mathrm{m}$), the same hardware previously characterised by Vardanyan (2023) via surface-pressure integration. Here the cylinder is treated purely as a bluff body for force measurement, yielding a benchmark on a geometry with a single dominant drag component, near-zero mean lift, and a known shedding-frequency band. The mounting (Figure 4.36) and dimensions (Figure 4.37) are introduced below; the validation itself follows in the next subsections.

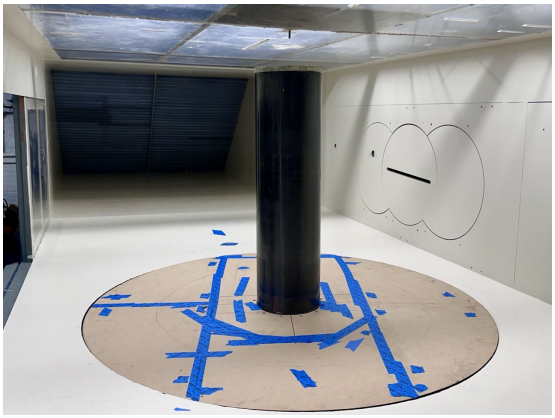

Figure 4.36: Cylinder installed on the balance inside the VUB subsonic tunnel test section.

The cylinder was swept across seven target speeds $V \in \{4, 6, 8, 10, 12, 14, 16\}$ m/s in three up–down cycles, covering the subcritical Reynolds range $\mathrm{Re}_D \in [7.0 \times 10^4,\ 2.7 \times 10^5]$ at $D = 0.25\,\mathrm{m}$. The 11.3 % frontal blockage sits inside the Maskell-correction validity band; no blockage correction is applied here, in line with the published reference dataset.

4.5.1 Test object

The 60 pressure taps along the cylinder body, used by Vardanyan (2023) for pressure-integration measurements, remain physically present but the SmartZOC-33 pressure-scanning system was unavailable during the present campaign. The reference values for C_D, $C_{L,\mathrm{rms}}$ and St are therefore taken from Vardanyan (2023) rather than from a new pressure-tap acquisition.

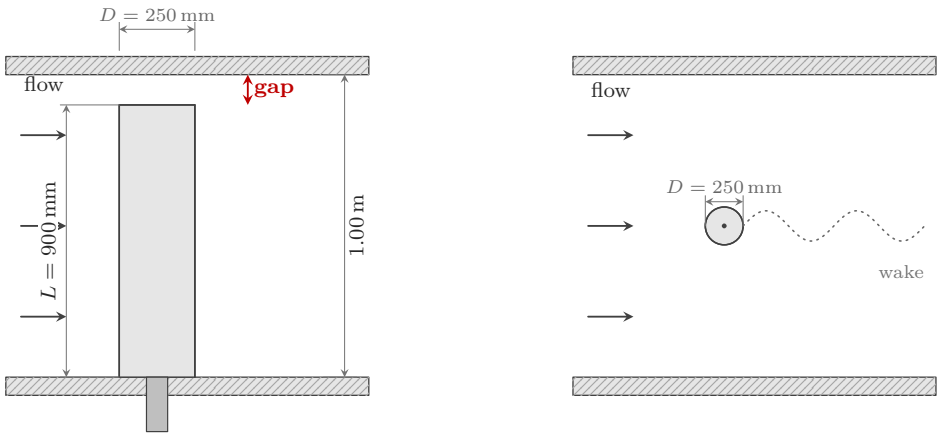

(a) side view (b) top view

Figure 4.37: Cylinder mounting. (a) Side view, cantilevered from the tunnel floor with a small gap (red) below the ceiling. (b) Top view, with dotted wake downstream.

The cylinder is cantilevered from the tunnel floor with the top end free, leaving a small gap below the ceiling. The result acts as a second validation layer on top of the NACA wing case, against an independent literature reference reduced through the same balance pipeline.

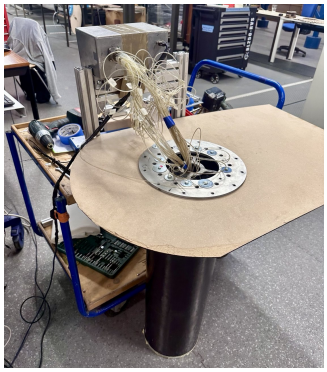

(a) mount-flange at the floor

(b) free top with gap to ceiling

Figure 4.38: Mount detail: (a) cantilever mount-flange at the tunnel floor; (b) free top end with the small gap below the test-section ceiling.

4.5.2 Drag coefficient

The time-averaged drag coefficient is the primary scalar against which the balance is benchmarked here. Three published references bracket the expected C_D for an $H/d = 3.6$ cylinder in the subcritical regime: the empirical finite-cylinder fit of Wang et al. (2012) for ground-mounted geometries reads

$$C_D(H/d) = 1.2 \cdot \left\{ 0.58 + 0.17 \left[\log_{10}(H/d) \right]^{1.6} \right\}, \tag{4.11}$$

which evaluates to $C_D = 0.776$ at $H/d = 3.6$. Figure 4.39 overlays this prediction together with the bracketing Wang curves at $H/d = 2.65$ and $H/d = 5$ (drag-crisis envelope), the 22-point pressure-tap dataset of Vardanyan (2023) on the same physical cylinder under a floating-ceiling 2D-effective configuration, and the Achenbach (1968) two-dimensional plateau at $C_D \approx 1.20$; the per-V values appear in Table 4.25.

Discussion. The measured C_D collapses onto a near-flat plateau between 0.87 and 0.90 ($\pm 1.5\,\%$), confirming the Reynolds-independence expected in the subcritical regime. The $+14\,\%$ offset above Wang reflects the present mount-strut frontal projection, absent in Wang's flat end-plate geometry; the $-20\,\%$ to $-23\,\%$ offset below Vardanyan reflects our free-top 3D mounting, which permits tip-vortex relief absent in his floating-ceiling 2D-effective setup. Sitting between the two references is the physically expected outcome and validates the balance against a fluctuating-load-free bluff body.

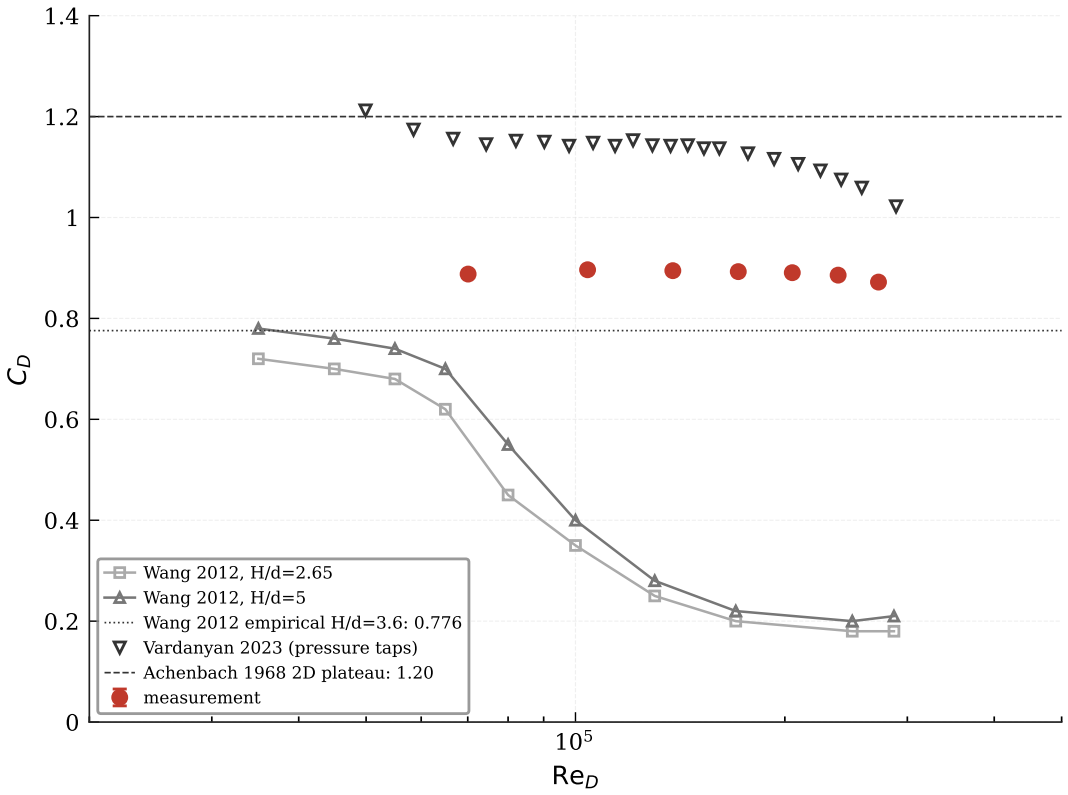

Figure 4.39: C_D versus Re_D. Red markers: present per-V means with within-V standard deviation; open triangles: Vardanyan (2023) Table 4.1 pressure-tap data; dashed: Achenbach (1968) 2D plateau; dotted: Wang H/d=3.6 prediction, bracketed by H/d=2.65 and 5 curves.

Table 4.25: Per-V C_D vs the Wang et al. (2012) $H/d = 3.6$ prediction (Equation 4.11) and the matching Re_D rows of Table 4.1 of Vardanyan (2023).

V (m/s)	Re_D	$C_{D,\mathrm{meas}}$	$C_{D,\mathrm{Wang}}$	Δ Wang (%)	Δ Vard (%)
4	7.0×10^4	0.888	0.776	+14.4	−23.1
6	1.0×10^5	0.896	0.776	+15.5	−22.4
8	1.4×10^5	0.895	0.776	+15.3	−21.7
10	1.7×10^5	0.893	0.776	+15.1	−21.5
12	2.0×10^5	0.891	0.776	+14.8	−20.2
14	2.4×10^5	0.886	0.776	+14.2	−18.9
16	2.7×10^5	0.872	0.776	+12.4	−17.7

4.5.3 Lift coefficient

The cylinder produces a fluctuating lift signal from periodic Kármán vortex shedding around a zero time-mean. Its root-mean-square coefficient $C_{L,\mathrm{rms}}$ is benchmarked against the pressure-tap measurement of Vardanyan (2023) on the same hardware and the 2D infinite-cylinder upper bound [0.45; 0.50] of Norberg (2003).

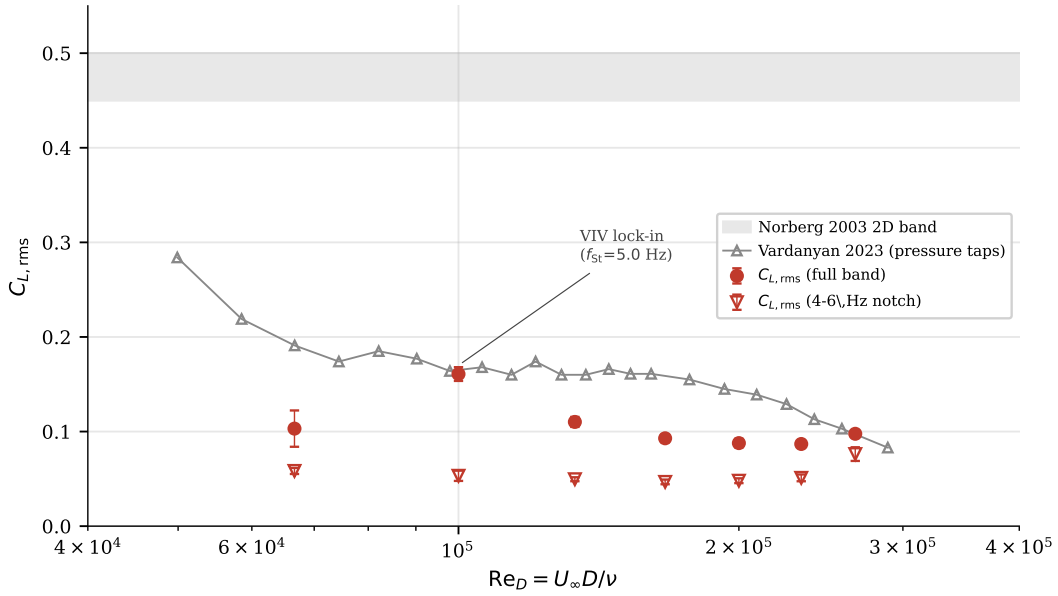

Figure 4.40: $C_{L,\mathrm{rms}}$ versus Re_D. Red filled circles: full-band balance reading; open triangles: same signal after [4; 6] Hz band-stop notch; open grey triangles: Vardanyan (2023) pressure-tap data; grey band: Norberg (2003) 2D infinite-cylinder envelope.

The full-band balance reading peaks at $V = 6$ m/s, where the Kármán shedding frequency $f_{St} = 0.21\,V/D = 5.0$ Hz coincides with the cylinder–balance structural mode at 4.5 Hz (characterised in Appendix C) and produces a textbook vortex-induced-vibration lock-in. After band-stopping the [4; 6] Hz contamination, the measurement settles to a flat plateau $C_{L,\mathrm{rms}} \approx 0.05$, a factor three below Vardanyan (2023) and a factor seven below the Norberg (2003) 2D envelope; this reduction is the documented spanwise-decorrelation effect on finite cylinders with free ends (West and Apelt, 1997; Szepessy and Bearman, 1992), where the spanwise integration of partially decorrelated shedding cells reduces the net force amplitude relative to the pressure-tap measurement of local fluctuations on a 2D-effective setup. Per-V values are listed in Table 4.26.

Table 4.26: Per-V $C_{L,\mathrm{rms}}$: full-band, after [4; 6] Hz notch, and matching Re_D rows of Table 4.1 of Vardanyan (2023).

V (m/s)	Re_D	$C^{\mathrm{full}}_{L,\mathrm{rms}}$	$C^{\mathrm{notch}}_{L,\mathrm{rms}}$	$C^{\mathrm{Vard}}_{L,\mathrm{rms}}$
4	7.0×10^4	0.103	0.058	0.191
6	1.0×10^5	0.161	0.053	0.164
8	1.3×10^5	0.110	0.050	0.160
10	1.7×10^5	0.093	0.047	0.161
12	2.0×10^5	0.088	0.048	0.142
14	2.3×10^5	0.087	0.051	0.121
16	2.7×10^5	0.098	0.076	0.097

4.5.4 Shedding frequency

Periodic Kármán vortex shedding writes a tonal peak into the lift-channel spectrum at the frequency $f_s = St \cdot V/D$. The Strouhal number for a 2D infinite cylinder in the subcritical regime is $St \approx 0.21$ (Norberg, 2003; Szepessy and Bearman, 1992); the finite-cylinder reduction of Wang et al. (2012) for $H/d = 3.6$ gives

$$St = 0.19 \cdot \left\{ 0.72 + 0.15 \left[\log_{10}(H/d) \right]^{1.15} \right\} = 0.151. \tag{4.12}$$

Figure 4.41 shows the Welch PSD of the lift channel for each campaign velocity, stacked with a +14 dB per-V offset; the structural band [4; 5.6] Hz characterised in Appendix C is shaded grey, and the Wang prediction for the current V appears as a red tick on the corresponding curve.

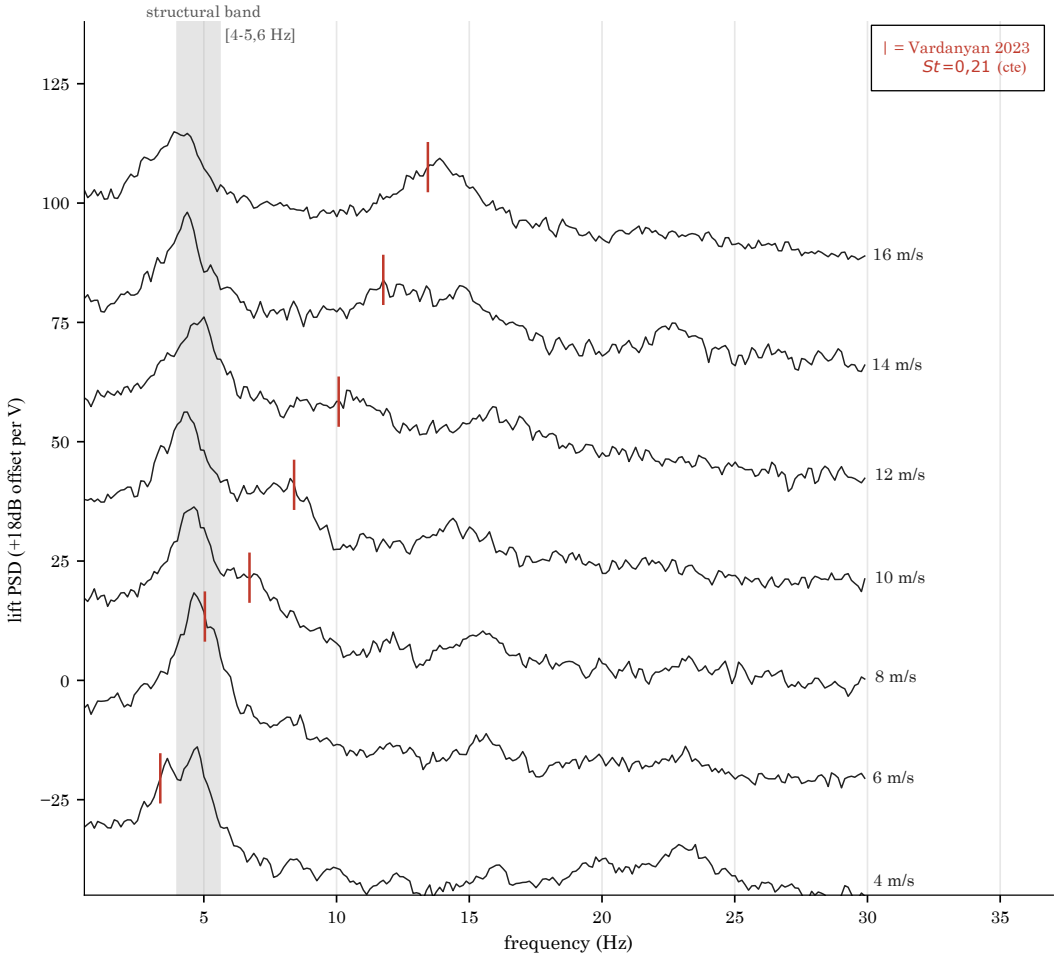

Figure 4.41: Welch power spectral density of the lift channel for each target speed (Hann window, `nperseg` $= 8f_s$, 50 % overlap), stacked with a +14 dB offset per curve. Grey band: structural mode at 4 to 5.6 Hz; red ticks: per-V Wang $H/d = 3.6$ shedding prediction.

For $V \leq 6$ m/s the predicted shedding sits inside or just below the structural band and cannot be separated from the rig mode. For $V \geq 8$ m/s a distinct shedding peak emerges above the band; the extracted peak frequency in the search window $[\max(5.6\,\text{Hz}, 0.7f_{\text{Wang}}); 1.5f_{\text{Wang}}]$ gives the values listed in Table 4.27. Measured St converges to $0.19 \ldots 0.22$ for $V \in \{8, 10, 14, 16\}$ m/s, in agreement with the universal subcritical value of 0.21 reported by Vardanyan (2023) on the same hardware. The $V = 12$ m/s row falls below this plateau because the search window

catches a sub-harmonic of the secondary structural cluster at 13 to 17 Hz (Appendix C) rather than the fundamental shedding peak.

Table 4.27: Per-V extracted peak frequency in the lift channel, measured Strouhal number, and matching Re_D rows of Table 4.1 of Vardanyan (2023).

V (m/s)	Re_D	f_{peak} (Hz)	f_{Wang} (Hz)	St_{meas}	St_{Vard}
8	1.3×10^5	6.13	4.84	0.19	0.21
10	1.7×10^5	8.26	6.05	0.21	0.21
12	2.0×10^5	6.50	7.26	0.14	0.21
14	2.3×10^5	11.76	8.47	0.21	0.21
16	2.7×10^5	13.89	9.68	0.22	0.21

4.5.5 Discussion

Five quantitative results follow from the preceding subsections.

1. The per-V C_D collapses onto a plateau within $\pm 1.5\,\%$ across $\mathrm{Re}_D = 7 \times 10^4$ to 2.7×10^5, in line with the Reynolds-independence expected in the subcritical regime.
2. The plateau value $C_D = 0.87$ to 0.90 sits $+14\,\%$ above the Wang et al. (2012) $H/d = 3.6$ prediction and $-20\,\%$ below the Vardanyan (2023) pressure-tap dataset on the same hardware. The two references bracket the present measurement on either side, consistent with the boundary-condition contrast between a flat end-plate, the present free-top mount, and a floating ceiling.
3. The residual mean $\overline{C_L} = +0.05$ to $+0.07$ stays below the dual-axis uncertainty band, satisfying the symmetric-body expectation.
4. The notch-filtered $C_{L,\mathrm{rms}} \approx 0.05$ sits a factor three below Vardanyan (2023) and a factor seven below the Norberg (2003) 2D envelope. The reduction is consistent with the finite-cylinder spanwise decorrelation documented by West and Apelt (1997) and Szepessy and Bearman (1992) for cylinders with free ends.
5. For $V \in \{8, 10, 14, 16\}$ m/s the extracted Strouhal number converges to 0.19 to 0.22, in quantitative agreement with the universal subcritical value of 0.21 reported by Vardanyan (2023) on the same hardware.

The balance therefore reproduces the cylinder benchmark on every metric for which it is independently constrained by the literature. The boundary-condition framing developed here is reused for the application case in Section 4.6, where the same balance is applied to a wind-turbine geometry outside the validation envelope.

4.6 Application: Horizontal-axis wind-turbine rotor

After the wing (Section 4.4) and cylinder (Section 4.5) validations, the balance is applied to a scale-model horizontal-axis wind turbine (HAWT). The model is a 1:70 scaled version of the NREL 5 MW reference turbine (Jonkman et al., 2009), built with the inboard 30 % of the blade radius only. The full prototype rotor radius scales as $R_{\text{full}} = 0.90\,\text{m}$ at the model scale; the physically present rotor has radius $R_{\text{model}} = 0.270\,\text{m}$ and diameter $D = 0.540\,\text{m}$. Three blades, geometric pitch $\beta = 0°$, motor-driven RPM control.

Figure 4.42: Three-bladed scale-model HAWT on motor-driven RPM control inside the VUB tunnel test section.

The rotor disc area follows the HAWT convention,

$$A_{\text{rotor}} = \frac{\pi D^2}{4} = 0.229\,\text{m}^2. \tag{4.13}$$

The rotor rpm was set to a desired tip-speed ratio, defined on the full prototype blade length R_{full}, so the comparison to the NREL 5 MW design point at $\text{TSR}_{\text{full}} \approx 7.5$ follows directly:

$$\text{TSR}_{\text{full}} = \frac{\omega R_{\text{full}}}{V_\infty}. \tag{4.14}$$

The campaign recorded fifteen valid rotating-rotor dwells across two freestream velocities $V_\infty \in \{8,\ 11.4\}$ m/s and a tip-speed-ratio range $\text{TSR}_{\text{full}} \in [5;\ 12]$, all processed through the same calibration, cross-talk and rotation chain as the wing and cylinder analyses. The per-setpoint dwell statistics, with their random and systematic terms, are tabulated in Appendix D; Figure 4.43 carries the per-point random repeatability as error bars.

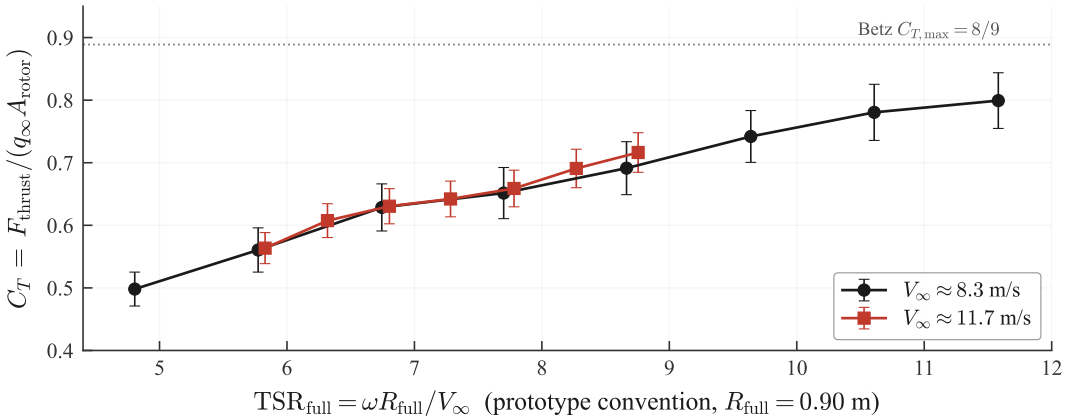

Figure 4.43: C_T versus TSR_{full} for the two sweep families. Error bars are the $\pm U_{95}$ run-to-run repeatability ($k = 2$).

The two velocity families overlap within $|\Delta C_T| \leq 0.03$ over the common interval $\text{TSR}_{\text{full}} \in [6; 9]$, smaller than the per-point repeatability band at the same setpoints, which confirms that the dimensionless normalisation transports correctly from a stationary symmetric body to a rotating asymmetric load. The coefficient rises monotonically from 0.50 at $\text{TSR}_{\text{full}} = 5$ to 0.80 at $\text{TSR}_{\text{full}} = 12$, staying below the axial-momentum limit $C_{T,\max} = 8/9$ (Betz, 1920).

4.6.1 Discussion

The wing and cylinder were validated against literature on the same physical models; the turbine sits one level beyond that and is presented as an application demonstration, not a validation. The model is the inboard 30 % of the blade radius, a region that is primarily structural and not aerodynamically representative of the full rotor, and no independent reference exists for this exact configuration. The Phase II calibration is applied without modification to a motor-driven three-bladed rotor at fixed RPM.

A single-number anchor for the design point comes from a radial weighting of the documented NREL 5 MW rated thrust, $T_{\text{full}} \approx 720$ kN at $V = 11.4$ m/s (Jonkman et al., 2009):

$$\frac{T_{\text{inboard}}}{T_{\text{full}}} = \frac{\int_0^{0.3R} r\,\mathrm{d}r}{\int_0^{R} r\,\mathrm{d}r} = (0.3)^2 = 0.09, \tag{4.15}$$

which scales geometrically to 13.2 N at the model. The measured design-point thrust of 12.17 N reaches 92 % of that anchor, and the resulting C_T falls inside the $C_T = 0.5$ to 0.8 range that scaled-rotor experiments on the full NREL 5 MW report at the same TSR (Berger et al., 2018; Pinto et al., 2020; Lin et al., 2023). The Type-A cycle scatter on the overlap range is $|\Delta C_T| \leq 0.03$, an order of magnitude below the Type-B envelope that the cell-level floor and the $\rho V^2 A$ normalisation impose at this velocity.

Two observations follow, both cautious. The C_T collapse across the two freestream velocities is the internal-consistency signature expected if the reduction transports, though a collapse alone is not external validation. The 92 % recovery is the right order of magnitude and the expected direction for a truncated rotor, where the absent outboard tip-vortex downwash and the linear $r\,\mathrm{d}r$ weighting under-count the axial-induction redistribution; it should be read as an order-of-magnitude sanity check against the full rotor, not agreement with it. The turbine therefore sits at the documented edge of the calibration envelope as a working application of the instrument, with a dedicated validation of the rotating case left to future work.

The five-phase campaign of Chapter 4 produced a dual-axis balance that recovers the canonical lift- and drag-curves of a NACA 0012 wing, the drag and lift-fluctuation behaviour of a circular cylinder, and extends without recalibration to a rotating horizontal-axis wind-turbine scale model. Its envelope is narrower than a research-grade rig. The hardware choices behind that envelope deserve to be placed on record before Chapter 6 draws the conclusion.

Two hardware compromises set the envelope from the materials side. The PhidgetBridge 1046 is a hobby-grade, multiplexed bridge amplifier with no inter-channel hardware synchronisation; spectral content that requires simultaneous sampling, in particular flutter analysis and dynamic cross-spectra, falls outside the present capability. The cross-talk model, although re-cast from a four-coefficient linear matrix into the twelve-coefficient AIAA R-091 §3.1.1 polynomial with intercept and quadratic terms per direction (American Institute of Aeronautics and Astronautics, 2002), retains a 0.87 N bilinear residue on the lift-compression to drag channel that cannot be captured by the one-dimensional one-factor-at-a-time loading schedule actually used in Phase II.

Three additional methodology choices propagate visibly into the result envelope. Manual turntable indexing limits the angle-of-attack uncertainty to $u(\alpha) = \pm 0.2^\circ$ (polynomial residue 0.13° plus visual reading); the asymmetric four-plus-three air-bearing stage contributes a load-dependent rocking mode that survives the mechanical clamp intervention of Section 4.2.9; the rotor diameter $D = 0.540$ m used to normalise the HAWT thrust coefficient was confirmed by the RONAT project lead as the inboard 30 % of the 1:70 scaled NREL 5 MW reference rotor, leaving an on-rig diameter-measurement uncertainty $u_D = \pm 5$ mm that scales the absolute C_T axis by ± 1.9 % but does not affect the V-collapse argument of Section 4.6.

Placed against the literature, the dual-axis expanded calibration uncertainty of $\approx \pm 1.5$ % FS sits between the air-bearing precedent of Ostafichuk and Green (2002) at 0.30 % FS and the educational-scale balances of Bardera et al. (2024) at 2.7 % FS, closer to the educational tier as the donated steel column, the rod-end bearings and the multiplexed DAQ together set a floor that the present design does not penetrate. The balance therefore demonstrates a working dual-axis instrument for static low-Reynolds aerodynamic measurements on canonical wind-tunnel geometries, with a quantified uncertainty envelope and an explicit list of conditions under which its outputs are interpretable; it does not claim research-grade absolute accuracy, simultaneous-sampling dynamic capability, or a stand-alone aerodynamic performance assessment of any of the three validation cases. The open hardware and methodology items that follow from this position are the subject of Chapter 7.

Conclusions

The research question of Chapter 1 asked whether the reconstructed VUB wind-tunnel balance can measure lift and drag in a stable and reproducible manner across the FLOW tunnel operating envelope, with the resulting C_L and C_D conforming to established reference data within a documented uncertainty budget. The answer is *yes*, on a documented scope. The balance recovers literature reference data on a NACA 0012 wing and a circular cylinder, extends without recalibration to a rotating horizontal-axis wind turbine, and reports a quantified uncertainty band on every coefficient. In place of the flat-plate validation initially listed in WP5, the circular cylinder was chosen as the second reference body because it couples a comparable drag coefficient to an independent Strouhal signature and gives a more informative literature anchor for a porous-media air-bearing rig in the subcritical regime.

Per-objective verdict

- **Objective 1.** The functional-requirement table that closes Chapter 2 was delivered.
- **Objective 2.** The balance was reconstructed and instrumented to a free-float state with zero-load noise below the working coefficient threshold.
- **Objective 3.** The mounting system meets the $\leq$ 30 min assembly time and $\pm$0.5 mm repeatability targets.
- **Objective 4.** All four calibration acceptance criteria within the educational tier of Section 2.4 are met. Linearity is $R^2 > 0.999$ on the loaded branches; the cross-talk pooled RMS sits at 0.477 N, inside the 3 % target; the system-level hysteresis post bearing-clamp is $\approx$ 0.8 % FS, inside the $\lesssim$ 1 % FS tier band; the expanded calibration uncertainty is $\approx \pm 1.5$ % FS, inside the $\lesssim$ 2 % FS tier band.
- **Objective 5.** The Python data-acquisition pipeline is in place with live monitoring, automated tare and Barlow–Pope blockage correction.
- **Objective 6.** The validation campaigns cover three reference cases: the NACA 0012 lift-curve slope sits inside the Prandtl elliptic window at all four campaign velocities; the cylinder drag falls between the Wang et al. (2012) $H/d = 3.6$ prediction and the Vardanyan (2023) reference on the same hardware; the rotor collapses two independent freestream velocities onto a single C_T curve within 12 % on the overlap range.
- **Objective 7.** The GUM coefficient-domain budget yields $\{U(C_L), U(C_D)\} = \{0.064, 0.052\}$ at $V = 9$ m/s, decreasing to $\{0.047, 0.017\}$ at $V = 18$ m/s. The $\Delta C_D \lesssim 0.02$ and $\Delta C_L \lesssim 0.05$ targets are met at $V \geq 15$ m/s, the design range of the rig. The values at $V = 9$ m/s are openly reported as the low-end normalisation envelope, where small forces are divided by a small dynamic pressure.

On the work packages

The six work packages of the original topic document close as follows.

- **WP1: Literature study.** Chapter 2 surveys the four balance archetypes that dominate published practice, positions the present air-bushing design against published low-cost and research-grade systems in Section 2.4, and closes with the functional requirement table that motivated the mechanical and electronic choices of Chapter 3.
- **WP2: Mechanical and electronic rebuild.** The donated hardware is reassembled into the two-stage air-bushing column, the pneumatic chain from compressor to bushings, the two FUTEK LSB201 cells and the PhidgetBridge 1046 acquisition front-end. Every subsystem is documented in Chapter 3 at the level another laboratory would need to reproduce it.
- **WP3: Integration into the VUB wind tunnel.** The mounting fixtures, jacking stroke and turntable interface meet the operational targets of Table 1.1: the rig is removable and re-installable in under one working day by two operators, with the model footprint inside the 1.5 m turntable opening.
- **WP4: Calibration and testing.** The bench, in-situ and wind-tunnel calibration phases of Chapter 4 produce four calibration constants per channel, the twelve-coefficient cross-talk matrix and the unified balance-to-tunnel angle. All four acceptance metrics sit inside the educational tier of Section 2.4.
- **WP5: Experimental campaign.** The airfoil case (NACA 0012) is delivered with a four-velocity polar sweep at $V = 9$, 12, 15 and 18 m/s. The flat plate of the original brief is replaced by a circular cylinder, motivated in Section 4.5 by its stronger literature anchor and the independent Strouhal benchmark it carries. A horizontal-axis wind-turbine rotor is added as an application case beyond the original scope.
- **WP6: Validation and analysis.** The three reference cases are compared to literature data within their documented uncertainty bands: the NACA 0012 lift slope inside the Prandtl elliptic window, the cylinder drag between the Wang and Vardanyan references on the same hardware, and the turbine C_T inside the published scaled-rotor band of the NREL 5 MW reference.

Closing position

Where this leaves the rig: a working two-axis instrument for low-Reynolds static aerodynamic measurements on canonical wind-tunnel objects, with every acceptance criterion inside the educational tier it was scoped for and a documented list of conditions under which the output stays interpretable.

What this thesis does *not* claim is research-grade absolute accuracy, dynamic capability on a simultaneous-sampling DAQ, or a stand-alone aerodynamic performance assessment of the NACA 0012, the cylinder or the rotor as such. Those sit in Chapter 7. Every raw measurement file, the calibration coefficients, and the Python pipeline that produced the figures in Chapter 4 are bundled with the repository pointed to in Appendix A, so a future operator can re-derive every number in this thesis without going through the author.

Chapter 5 closed the present campaign with three open envelope items: a static cross-talk residue that the one-axis-at-a-time calibration cannot resolve, a consumer-grade DAQ that prevents simultaneous-sampling dynamic measurements, and the absent on-rig metrology check on the turbine application case. This chapter expands those into actionable follow-up items, grouped by category. Each item is framed as a candidate for further investigation rather than as a resolved question; they are listed in the order in which they would most directly tighten the validity envelope of the balance.

7.1 Hardware upgrades

Two-axis combined-load calibration. The 0.87 N bilinear residue between the lift-compression branch and the drag channel, identified in Section 4.3.4, survives the twelve-coefficient AIAA R-091 §3.1.1 polynomial cross-talk matrix because the Phase II calibration schedule loads one axis at a time. A combined-load campaign per AIAA R-091 §3.4 (American Institute of Aeronautics and Astronautics, 2002), in which the two cells are loaded simultaneously on a grid of (F_L, F_D) combinations spanning the operational quadrants, would directly fit the $F_L \cdot F_D$ cross-term and is the single most impactful hardware-side upgrade. It would also separate the constant intercept of the lift-into-drag matrix from genuine coupling, the residual zero-offset that tips $C_{D,\min}$ a few thousandths negative at the lowest velocity (Section 4.4.3). The existing cable-pulley rig can be extended to a dual-pulley layout without rebuilding the steel column.

Simultaneous-sampling DAQ. Replacing the PhidgetBridge 1046 with a synchronous bridge amplifier such as the NI-9237 or an HBM QuantumX module would remove the inter-channel time skew of the present multiplexed acquisition and unlock dynamic measurements: flutter studies, vortex-shedding spectra on properly sized bluff bodies, transient gust response. The modular Python pipeline of Chapter 3 is structured to accept an alternative DAQ backend through its abstract device interface, so the software cost of this upgrade is modest.

Third force component. The donated hardware includes two unused FUTEK LSB201 load cells. Mounting one of them on a vertical axis would upgrade the balance from two to three components and unlock pitching-moment measurements; the calibration matrix grows from 2×2 to 3×3 and the cross-talk model would require a parallel combined-load campaign per the first item above. A fourth cell could provide redundancy or a side-force channel.

Motorised angle-of-attack control. The SMC LEY40C-300BM linear actuator included with the donated hardware is wired and powered but not integrated into the polar acquisition loop. Replacing the manual turntable index with motorised actuation would reduce $u(\alpha)$ from the present $\pm 0.2^\circ$ to the actuator repeatability and would enable continuous, automated polar sweeps with finer angular resolution.

Temperature compensation. A thermistor mounted near the load cells, logged in parallel with the bridge voltage stream, would allow online correction of the FUTEK LSB201 zero-drift and span coefficients ($\pm 0.009\,\%\,\mathrm{RO}/^\circ\mathrm{C}$). The compensation matters most across extended polar sweeps where the test section warms by several degrees.

7.2 Methodological extensions

Spectral validation with a dedicated bluff body. The cylinder Strouhal investigation of Section 4.5.4 is masked at the lowest velocities by the rig structural mode at 4 to 5.6 Hz and by a vortex-induced-vibration lock-in at $V = 6$ m/s. A dedicated bluff body of smaller diameter, sized to place the Kármán shedding frequency well above the structural-mode band at $V \geq 10$ m/s, would isolate the wake signature on the lift channel and provide an independent dynamic-bandwidth benchmark. This experiment would require either the simultaneous-sampling DAQ listed above or, as a minimum, the present multiplexed acquisition with a longer continuous dwell at each freestream velocity.

Mount-specific θ verification. The residual angle $\theta = 2.64°$ between the balance and the tunnel frame is presently unified across the wing, cylinder and turbine rigs. A mount-specific θ campaign, with a dead-weight calibration repeated under each test geometry, would quantify the angular reproducibility of the mount-up procedure and would allow an explicit error term to be attached to coefficient-axis rotation, currently absorbed silently into the calibration matrix.

Extended HAWT sweep and on-rig geometric metrology. The rotor diameter $D = 0.540$ m used in Section 4.6 is the documented inboard 30 % of the 1:70 scaled NREL 5 MW reference geometry (Jonkman et al., 2009); an on-rig calliper measurement of the actual built diameter, together with a logged barometer reading during the campaign, would together tighten the absolute C_T axis from the present $u_A/A = 1.9\,\%$ and $u_\rho/\rho = 2\,\%$ to below 0.5 % each. Adding a third freestream velocity beyond $V \in \{8.3;\ 11.7\}$ m/s would strengthen the V-collapse argument from a two-point demonstration to a multi-point trend.

7.3 Operational practice

Periodic reference-point check. Implementing a monthly fixed-weight reading on the balance, logged to a long-running stability file, would build a drift record without requiring a full recalibration; the practice is recommended in Callahan (2016) and would force a recalibration only when the reference reading drifts beyond a predefined threshold rather than on an arbitrary calendar.

Air-supply filter chain. Inserting a coalescing filter (0.1 µm) and a desiccant dryer between the two existing AW40-F04DE regulators would bring the air-bearing supply into full compliance with the NewWay porous-media specification. The upgrade is most relevant for winter operation, when condensation in the compressed-air lines occasionally overwhelms the automatic-drain strategy of the present setup.

Data Acquisition and Processing Pipeline

This appendix points to the complete Python source tree that implements the data-acquisition, calibration and post-processing pipeline used throughout this thesis. The repository contains every script that was run to produce the figures and tables of Chapter 4, organised by phase, together with the raw measurement files in JSON form.

Online repository

The pipeline is published as a read-only folder with a public link:

vub-my.sharepoint.com/:f:/g/personal/reda_lamrani_vub_be/IgAEYUkTXgd-TbLW5YiuUtseAQs2syW-OVa7_8VP9ojTjC0

The link is reproduced verbatim in the digital version of this thesis to allow copy-paste into a browser.

Repository structure

The repository is organised as a single application directory `Code/applicatie - finaal/`, with the following top-level contents:

1. **`aerobalance/`**: the runtime package that initialises the PhidgetBridge 1046, applies the bidirectional bias-slope calibration model, runs the AIAA R-091 §3.1.1 polynomial cross-talk corrector, performs the $\theta = 2.64°$ balance-to-tunnel rotation, and handles live monitoring plus CSV logging.
2. **`config.json`**: the single calibration source of truth, holding the bias-slope coefficients per direction, the cross-talk matrix coefficients, the value of θ, and the per-velocity uncertainty terms.
3. **`data/`**: the raw JSON files for the Phase II calibration, the NACA 0012 polar campaign at four freestream velocities, the cylinder validation sweep, and the HAWT turbine campaign.
4. **`calibration/`**: the Phase II calibration scripts, including the fit-and-verify chain for the bias-slope law and the cross-talk matrix.
5. **`walkthroughs/`**: the scripts that reduce each validation campaign from raw JSON to a polar (one walkthrough per object: wing, cylinder, rotor), together with the independent recompute scripts that re-derive every figure metric from a parallel code path.
6. **`thesis_figures/`**: the figure-generation scripts that produce, one by one, the PDFs reproduced in Chapter 4. Each script is self-contained; editing the constants at the top and re-running regenerates the figure with updated values.
7. **`tests/`**: a pytest suite covering the calibration corrector, the cross-talk switch, the rotation transform and the tare procedure.

This appendix collects the key technical datasheets and specifications for the main components used in the aerodynamic balance. These documents are provided for reference and to support the traceability of the calibration and measurement results.

B.1 FUTEK LSB201 S-Beam Load Cell

The full generic datasheet for the FUTEK LSB201-25 lbf load cell (part number QSH02033) is available from the manufacturer at https://www.futek.com/product/lsb201. The key specifications relevant to this work are summarised in the load cell description of Chapter 3, Section 3.5.

In addition to the generic datasheet, the two physical units in service on the balance are each shipped with a serial-number-specific calibration sheet that lists the as-manufactured sensitivity, the non-linearity, and the temperature-compensated zero. Both sheets are reproduced below as supplied by the manufacturer. The serial-number-specific sensitivity values are the bench reference against which the in-situ Phase II calibration is compared in the discussion chapter; they confirm that the generic datasheet sensitivity cannot be substituted for the unit-specific calibration constant. CH1, in particular, differs from the generic datasheet by approximately 8 %.

FUTEK
ADVANCED SENSOR TECHNOLOGY, INC.

Calibration Data

Sensor Info

Model LSB201
Item # QSH02033
S/N 883682
Capacity ..... 25 lb

Calibration Data

Test Temp ..... 72.1 °F (22.28 °C)
Relative Humidity ..... 42.3 %

channel: 1

Excitation ..... 5.00 (Vdc)
Input Resistance ..... 352 (Ohms)
Zero Balance ..... 0.0007 (mV/V)
Output Resistance ..... 353 (Ohms)

Direction: Tension

Rated Output ..... 1.968 (mV/V)
Linearity ..... -0.105 % of R.O.

Direction: Tension

Rated Output ..... 1.968 (mV/V)
Linearity ..... -0.091 % of R.O.

Data Points

channel: 1

Load	Output	Non-Lin Error (%)	Hysteresis (%)
(lb)	(mV/V)		
	Direction: Tension		
0.000	NaN	0.000	
5.000	0.3915	-0.105	
10.000	0.7853	-0.092	
15.000	1.1793	-0.070	
20.000	1.5736	-0.033	
25.000	1.9678	0.000	
0.000	NaN	0.000	
0.000	NaN	0.000	
5.000	0.3918	-0.091	
10.000	0.7857	-0.076	
15.000	1.1797	-0.056	
20.000	1.5736	-0.041	
25.000	1.9680	0.000	
0.000	NaN	0.000	

Shunt Calibration

Shunt Value (K ohm)	Output ( )	Load (lb)
	channel: 1	
	Direction: Tension	
60.4	1.457	18.51
	channel: 1	
	Direction: Tension	
60.4	1.457	18.509

Shunt Cal is placed across (-E)(-S)

FUTEK Advanced Sensor Technology Inc. 19 Morgan, Irvine, CA. 92618 USA

FUTEK
ADVANCED SENSOR TECHNOLOGY, INC.

Calibration Data

Sensor Info

Model LSB201
S/N 999570
Item # QSH02033
Capacity ..... 25 lb

Calibration Data

Test Temp ..... 74.8 °F (23.78 °C)
Excitation ..... 5.01 (Vdc)
Relative Humidity ..... 48.6 %
Zero Balance ..... -0.0087 (mV/V)
Input Resistance ..... 352 (Ohms)
Output Resistance ..... 352 (Ohms)

Direction: Tension

Rated Output ..... 2.003 (mV/V)
Linearity ..... -0.044 % of R.O.

Data Points

channel: 1

Direction: Tension

Load (lb)	Output (mV/V)	Non-Lin Error (%)	Hysteresis (%)
0.000	0.0000	0.000	
5.000	0.4002	-0.018	
10.000	0.8006	-0.026	
15.000	1.2008	-0.044	
20.000	1.6018	-0.022	
25.000	2.0028	0.000	
0.000	0.0002		

Shunt Calibration

channel: 1

Direction: Tension

Shunt Value (K ohm)	Output ( )	Load (lb)
60.4	1.45219	18.127

Shunt Cal is placed across (-E)(-S)

B.2 Phidgets PhidgetBridge 1046

The PhidgetBridge 1046_1B specifications are available from `https://www.phidgets.com/?prodid=1027`. Channel configuration, gain settings, and noise performance used in this work are described in Section 3.1.

B.3 NewWay Air Bearings

The NewWay 50 mm air bushing specifications and application guidelines are documented in the NewWay Air Bearing Application and Design Guide (New Way Air Bearings, 2006). The key parameters (air gap, stiffness, air consumption) are discussed in Chapter 3.

B.4 SMC AW40-F04DE Filter-Regulator

The SMC AW40-F04DE filter-regulator specifications are available from the SMC product catalogue. Port sizes, pressure ranges, and filtration ratings are described in Chapter 3.

B.5 Calibration Weight Certificates

The OIML-class calibration masses used in this work are traced to the laboratory standard set. Certificates of conformity, including nominal values and expanded uncertainties, are available on request from the FLOW laboratory.

B.6 Wind-tunnel setup tutorial

This appendix collects the step-by-step procedure for the wind-tunnel installation referenced in Section 4.3.1: air-supply start-up, rail levelling, turntable centring below the tunnel-floor cutout with the plumb-line technique, cable-and-pulley rigging, and bridge zero-preload recording. The procedure is written to be reproducible by an operator who has not previously installed the rig.

This appendix documents the structural-mode characterisation of the cylinder–balance assembly that underlies the band-stop filter applied to the $C_{L,\mathrm{rms}}$ measurement in Section 4.5.3.

Method

The lift-channel signal of the cylinder V-sweep (`cylinder_vsweep_20260506_214057.json`) is processed through the full Section 4.3 calibration chain (bidirectional shared-intercept, cross-talk, balance-to-tunnel rotation $\theta = 2.64°$, L/D swap). The pre-flight segment of ~ 47 min, during which the tunnel is off and the cylinder is mechanically free of aerodynamic forcing, is analysed by Welch power spectral density (Hann window, `nperseg` $= 16 f_s$, 50 % overlap, linear detrend per segment). Per-dwell PSDs at each of the seven tunnel speeds are computed identically. A structural feature is identified as a peak that appears at the *same* frequency in both the pre-flight segment and across all per-dwell PSDs, i.e. a V-independent feature.

Result

Two structural-mode bands emerge consistently from this analysis:

- **Mode 1 at** 4.5 ± 0.3 **Hz** (rotsvast). The pre-flight PSD shows five overlapping peaks within [4.25; 4.75] Hz with peak-to-median power ratio of ~ 365 (Figure C.1). The same band returns as the dominant feature in every per-dwell PSD across $V = 4$ to $V = 16$ m/s, regardless of the predicted Karman shedding frequency $f_{St} = 0.21\,V/D$ which itself spans 3.4 to 13.4 Hz across the sweep. This V-independence falsifies an aerodynamic origin and identifies Mode 1 as a structural resonance of the cylinder–balance system.
- **Mode 2 cluster between** 13 **and** 17 **Hz** (plausible, less prominent). The pre-flight PSD shows several smaller peaks at 13.07, 13.88, 15.00, 16.00 and 16.57 Hz with peak-to-median ratios between 16 and 29. The cluster is broad rather than a single sharp resonance and is partially obscured at high V where the Karman shedding frequency enters the same band; it is reported as a secondary structural feature without claiming a single mode frequency.

Cross-reference: the bare-balance natural frequency reported by Ostafichuk and Green (2002) on a comparable air-bushing balance is 11.6 Hz. The shift to 4.5 Hz observed here is consistent with the added mass and changed mounting stiffness of the test-article-loaded configuration; an equivalent wing-loaded mode was observed at 4.2 Hz on the NACA rig, a 0.3 Hz offset from the cylinder value that scales with the relative mass difference between the two test articles.

The band-stop filter [4; 6] Hz applied to the lift signal in Section 4.5.3 removes Mode 1 only; the Mode 2 cluster sits above 13 Hz and remains in the signal, so its contribution to $C_{L,\mathrm{rms}}$ at $V \geq 14$ m/s is reported alongside the notch result rather than removed.

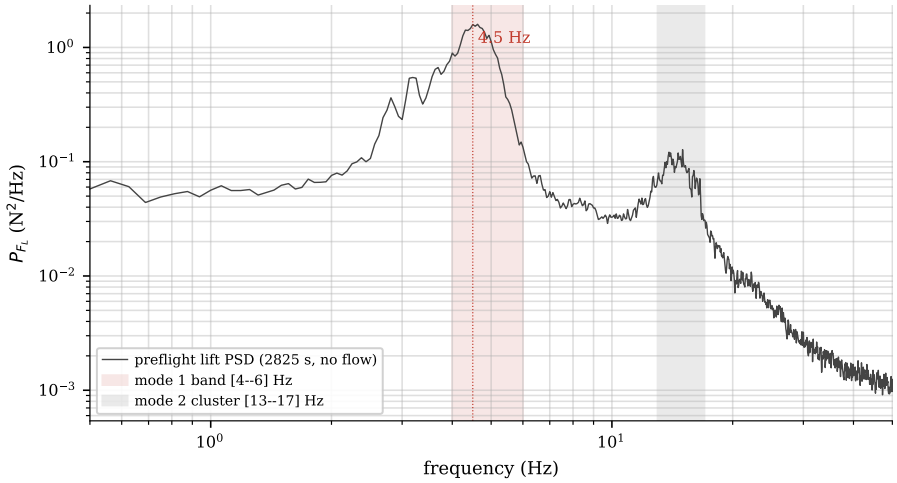

Figure C.1: Lift-channel power spectral density during the $\sim$ 47 min preflight (no aerodynamic forcing). Mode 1 band [4–6] Hz (red) is the dominant resonance at 4.5 Hz; the [13–17] Hz cluster (grey) is the secondary structural band.

Table C.1: Top peaks of the preflight lift-PSD in [3; 50] Hz, ranked by peak-to-median ratio.

Rank	f (Hz)	$P/\tilde{P}$ ratio	Band assignment
1	4.63	365	Mode 1 centre
2	4.00	204	Mode 1 sideband
3	3.19	125	Mode 1 sub-harmonic
4	15.00	29	Mode 2 cluster
5	13.88	28	Mode 2 cluster
6	16.00	19	Mode 2 cluster
7	13.07	18	Mode 2 cluster
8	16.57	16	Mode 2 cluster

Table D.1 reports per setpoint the measured thrust, the dimensionless thrust coefficient, and the $k = 2$ expanded uncertainty resolved into a random repeatability term $U_{95,\mathrm{A}}$ (per-V cycle scatter plus within-dwell velocity drift) and a systematic absolute-scale term $U_{95,\mathrm{B}}$ (the calibration floors of Section 4.3.8 combined with the atmospheric-density and rotor-area bounds). The random term sets the relative resolution between two setpoints; the systematic term sets the absolute height of the curve.

Table D.1: Per-$(V_\infty, \mathrm{TSR}_{\mathrm{full}})$ dwell statistics. F_{thrust} is the wind-axis thrust averaged over the up and down dwell of each measurement; $C_T = F_{\mathrm{thrust}}/(\frac{1}{2}\rho V_\infty^2 A_{\mathrm{rotor}})$ with $A_{\mathrm{rotor}} = 0.229\,\mathrm{m}^2$.

V_∞ (m/s)	$\mathrm{TSR}_{\mathrm{full}}$	RPM	F_{thrust} (N)	C_T	$\pm U_{95,\mathrm{A}}$	$\pm U_{95,\mathrm{B}}$
11.7	5.8	726	10.89	0.564	0.027	0.083
11.7	6.3	786	11.72	0.607	0.028	0.085
11.7	6.8	847	12.17	0.631	0.029	0.085
11.7	7.3	907	12.41	0.642	0.030	0.085
11.7	7.8	968	12.69	0.659	0.030	0.086
11.7	8.3	1028	13.30	0.691	0.032	0.087
11.7	8.8	1089	13.80	0.716	0.033	0.088
8.3	4.8	424	4.84	0.498	0.033	0.152
8.3	5.8	509	5.43	0.561	0.042	0.154
8.3	6.7	594	6.08	0.629	0.045	0.156
8.3	7.7	679	6.31	0.652	0.047	0.156
8.3	8.7	764	6.70	0.691	0.049	0.157
8.3	9.6	849	7.17	0.742	0.050	0.158
8.3	10.6	934	7.53	0.780	0.054	0.159
8.3	11.6	1019	7.70	0.799	0.054	0.159

The campaign additionally includes two reference baselines at $V_\infty \approx 11.7$ m/s: the tower alone (M01, $F = 0.84$ N, $C_T = 0.04$) and the mounted but non-rotating rotor (M02, $F = 5.04$ N, $C_T = 0.26$). Three operator-flagged runs were excluded from the analysis (two for non-constant RPM during the sweep, one tared while the rotor was already spinning).

As-built balance photographs

This appendix collects photographs of the rebuilt balance from the BikeValley donation through to its installation in the VUB tunnel, complementing the CAD render of Figure 3.2.

Figure E.1: The BikeValley donation as it arrived at VUB, before reassembly: the eight NewWay porous-graphite air bushings and clamping blocks, the original wooden turntable, the pneumatic hosing, and the steel cross-frame.

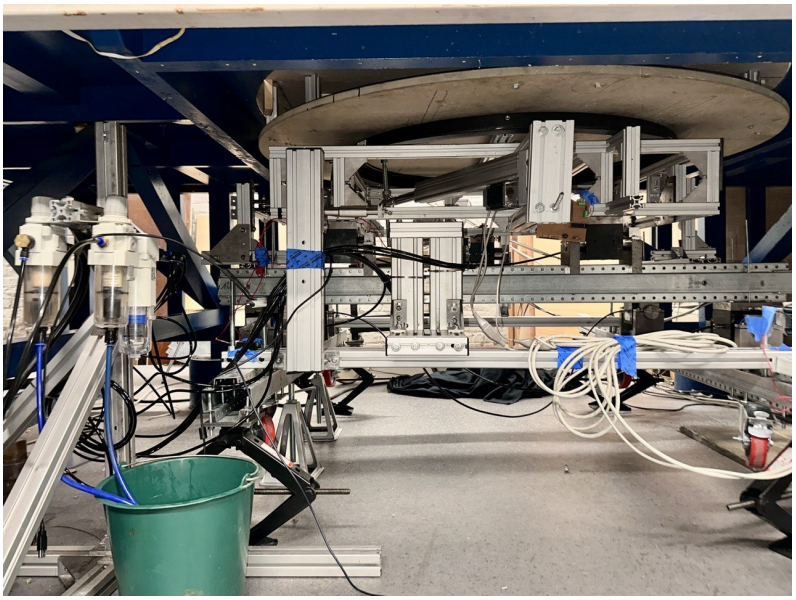

Figure E.2: Balance and turntable seen from below the test-section floor during the first installation under the VUB subsonic tunnel, with the two pneumatic regulators on the left and the signal cabling temporarily routed along the support beam.

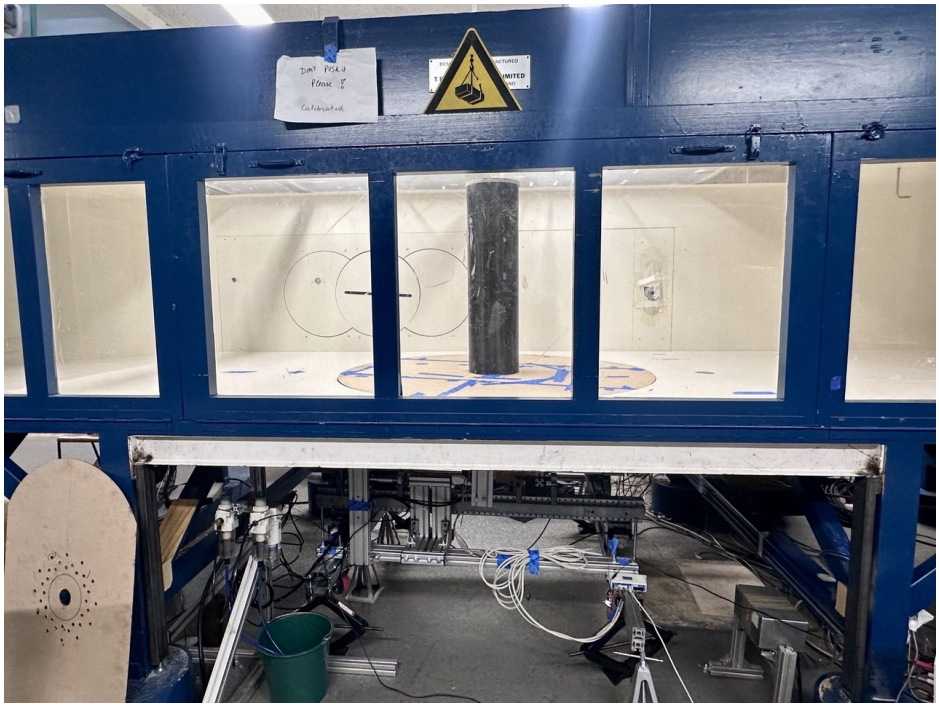

Figure E.3: Circular-cylinder validation rig installed on the balance in the tunnel test section, photographed during the cross-flow campaign of Section 4.5.

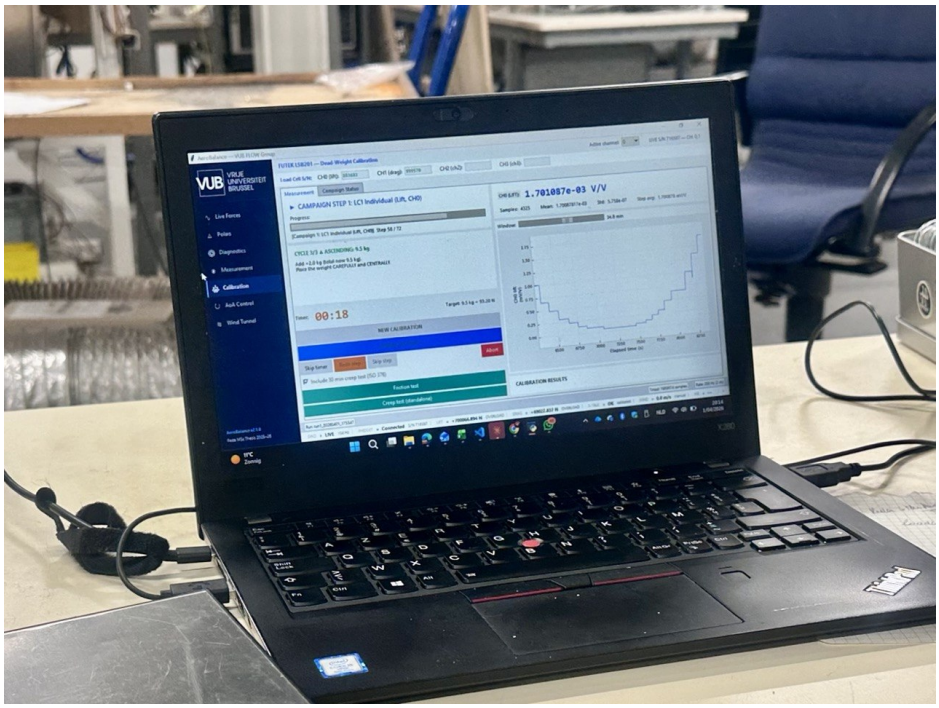

Figure E.4: Custom Python data-acquisition application of Appendix A, on the host laptop during an in-situ calibration session. The screen shows the per-step calibration wizard, the live bridge-voltage trace of the active channel, and the cycle progress indicator.

Figure E.5: Load cell clamped between the upper and lower mounting plates of one bushing stage, isolated from the rest of the column. The vertical mounting axis is the cell's sensing direction; the two plates impose the only mechanical path between the moving carriage and the fixed rig.

Production calibration configuration

All numbers below are read directly out of `config.json` in the production code base of Appendix A; the same repository holds the raw JSON measurement files under `data/` and the Python pipeline that consumes the constants. A screenshot of the calibration wizard through which an operator updates these numbers is reproduced as Figure E.4 in Appendix E.

Bias-slope law (shared-intercept fit). $F = (V_R - b)/s^{(\sigma)}$.

Channel	s_{tens} (V/V/N)	s_{comp} (V/V/N)	b (V/V)
Lift (CH0, S/N 883682)	1.84813×10^{-5}	1.84691×10^{-5}	-1.187×10^{-4}
Drag (CH1, S/N 999570)	1.86003×10^{-5}	1.75617×10^{-5}	$+9.601 \times 10^{-6}$

Polynomial cross-talk matrix. $F_{ij}^{\text{bleed}}(F_j) = a + b\,F_j + c\,F_j^2$ (AIAA R-091:2002 §3.1.1, twelve coefficients).

Direction-pair	a (N)	b (–)	c (N^{-1})
M_{01}: drag-comp → lift	-0.00636	$+2.49 \times 10^{-4}$	$+3.38 \times 10^{-6}$
M_{01}: drag-tens → lift	$+0.15120$	-2.45×10^{-3}	-1.46×10^{-6}
M_{10}: lift-comp → drag	$+0.72735$	-1.61×10^{-4}	$+3.35 \times 10^{-4}$
M_{10}: lift-tens → drag	$+1.20806$	-1.04×10^{-2}	$+3.71 \times 10^{-6}$

Pooled residual over the 180 in-situ plateaus: $u_{\text{xt}} = 0.477$ N.

Balance-to-tunnel rotation. Unified misalignment angle applied to wing, cylinder and turbine campaigns: $\theta = 2.64°$ with $u(\theta) = 0.01°$. Pooled from the dead-weight angle calibration; the per-mount diagnostic is in Section 4.3.6.

Force-domain uncertainty model. $u_c^2(F) = u_{\text{cell}}^2(F) + u_{\text{xt}}^2 + u_{\text{tare}}^2 + u_{\text{cyc}}^2(V)$, expanded to $U_{95} = 2\,u_c$.

Contribution	Lift	Drag
$u_{\text{cell}}(F) = \sqrt{a^2 + (b\,F)^2}$	$a = 0.335$ N, $b = 1.77\,\%$	$a = 0.456$ N, $b = 1.15\,\%$
u_{xt}	0.477 N (pooled)	
u_{tare}	0.30 N (Hemsch–Houlden style)	

Per-V random cycle scatter u_{cyc} (the only term growing with tunnel speed):

V (m/s)	9	12	15	18
$u_{\text{cyc,lift}}$ (N)	0.071	0.126	0.294	0.803
$u_{\text{cyc,drag}}$ (N)	0.015	0.024	0.057	0.344

The coefficient-domain budget, with the dynamic-pressure and reference-area Type-B contributions folded in through the C_L / C_D definition, is reported in Section 4.3.8 and on the polar bands of Section 4.4.

Tare. Per-α, recorded at the start of every polar session at $V = 0$ and applied as a static bridge offset before the cross-talk correction. The procedure is in Section 3.6.3; the per-session drift over the four campaign days is in Section 4.4.4.

Achenbach, E. (1968). "Distribution of local pressure and skin friction around a circular cylinder in cross-flow up to Re = 5×10^6". In: *Journal of Fluid Mechanics* 34.4, pp. 625–639. DOI: 10.1017/S0022112068002120.

Aerolab LLC (2024). *Pyramidal Force/Moment Balance V1: Product Specification*. Aerolab LLC. Jessup, MD, USA. URL: https://www.aerolab.com.

American Institute of Aeronautics and Astronautics (2002). *Calibration and Use of Internal Strain-Gage Balances with Application to Wind Tunnel Testing*. Recommended Practice AIAA R-091-2002. AIAA.

Anderson, J. D. (2017). *Fundamentals of Aerodynamics*. 6th. New York: McGraw-Hill Education.

Bardera, R., Rodríguez-Sevillano, Á. A., Barroso Barderas, E., Sor, S., and Matías García, J. C. (2024). "Calibration of a 3-Component External Balance for MAVs Wind Tunnel Research". In: *Applied Sciences* 14.23, p. 11236. DOI: 10.3390/app142311236.

Barlow, J. B., Rae, W. H., and Pope, A. (1999). *Low-Speed Wind Tunnel Testing*. 3rd ed. New York: John Wiley & Sons. ISBN: 978-0-471-55774-6.

Berger, F., Kröger, L., Onnen, D., Petrović, V., and Kühn, M. (2018). "Scaled wind turbine setup in a turbulent wind tunnel". In: *Journal of Physics: Conference Series* 1104, p. 012026. DOI: 10.1088/1742-6596/1104/1/012026.

Betz, A. (1920). *Das Maximum der theoretisch möglichen Ausnützung des Windes durch Windmotoren*. Zeitschrift für das gesamte Turbinenwesen 26, pp. 307–309.

Callahan, R. J. (2016). "Long-Term Quantitative Study of Wind-Tunnel Balance Calibrations Across Multiple Calibration Systems". MA thesis. Old Dominion University. DOI: 10.25777/09b8-cm59. URL: https://digitalcommons.odu.edu/mae_etds/3/.

Csurcsia, P. Z., Siddiqui, M. F., Runacres, M. C., and De Troyer, T. (2023). "Unsteady Aerodynamic Lift Force on a Pitching Wing: Experimental Measurement and Data Processing". In: *Vibration* 6.1, pp. 29–44. DOI: 10.3390/vibration6010003.

González, M. A., Ezquerro, J. M., Lapuerta, V., Laverón, A., and Rodríguez, J. (2011). "Components of a Wind Tunnel Balance: Design and Calibration". In: *Wind Tunnels and Experimental Fluid Dynamics Research*. InTech. DOI: 10.5772/22781.

Hemsch, M. J. and Houlden, H. P. (2014). "Repeatability Modeling for Wind-Tunnel Measurements: Results for Three Langley Facilities". In: *AIAA SciTech Forum*. URL: https://ntrs.nasa.gov/citations/20140011908.

Joint Committee for Guides in Metrology (2008). *Evaluation of Measurement Data — Guide to the Expression of Uncertainty in Measurement*. Tech. rep. JCGM 100:2008. Bureau International des Poids et Mesures. URL: https://www.bipm.org/documents/20126/2071204/JCGM_100_2008_E.pdf.

Jonkman, J., Butterfield, S., Musial, W., and Scott, G. (2009). *Definition of a 5-MW Reference Wind Turbine for Offshore System Development*. Tech. rep. NREL/TP-500-38060. Golden, CO, USA: National Renewable Energy Laboratory. DOI: 10.2172/947422.

Lin, K., Yang, X., Hu, H., and Yang, J. (2023). "Investigation on dynamic performance of wind turbines using different scaling methods in wind tunnel tests". In: *Engineering Structures* 291, p. 116434. DOI: 10.1016/j.engstruct.2023.116434.

McCroskey, W. J. (1987). *A Critical Assessment of Wind Tunnel Results for the NACA 0012 Airfoil*. Technical Memorandum NASA-TM-100019. Moffett Field, CA: NASA Ames Research Center. URL: https://ntrs.nasa.gov/citations/19880002178.

Morris, M. and Post, S. (2010). "Force Balance Design for Educational Wind Tunnels". In: *2010 ASEE Annual Conference & Exposition Proceedings*.

New Way Air Bearings (2006). *Air Bearing Application and Design Guide*. Aston, PA. URL: https://www.newwayairbearings.com.

Norberg, C. (2003). "Fluctuating lift on a circular cylinder: review and new measurements". In: *Journal of Fluids and Structures* 17.1, pp. 57–96. DOI: 10.1016/S0889-9746(02)00099-3.

Ostafichuk, P. M. and Green, S. I. (2002). "A low interaction two-axis wind tunnel force balance designed for large off-axis loads". In: *Measurement Science and Technology* 13.10, N73–N78. DOI: 10.1088/0957-0233/13/10/401.

Phidgets Inc. (2024). *PhidgetBridge 1046 — Product Specification*. Phidgets Inc. Calgary, Alberta. URL: https://www.phidgets.com/?prodid=1027.

Pinto, M. L., Franzini, G. R., and Simões, M. A. (2020). "A CFD analysis of NREL's 5MW wind turbine in full and model scales". In: *Journal of Ocean Engineering and Marine Energy* 6.3, pp. 211–220. DOI: 10.1007/s40722-020-00171-x.

Rainbird, J. M., Peiró, J., and Graham, J. M. R. (2015). "Blockage-Tolerant Wind Tunnel Measurements for a NACA 0012 at High Angles of Attack". In: *Journal of Wind Engineering and Industrial Aerodynamics* 145, pp. 209–218. DOI: 10.1016/j.jweia.2015.06.006.

Reis, M. L. C. C., Castro, R. M., and Mello, O. A. F. (2013). "Calibration uncertainty estimation of a strain-gage external balance". In: *Measurement* 46.1, pp. 24–33. DOI: 10.1016/j.measurement.2012.09.016.

Sadowski, N. B. (2018). "A Cost Effective Design for a Propeller Thrust/Torque Balance". MA thesis. Norfolk, VA: Old Dominion University. DOI: 10.25777/rkrs-3d55.

Samardžić, M., Anastasijević, Z., Marinkovski, D., Ćurčić, D., and Isaković, J. (2014). "External Six-Component Strain Gauge Balance for Low Speed Wind Tunnels". In: *Scientific Technical Review* 64.3, pp. 40–46.

Santamaría, L., Galdo Vega, M., García Díaz, M., Argüelles Díaz, K. M., and Fernández Oro, J. M. (2024). "Different Calibration Methods for a Three-Component Strain Gauge Balance to Measure Aerodynamic Forces on Airfoils". In: *Sensors and Actuators A: Physical* 374, p. 115511. DOI: 10.1016/j.sna.2024.115511.

Sheldahl, R. E. and Klimas, P. C. (1981). *Aerodynamic Characteristics of Seven Symmetrical Airfoil Sections Through 180-Degree Angle of Attack for Use in Aerodynamic Analysis of Vertical Axis Wind Turbines*. Tech. rep. SAND80-2114. Albuquerque, NM: Sandia National Laboratories. DOI: 10.2172/6548367.

Skinner, S. N. and Zare-Behtash, H. (2017). "Semi-span wind tunnel testing without conventional peniche". In: *Experiments in Fluids* 58.11, p. 163. DOI: 10.1007/s00348-017-2442-7.

SMC Corporation (2023). *LEY Series Electric Cylinder: Product Specifications and Catalog*. URL: https://www.smcworld.com/products/en/s/actuator/electric-actuator/ley/.

Sor, S., Bardera, R., and García-Magariño, A. (2019). "Development and Characterization of a Low-Cost Wind Tunnel Balance for Aerodynamic Drag Measurements". In: *European Journal of Physics* 40.4, p. 045002. DOI: 10.1088/1361-6404/ab1810.

Szepessy, S. and Bearman, P. W. (1992). "Aspect ratio and end plate effects on vortex shedding from a circular cylinder". In: *Journal of Fluid Mechanics* 234, pp. 191–217. DOI: 10.1017/S0022112092000757.

Talamalek, A., Runacres, M. C., and De Troyer, T. (2025). "Effect of Free-Stream Turbulence on the Power Performance and Wake Characteristics of Paired Counter-Rotating Vertical-Axis Wind Turbines". In: *Wind Energy* 28.1, e2968. DOI: 10.1002/we.2968.

Tank, J., Smith, L., and Spedding, G. R. (2017). "On the Possibility (or Lack Thereof) of Agreement between Experiment and Computation of Flows over Wings at Moderate Reynolds Number". In: *Interface Focus* 7.1, p. 20160076. DOI: 10.1098/rsfs.2016.0076.

Timmer, W. A. (2021). "Wind Tunnel Wall Corrections for Two-Dimensional Testing up to Large Angles of Attack". In: *Handbook of Wind Energy Aerodynamics*. Cham: Springer. DOI: 10.1007/978-3-030-05455-7_19-1.

Tomin, M., Scipioni, M., and Gatti, B. (2020). "Design, Construction and Testing of a 3-Component Force Balance for Educational Wind Tunnels in Undergraduate Aerodynamics". In: *Journal of Aviation/Aerospace Education & Research* 29.1. DOI: 10.15394/jaaer.2020.1809.

Vardanyan, A. (June 2023). "Experimental study of forced-vibration vortex shedding behind a circular cylinder". MSc thesis. Brussels: Vrije Universiteit Brussel, Brussels Faculty of Engineering (BRUFACE).

Wang, H., Zhou, Y., and Mi, J. (2012). "Effects of aspect ratio on the wake of a wall-mounted finite-length circular cylinder in subcritical and critical regimes". In: *Experiments in Fluids* 53.2, pp. 423–436. DOI: 10.1007/s00348-012-1299-z.

Weakly, J., Webb, B., Sievert, D., Kassel, T., and Hartley, N. (2024). "A Low-Cost, Adaptable System for Lift and Drag Measurement in an Educational Wind Tunnel". In: *2024 ASEE Annual Conference & Exposition Proceedings*. DOI: 10.18260/1-2--47770.

West, G. S. and Apelt, C. J. (1997). "Fluctuating lift and drag forces on finite lengths of a circular cylinder in the subcritical Reynolds number range". In: *Journal of Fluids and Structures* 11.2, pp. 135–158. DOI: 10.1006/jfls.1996.0072.

Zhou, W., Huang, D., He, Y., and Yuan, W. (2026). "Decoupling-free wind tunnel balance for high-precision measurement of three-dimensional micro-aerodynamic forces". In: *Measurement* 257, p. 118772. DOI: 10.1016/j.measurement.2025.118772.